DEVELOPMENT OF LOCALIZED DIFFUSE SOURCE BASIS FUNCTION FOR NEAR WELL UPSCALING AND COMPRESSIBLE FLOW DIAGNOSTICS APPLIED TO RESERVOIR MODELING

A Dissertation

by

CHING-HSIEN (ISSAC) LIU

Submitted to the Graduate and Professional School of
Texas A&M University
in partial fulfillment of the requirements for the degree of

DOCTOR OF PHILOSOPHY

Chair of Committee,	Michael J. King
Committee Members,	Akhil Datta-Gupta
	Eduardo Gildin
	Yalchin Efendiev
Head of Department,	Jeff Spath

December 2021

Major Subject: Petroleum Engineering

ABSTRACT

The topic of this study is the fast and accurate simulation and flow diagnostic techniques used for simulations of flow and transport in porous media, particularly petroleum reservoirs. Fast and reliable simulation and flow diagnostic techniques are becoming increasingly necessary for reservoir management and development. The geological models increase in size and level of detail and require more computational resources to be utilized. The upscaling framework is a promising approach to facilitate the simulation of detailed geological models.

The shale gas/ tight oil reservoir gradually becomes the critical exploration target for petroleum resources. This unconventional reservoir has commonly low permeability properties distribution and is explored by the multi hydraulic fractured horizontal well. The compressible flow diagnostic is a robust and flexible method to analyze the fluid flow behavior in any reservoir model. Combining the convective time of flight (resolution of flow diagnostic) and diffusive time of flight (solution of fast marching method) allows us to investigate further detail of unconventional reservoir model, particularly for the multi hydraulic fractured horizontal well.

This study's work includes developing a coupling Diffuse Source transmissibility upscaling and the novel near well upscaling method for the high-resolution geological model. The work contains the development of a new flow diagnostics that extended the previously proposed flow diagnostics to compressible flow and an application of the flow diagnostics for the field analysis of multi transverse hydraulically fractured well.

The research indicates a great potential for flexibility and scalability suitable for high-fidelity simulators and fast and robust diagnostic methods.

ACKNOWLEDGEMENTS

First and foremost, I would like to express my deepest gratitude to my advisor, Dr. Michael J. King for his academic guidance and financial support throughout my five-year Ph.D. education. His immense knowledge, insightful view, and continuous encouragement helped me overcome all the challenges in the completion of this study, which would be extremely helpful for my future career.

I am also very grateful to Dr. Akhil Datta-Gupta, the co-director of the MCERI group, for his innovative ideas. I would like to extend my sincere appreciation to my other respected committee members, Dr. Eduardo Gildin and Dr. Yalchin Efendiev who served as the substitute during my preliminary exam, for their insightful comments and valuable suggestions to improve the contents of this research.

Thanks to my colleagues from MCERI, Krishna Nunna, Chen Li, Zhenzhen Wang, Changqing Yao, Tian Liu, Sherry Liu, Andrew Malone, Lichi Deng, Imroj Syed, Ankit Bansal, Kenta Nakajima, Venkata Chavali, and the other unmentioned MCERI members, for their valuable and insightful participation in our research discussions. I would like to thank my friends and roommates at Texas A&M University for being my emotional support through all ups and downs in the US. I would also like to thank my master's advisor Dr. Bieng-Zih Hsieh and Dr. Zsay-Shing Lin, and members of Carbonate Dioxide & Reservoir Engineering Lab for helping me starts this Ph.D. journey.

Last but not the least, special thanks my parents for their unconditional love all these years during my graduate studies in the US.

CONTRIBUTORS AND FUNDING SOURCES

Contributor

This work was supervised by a dissertation committee consisting of Professors Michael J. King (advisor), Akhil Datta-Gupta, and Eduardo Gildin of the Department of Petroleum Engineering and Professor Yalchin Efendiev of the Department of Mathematics.

All the other work for the dissertation was completed independently by the student.

Funding Sources

This work was made possible by the financial support of Energi Simulation (formerly Foundation CMG) through the Texas A&M chair in Robust Reduced Complexity Modeling with Dr. Eduardo Gildin and the support of the members of the Model Calibration and Efficient Reservoir Imaging (MCERI) joint industry project at Texas A&M University. We also acknowledge the support provided by the ExxonMobil (FC)2 Alliance together with Sebastian Geiger and the International Centre for Carbonate Reservoirs at Heriot-Watt University, and to Kelkar and Associates, Inc for the use of their reservoir models, and to Schlumberger for the use of their reservoir modeling applications.

TABLE OF CONTENTS

Page

LIST OF FIGURES

Page

LIST OF TABLES

Page

CHAPTER I

INTRODUCTION

The high-resolution fine-scale geocellular representations of heterogeneous reservoirs are typically too detailed for direct flow simulation and reservoir management. While advanced computational capabilities are emerging, the task of calibrating and maintaining these high-resolution reservoir models continues to be a challenge. The need for rapid and accurate simulation techniques for fluid flow and transport in porous media is essential in particular for petroleum reservoirs due to the need to run multiple realizations to help quantify subsurface uncertainty. Therefore, it is usual to use some form of upscaling to coarsen the size of the reservoir model to obtain a model that is feasible for realistic reservoir simulation.

Diffuse source upscaling is a promising flow based transmissibility upscaling approach with the benefit of no need for global knowledge of the flow field, i.e., well locations and rates, as shown in recent literature. In contrast to traditional upscaling approaches based on the steady state flow concept, diffuse source upscaling is based on transient flow concepts. Transient flow describes the fluid flow and transport in the coarse cell volume during a simulation time step. Especially in the case of a high contrast or low permeability model, such as a carbonate reservoir or an unconventional reservoir, the steady state or pseudo steady state limits within a coarse cell volume may never be reached.

However, near well fluid flow may not be the same. he fluid flow in the near well region is mainly driven from the well (a point source or sink), the near well fluid transients should approach the steady state limit. Accurate upscaling of near well flow is indispensable for a robust upscaling workflow, as it can dominate over other aspects of upscaling in commercial reservoir simulators.

In addition to the upscaling technique, flow diagnostics is also a quick, approximate method for analyzing the flow regime and a useful tool for scanning the multiscale and/or multi-realization reservoir model. Even though these diagnostics may not be as accurate as those based on streamline simulation techniques, they have the advantages of rapid computing of swept and drained volumes without the need to know the underlying geometry of the grid. However, the current limitation of flow diagnostics arises from the basis of this methodology relying on the steady state flow assumption. The extension of the basis of flow diagnostics from steady state flow (incompressible flow) to the pseudo steady state or transient flow (compressible flow) could allow us to apply this methodology to field conventional and unconventional reservoir models. Application of the compressible flow diagnostics in the unconventional reservoir models provides a fast and robust way to analyze the progress of the flow regime. Combing convective time of flight and diffusive time of flight (DTOF) would also help analyze the dynamic growth of the pressure and convective tracer fronts during transient flow around the hydraulic fractures of a multi-stage fractured horizontal well.

1.1 Flow Equations

Fluid flow simulation of subsurface reservoir model has been widely used for the qualitative and quantitative forecast for the flow behavior and reservoir production. The numerical model is a set of equations that, according to certain assumptions, include the mass conservation equation and Darcy's flow equation to explain the physical processes active in the reservoir. The reservoir model demonstrates how fluid flowing in the porous media by describing its density, viscosity, compressibility, pressure, and velocity. Generally, the density (denoted as ρ) varies with pressure and temperature. Fluid viscosity (denoted as μ) is a measure of the resistance or tendency of the fluid to flow. Compressibility is the measure of how much the volume varies when a fluid is subject to changes in pressure. Fluids consist of one or more components that correspond to a particular chemical species in each component. A component may be present in different phases that relate to the physical state of a component. Three phases, including solid, liquid, and gaseous phases, are commonly distinguished. In a porous media, several liquid phases may be present, but only one gaseous phase can exist. In the following, we consider the equations that govern the simplest form of fluid flow in porous media in a single phase flow model.

The basic concepts of single phase fluid flow in homogeneous porous media comprise flow equations for steady state, pseudo steady state, and transient flow of fluids. Both the steady state (constant pressure at the outer boundaries) and the pseudo steady state (no flow at the outer boundaries) presume constant rate production in the well. In fact, a well is more likely to be produced at a near constant flow of bottom hole

pressure (BHP) than at a constant rate. As pressure transients hit no flow drainage region boundary, the flow regime is not a pseudo steady state; instead, it is more accurately referred to as boundary dominated flow. However, if the drainage limits are held at constant pressure, steady-state flow is reached until the pressure transient exceeds the reservoir boundary (Lee 1982).

The basic governing equation for the flow of a single phase in a porous medium is the mass conservation equation, as described below

$$\int_{\Omega} \frac{\partial(\phi\rho)}{\partial t} dV + \int_{\partial\Omega} (\rho\vec{u}) \cdot \vec{n} dS = \int_{\Omega} \rho q dV \tag{1.1}$$

where $\vec{u}$ is the fluid velocity, ρq is the sink or source term, and Ω is a control volume in which the mass is conserved. This equation states that the change in the mass of the fluid inside the control volume Ω is equivalent to the mass flowing in and out of the control volumes as well as the accumulation or decrees induced by the source or sink term ρq, respectively. Applying the theorem of divergence, we can restate the conservation of mass as:

$$\frac{\partial(\phi\rho)}{\partial t} + \nabla \cdot (\rho\vec{u}) = \rho q \tag{1.2}$$

Fluids flow in porous media is modeled by Darcy's law:

$$\vec{u} = -\frac{\vec{\vec{k}}}{\mu} \cdot (\nabla p + \rho g \nabla z) \tag{1.3}$$

Here, the Darcy velocity $\vec{u}$ is described by the permeability tensor $\vec{\vec{k}}$ of the porous medium, the pressure p, the gravitational constant g, and the spatial coordinate z in the upward vertical direction. In other words, Darcy's law dictates that the flow velocity

is proportional to the gradient of the fluid potential. Assuming the porosity is independent with time, by using the chain rule, we can rewrite the first term in Eq. (1.2) as:

$$\frac{\partial(\phi\rho)}{\partial t} = \phi \frac{\partial \rho}{\partial p} \frac{\partial p}{\partial t} \tag{1.4}$$

For the slightly compressible flow, the compressibility, c, can be defined as

$$c = \frac{1}{\rho} \frac{\partial \rho}{\partial p} \tag{1.5}$$

Combined Eq. (1.5) for the fluids and rock in the flow system and Eq. (1.4) and Substituted into Eq. (1.2) yields the mass conservation equation for slightly compressible flow:

$$\phi c_t \frac{\partial p}{\partial t} + \nabla \cdot \vec{u} = q \tag{1.6}$$

The pressure derivative term in Eq. (1.6) represents the flow regime. There are three basic flow regimes to describe the fluid flow behavior in reservoir: Steady State (SS), Pseudo Steady State (PSS), and Transient flow. First, SS flow occurs when the pressure at arbitrary location in the reservoir remains constant, i.e. the pressure is independent with the time $(\partial p/\partial t = 0)$. It requires an unaltered source and sink in the reservoir or on the outer boundary of the reservoir to maintain the pressure, which only happens when the reservoir has strong aquifer or pressure maintenance operation to completely support the reservoir. Second, PSS flow describes the pressure at different location in the reservoir is linearly decreasing with the time $(\partial p/\partial t = \text{constant})$. It occurs when there is only no flow boundary observed from the well, where the boundary can be caused not

only by the sealed geometrical structure, but also by neighboring producing wells. The last but not least, transient flow describes the pressure and flow velocity in the reservoir are changing with the time. It suggests that the pressure derivative is a function of position and time $\left(\partial p/\partial t = f\left(\vec{x},t\right)\right)$. Combined with Darcy's law (1.3) and neglected the influence of gravity, this gives an Eq.(1.7).

$$\phi c_t \frac{\partial p}{\partial t} - \nabla \cdot \left[\frac{\vec{\vec{k}}}{\mu} \cdot \nabla p \right] = q \tag{1.7}$$

To close the model requires the appropriate boundary conditions to impose for the Eq. (1.7). For example, the simplest form of boundary conditions is no flow on the external boundary, which means imposing the constraint $\vec{u} \cdot \vec{n} = 0$, where $\vec{n}$ is the normal vector pointing outwards on the boundary $\partial\Omega$. This constraint gives us an isolated reservoir system where no fluid enters or leaves. Then the system is controlled by the wells to provide the source/sink terms (q).

The integral of diffusivity equation over the pore volume of cell can be used to determine the cell pressure in the finite volume formulation.

$$c_t V_p \frac{d\bar{p}}{dt} + \sum_f q_f = 0 \tag{1.8}$$

Here V_p is the pore volume for each cell, $\bar{p}$ is the pore volume weighted pressures in each cell, and q_f is the flux across each face of the cell. Eq. (1.8) represents the flux across each face of cell is proportional to the pressure difference in adjacent cells. If the pressure derivative term is zero, Darcy's equation in terms of the pore volume weighted

average pressure is then related to the SS flow. The average pressure will be applied to the transmissibility upscaling in the second chapter.

1.2 Eikonal Equation and the Fast Marching Method

How the pressure front propagates in the reservoir provides valuable detail for the reservoir evaluation and well testing analysis. An alternative approach directly solving the propagation equation for the pressure front has been developed with the benefit of being less computationally demanding. This kind of propagation equation can be derived from asymptotic ray theory, which has been commonly used in electromagnetic and seismic wave propagation (Virieux et al. 1994). The asymptotic approach is based on an analogy between the propagating pressure front and a propagating wave, where the pressure front is defined as the location of the maximum pressure change for an impulse source.

The pressure front equation in the form of the Eikonal equation can be derived from transforming the slightly compressible diffusivity equation in heterogeneous reservoirs (Eq. (1.6)) to the Fourier domain, as shown on equation (1.9), and whose properties are well developed in the literature (Virieux et al. 1994).

$$\nabla \tau(\vec{x}) \cdot \vec{\vec{k}}(\vec{x}) \cdot \nabla \tau(\vec{x}) = \phi(\vec{x}) \mu c_t \tag{1.9}$$

Here, $\tau(\vec{x})$ is associated with the propagation of the first passage pressure front from an impulse source or sink. In the case of a homogeneous isotropic porous media, the Eikonal equation simply relates incremental τ to distance through a proportionality constant given by the hydraulic diffusivity, as shown in equation (1.10)

$$\tau = r\sqrt{\frac{\phi\mu c_t}{k}} \tag{1.10}$$

The Eikonal equation can then be solved by a family of numerical solutions called Fast Marching Methods (FMM) (Sethian 1996) for a diffusive time of flight (denoted as τ) that governs the propagation of the "pressure front" in porous media (Vasco et al. 2000, Kulkarni et al. 2001, Datta-Gupta and King 2007).

The diffusive time of flight (DTOF) can be interpreted as a spatial coordinate and further applied to reduce the 3-D diffusivity equation into an equivalent 1-D form, leading to a robust simulator for rapid performance prediction in reservoirs. Papers on this particular topic have recently been published, offering a rapid approximation of the drainage volume, pressure depletion, and well performance without explicitly performing traditional computational simulations. (Datta-Gupta et al. 2011, Zhang et al. 2013, Zhang et al. 2016, Nunna et al. 2015, Pasumarti et al. 2015, Xie et al. 2015, Yang et al. 2015, Fujita et al. 2016, King et al. 2016, Li and King 2016, Yang et al. 2016, Iino et al. 2017, Wang et al. 2017). The associated drainage volume as a function of DTOF is useful for the optimization problem related to the well spacing and multi-stage fracture spacing. The drainage volume can also be used for applications, such as fixed or slowly variable rate drawdown in bounded reservoirs, drainage volume description, production data integration, etc. This study utilizes the DTOF to represent the pressure propagation and analyze the details of the subsurface flow in the conventional or unconventional reservoir.

Based on the assumption that the pressure contours are aligned with the DTOF contours, the volume average of the diffusivity equation over a $\Delta\tau$ interval provides an equivalent 1D formulation based on the cumulative pore volume and the cumulative reservoir resistivity (Zhang et al. 2016).

$$c_t(\tau,t)\frac{dV_p(\tau)}{d\tau}\frac{\partial p(\tau,t)}{\partial t}-\frac{\partial q(\tau,t)}{\partial \tau}=0 \tag{1.11}$$

$$q(\tau,t)=\lambda_{rt}(\tau,t)\frac{dR(\tau)}{d\tau}\frac{\partial p(\tau,t)}{\partial \tau} \tag{1.12}$$

Here the cumulative pore volume $V_p(\tau)$ and the cumulative reservoir resistivity $R(\tau)$ can be computed from the initial 3D properties after solving the Eikonal equation.

$$V_p(\tau)=\int_{\tau(\vec{x})\le\tau}\phi(\vec{x})d^3x \tag{1.13}$$

$$R(\tau)=\int_{\tau(\vec{x})\le\tau}\lambda_{rt}^{-1}(\vec{x},0)c_t(\vec{x},0)\phi(\vec{x})d^3x \tag{1.14}$$

For a well with the fixed flow rate q_t in an infinite-acting domain, the early time asymptotic pressure solution in the time domain based on the DTOF can be calculated by the high-frequency limit of the diffusivity equation (King et al. 2016).

$$c_t(\tau,t)\frac{\Delta p(\tau,t)}{\partial t}=\frac{\partial q(\tau,t)}{\partial V_p(\tau)}\approx-\frac{q_t}{V(t)}e^{-\tau^2/4t} \tag{1.15}$$

Here $\Delta p(\tau,t)\equiv p_{init}-p(\tau,t)$ is the pressure drop referenced to initial pressure. The function $V(t)$ is the transient drainage volume as a function of time.

1.3 Upscaling Methods

Fluid flow in subsurface petroleum reservoirs occurs on a wide range of length scales from micrometer pore scale to macro reservoir scale (Ringrose and Bentley 2015). The scale of geologically based simulation model could categorize to three principal scales: (a) the pore-scale model, used for simulating the multiple-phase pore network, has the model size around 10 to 50 mm cube; (b) lithofacies model, used for studying, for example, the lamina sets within a tidal bedding facies, has the dimensions about 0.3 m x 0.3 m x 0.01 m; (c) the geological model, showing facies architecture, such as the patterns of tidal channel and bars, has the dimensions about 3 km x 3 km x 100 m. The geological models are commonly built to study the structure and heterogeneity of a reservoir formation on a large scale. Such high-resolution geological models represent the spatial distribution of subsurface formation and their associated characteristics. These static three-dimensional geological models are widely used to describe geological structures, such as alluvial fans, braided channels, and river deltas, by integrating the seismic, well log, and core data. Such detailed models can represent the faults, pinch-outs, as well as the depositional and diagenetic complexities of reservoirs. However, they need a prohibitive number of grid cells from a simulation point of view. Not to mention that in order to quantify the uncertainty of the geological model, it typically took tens to hundreds of these realizations. Hence, the expense of computation is costly, and the long running time of simulation makes these models unfeasible for use in reservoir management and dynamic evaluations. Therefore, the development and use of several techniques to upscale the high-resolution geological model to a computationally

manageable level is worth studying (Chawathe and Taggart 2004, Chen et al. 2003, Christie 1996, Ding 2004, Durlofsky et al. 2000, King 2007, King 1989, Liu et al. 2020, Liu et al. 2019, Warren and Price 1961).

Numerous literatures have studied many facets of the issue of upscaling. In fact, what kind of upscaling approaches are suitable depending upon the situations in the reservoir simulation workflow and the questions being asked for the simulation, such as the reservoir drive mechanism, production strategy, and the degree of detail that can be accommodated in the upscaled model. In the case of a problem involving primary depletion with only oil being produced, the coarse model should correctly capture the effects of near well heterogeneity as well as the overall large-scale flow response of the reservoir. In scenarios involving the displacement of oil by water or gas, it may be necessary to accurately capture the effects of crucial flow paths between the injection and production pairs. For the miscible flooding, the degree of reservoir mixing or dispersion induced by diffusion of particles across streamlines can be significantly affects the flow behavior as fluids propagate through the reservoir. Hence, how to evaluate the level of mixing in a reservoir and how to incorporate mixing into the upscaling procedure is crucial. These varied conditions provide a broad range of upscaling techniques (Christie 1996, Farmer 2002, Durlofsky 2003, Garmeh and Johns 2009).

The general upscaling problem is determined the coarse scale simulation from the fine scale geological grid for different purposes in simulation workflow. The fine scale cells, in practice, are amalgamated to a coarse cell by restricting the coarsening

along the principal fine grid direction (i, j, k) and avoiding collapsing the zonation. This simplified the problem to determine the equivalent coarse geometry (i.e., dimension of grid) and properties (i.e., porosity, net-to-gross ratio, and permeability) from the fine scale model. The static properties, such as porosity and net-to-gross ratio can be estimated by analytical averaging upscaling methods. The permeability (or transmissibility), on the other hand, has been studied by using the methods from simple static upscaling (i.e., analytical averaging methods) to dynamic upscaling (i.e., advanced flow based upscaling methods).

A broad classification of permeability or transmissibility upscaling methods is whether the upscaling parameters are single phase (e.g. upscaling absolute permeability, transmissibility, or well index) or two phase (e.g. upscaling relative permeability, mobility, or other diffusion or dispersion coefficients) (Deutsch and Journel 1998, Darman et al. 2002, King 1989, Pickup et al. 1994, Renard and de Marsily 1997). In the class of single phase upscaling, the upscaling methods can be categorized into analytical methods and flow based methods. As discussed in this chapter, aspects of flow based upscaling that will be reviewed include the upscaling domains applied (e.g. local, extended local, global, and local-global) and the boundary conditions imposed (e.g. pressure, no flow, and periodic). In addition, the near well upscaling has a significant impact on the accurate production and injection as well, which required further studied. There are, however, also many essential aspects of the area that have not been thoroughly investigated in this study, such as the forms of gridding method used (e.g. nonuniform, flow based, and unstructured) and the nature of displacement mechanism

(e.g. immiscible, miscible, and compositional). This study covers some important areas, specifically the flow based transmissibility and well index upscaling of single phase flow (Christie 1996, Farmer 2002, Durlofsky 2003). The primary objective of this work is to develop and evaluate new upscaling approaches that enable accurate and effective coarse scale simulations of such displacements.

1.3.1 Analytical Permeability/Transmissibility Upscaling

The fine grid properties, such as porosity, net-to-gross, and geometry, are additive and can be scaled up easily by using bulk volume or pore volume weighted averages. Nevertheless, some attention is needed for directional properties, such as permeability or transmissibility, which involve combinations of permeability and geometry.

In absolute permeability upscaling, one of the simplest methods for calculating the coarse permeability is the power averaging method (Journel et al. 1986, King 1989, Renard and de Marsily 1997). This method covers typical averaging techniques such as arithmetic, geometric, harmonic, and the different techniques obtained by varying a power averaging exponent. Sequential averaging twice with a different method, such as harmonic-arithmetic averaging and arithmetic-harmonic averaging, helps preserve directional properties. Moreover, the harmonic-arithmetic averaging provides the lower bound of the coarse permeability by calculating an arithmetic sum of multiple core floods assuming each layer are isolated; and the arithmetic-harmonic averaging provides the upper bound of the coarse permeability by calculating a single core flood by mixing of

fluid at each column of the coarse block presuming the transverse pressure equilibrium are obtained (Warren and Price 1961). The analytic half-cell steady state transmissibility upscaling (AHCSS) proposed by Cardwell and Parsons (1945) was based on these directional calculation, which provides an algebraic approximation to the steady state flow based calculation in the half pair of cells with no transverse flow (Figure 1-1).

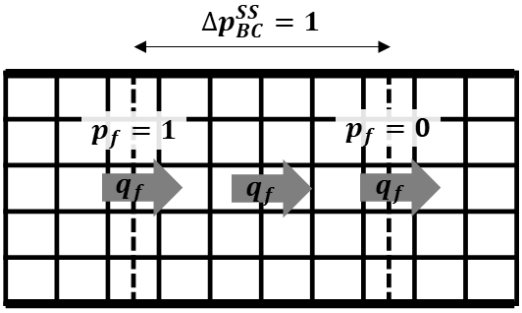

Figure 1-1 Schematic showing half-cell steady state flow for a coarse cell pair

Figure 1-1 presents the half-cell steady state flow from the center of upstream coarse cell (*p=1*) to the center of downstream coarse cell (*p=0*) with no flow on the side boundary. The AHCSS method has been implemented in the commercial software and defines as:

$$T_f = \sum_{i,j,k} \frac{1}{\sum_{m}^{N} \frac{1}{T_{f,m}}} \tag{1.16}$$

Here *m* is the index of the cell along the longitudinal direction, *N* is the total number of cells on the longitudinal direction. In this method, no transverse flow is assumed within the local model, and the intercell transmissibility is calculated by a harmonic sum along each "tube" in the direction of flow, followed by a summation over all tubes. The result is a lower bound on the effective transmissibility calculation compared to a 3D numerical flow calculation.

1.3.2 Flow Based Upscaling

More rigorous and accurate procedures for computing effective permeability and transmissibility require the solution of the fine scale pressure equation over the target coarse block (Begg et al. 1989, Chen et al. 2003, King 1989, Lunati et al. 2001). Based on the upscaling domain encompassed, the flow based upscaling methods may be further categorized into local, extended local, global, and local-global upscaling (Chen and Durlofsky 2006, Chen et al. 2003). The local or extended local upscaling techniques, have a nontrivial issue to determine the choice of boundary conditions to be imposed. Since the actual conditions (pressure or flux) imposed on the coarse grid during a flow simulation are not known a priori and usually differ, there is often some ambiguity in defining the boundary conditions in the upscaling process, as discussed in Nunna and King (2020).

1.3.2.1 Flow Based Local Upscaling

The simplest boundary conditions for local flow problem may be pressure isobars on the inlet and outlet surface with no flow boundary on the other sides of the boundary (pressure – no flow boundary) imposing on a local coarse cell problem for the steady state permeability upscaling (as shown in Figure 1-2 (a)) or a pair of local coarse cell problem for the half-cell steady state transmissibility upscaling (as shown in Figure 1-1) and steady state transmissibility upscaling (as shown in Figure 1-2 (b)).

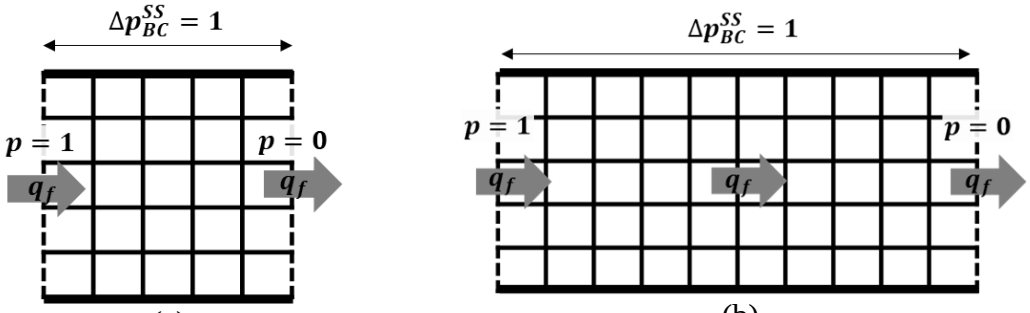

(a) (b)

Figure 1-2 Local isobar pressure and no flow boundary condition for (a) the steady state cell permeability upscaling for a single coarse cell; (b) the steady state transmissibility upscaling for a pair of coarse cell

The steady state local flow problem was set up by the pressure boundary on the upstream and downstream (denoted as dashed line) and the no flow boundary on the transverse direction (denoted as hard line). The local finite difference flow equations are solved numerically to determine the total flux (q_f) across a cell face. The effective permeability was calculated based on the Darcy's law with the reference pressure drop, as shown in Figure 1-2 (a):

$$\frac{1}{k^{eff}} = \frac{A\Delta p_{BC}^{SS}}{\mu q_f L} \tag{1.17}$$

Here the steady state pressure drop Δp_{BC}^{SS} is the difference between the upstream and downstream pressure boundary, *A* is the cross area, *L* is the length from upstream to downstream, and μ is the fluid viscosity. For the steady state transmissibility upscaling the transmissibility is determined by:

$$\frac{1}{T_f} = \frac{\Delta p_{BC}^{SS}}{\mu q_f} \tag{1.18}$$

This sort of boundary condition is an intuitive boundary condition imitating the measurements of local properties of the porous medium in the laboratory (Christie 1996, Christie and Blunt 2001). Though this type of boundary condition is most prevalent in flow based upscaling, the use of pressure isobars tends to bias the resulting transmissibility upwards, while the use of sealed side boundaries tends to bias the outcomes downwards (Cardwell and Parsons 1945). With the no flow side boundary condition, the local fluid flow paths would extend to the low permeability region, which tends to result in underestimates of the effective permeability or transmissibility.
The researcher also documented that the transmissibility upscaling representing the fine scale flow connectivity is better than the cell based permeability upscaling method (King et al. 1998, Chen et al. 2003). Hence, the following sections focus on reviewing the flow based transmissibility upscaling.

1.3.2.2 Flow Based Extended Local Upscaling

Researchers are also seeking to borrow information from the global domain to minimize reliance on local boundary conditions and proposed the extended local or local-global approaches. Extended local upscaling, including neighboring regions in the upscaling calculation domain, can better capture the effects of larger scale flow connectivity or barrier (Holden and Lia 1992, Gomez-Hernandez and Journel 1994, Hou and Wu 1997, Wu et al. 2002, Chen and Durlofsky 2006, Chen et al. 2003).

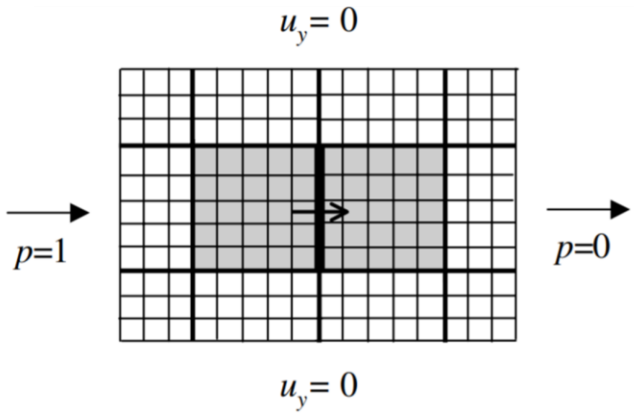

Figure 1-3 Extended local upscaling with no flow on the side boundary conditions (Chen and Durlofsky 2006)

Figure 1-3 shows the extended local upscaling with pressure and no flow on the side boundary conditions. The dark gray region is the local coarse cell pair and the flow direction is along the arrow sign. The expanding boundary area reduces the dependency on the choice of boundary condition. Preferably, there may be comparatively little change in the extended local upscaling when the two-ring area has been applied (Wen et al. 2003, Wen et al. 2000).

1.3.2.3 Flow Based Global Upscaling

Global upscaling requires more computation power comparing to the current upscaling techniques (Farmer 2002). Similar to history matching (data assimilation), this approach depends on a fine scale solution providing the pressure and flux for the local boundary conditions, such as wells, and a coarse property measured based on a fine scale solution (White and Horne 1987, Nielsen and Tveito 1998, Holden and Nielsen 2000). The coarse properties, specifically the coarse transmissibilities, are determined by the

coarse face flux and pressure difference of bulk volume weighted pressure. The benefit of global information provides an accurate coarse scale description if the global boundary conditions (prior information) have not changed by sacrificing the computation power.

1.3.2.4 Flow Based Local-Global Upscaling

In comparison to the global upscaling approach, local-global upscaling takes advantage of global boundary conditions but still addresses the global problem on a coarse scale rather than a fine scale that significantly decreases computing overhead (Farmer 2002, Chen et al. 2003). The local-global method involves coupling of fine scale local flow and coarse scale global flow and interpolating the boundary conditions to construct the coarse transmissibilities (Figure 1-4).

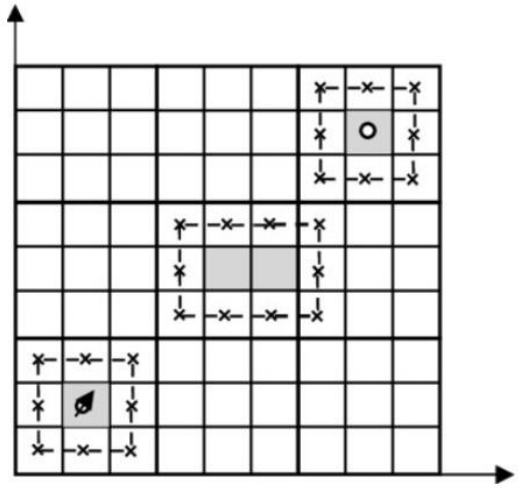

Figure 1-4 Local-global upscaling with global coarse pressures (Chen and Durlofsky 2006)

The coarse pressure solving from the global problem in coarse scale is used as boundary conditions to address the local flow problem to the coarse face of interest. This technique takes several iterations to converge to positive transmissibility. Adaptive local global upscaling was then suggested in order to speed up the process by applying the convergence criterion for iterations based on a predefined tolerance for flux and residual pressure between successive iterations and neglecting areas of very low flow to prevent negative transmissibility (Chen and Durlofsky 2006). This method certainly requires less work and has been successfully evaluated in many examples with certain variants (Efendiev and Durlofsky 2004, Wen et al. 2006, Alpak 2015, Alpak et al. 2012). However, this method requires the global well locations and well rates as a priori information, which are not typically known when upscaling a geologic model for flow simulation (Fincham et al. 2004).

1.3.3 Pseudo Steady State and Diffuse Source Upscaling

The pseudo steady state (PSS) and/or Diffuse Source (DS) upscaling, on the other hand, are completely local upscaling technique since both approaches have not relied on any outer boundary condition or the global knowledge. For example, Figure 1-5 (a) shows the SS flow required the global or extended local boundary condition to represent the transverse flow.

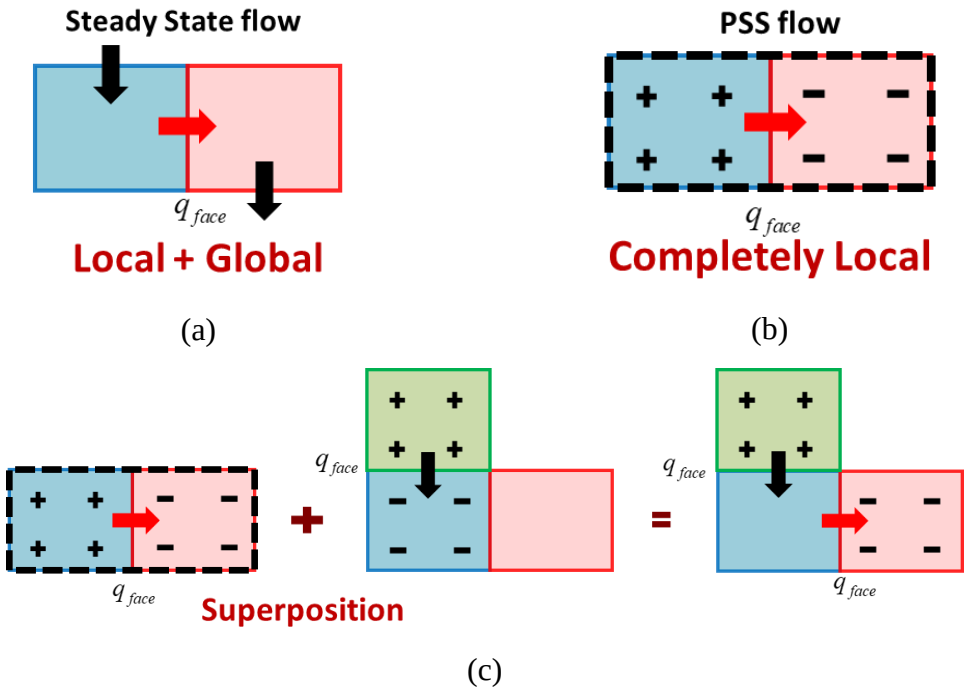

Figure 1-5 Schematic showing (a) steady state flow requiring the local and global boundary condition to represent the transverse flow; (b) completely local pseudo steady state flow as a basis function; (c) pseudo steady state flow with superposition to reconstruct the transverse flow

In contrast to the SS upscaling, PSS upscaling is a completely local method with the flux boundary condition at the interface and sealed outer boundary condition, as shown in Figure 1-5 (b). The fluid through the interface is driving by the diffuse source and sink in the local cell pair. The PSS flow allows us to use the superposition to complete arbitrary global flow field. For instance, we can recover the transverse flow in Figure 1-5 (a) by working one cell pair at a time and using superposition principal to obtain the transverse flow, as shown in Figure 1-5 (c). These approaches are based on the local PSS flow to provide a complete set of basis functions for flow description

(Nunna et al. 2015, Nunna and King 2020, Nunna et al. 2019). Figure 1-6 provides another example of the PSS upscaling in a 5x5 upscaling scheme.

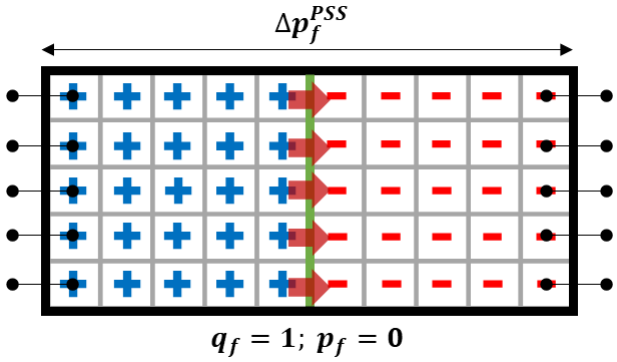

Figure 1-6 Schematic showing pseudo steady state upscaling for a pair of coarse cell with the upstream sources (plus sign) and downstream sinks (minus sign)

As discussed, pseudo steady state upscaling does not depend on the external boundary condition to provide an entirely local upscaling calculation. The shared flowing face is a pressure isobar, with no flow external boundaries. The resulting expression for the transmissibility is based on the PSS pressure drop across the coarse cells, not on the difference between the volume weighted average of the coarse cell pressures. At PSS, the source and sink strength, which distributed within a pair of adjacent cells, in the diffusivity equation is driven by the local reservoir energy. There is no well within the coarse block; instead, the source (or sink) strength sums to equal the face flux (q_f^{PSS}).

$$\frac{1}{T_f} = \frac{\Delta p_f^{PSS}}{\mu q_f^{PSS}} \tag{1.19}$$

The DS upscaling approach develops PSS solutions as the long-time limit of the local transient solution to differentiate between well-connected sub-volumes (e.g., high

permeability channel) and weakly-connected pay (e.g., extremely low permeability regions) (Nunna and King 2020, Nunna et al. 2019). The focus of this research in upscaling is therefore primary on developing completely local upscaling methods. DS transmissibility upscaling applied the asymptotic solution of the diffusivity equation derived by King et al. (2016) to a local upscaling method. It is an extension of PSS upscaling, which considers the local upscaling domain solutions under a transient state. In particular, for a local upscaling calculation, the fixed rate drawdown solution is used to determine the source/sink distribution (Figure 1-7).

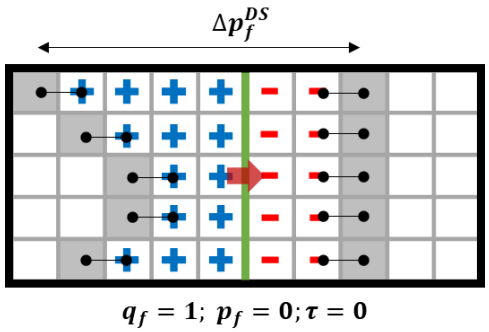

Figure 1-7 Schematic showing DS flow based transmissibility upscaling (DS) domain for a pair of the coarse cells with the effective upstream sources (plus sign) and downstream sinks (minus sign). The gray color cells are the non-pay cells

The Diffuse Source transmissibility upscaling procedure, like PSS upscaling, has no flow outer boundary and an isobar pressure condition imposing on the shared cell interface. However, instead of having the source/sink terms distributed in the entire local domain, we have the diffuse source distributed on the sub-volume that is well-connected to the interface of the coarse cell pair (cells with plus and negative signs in Figure 1-7). The source and sink strength in the diffusivity equation is driven by the local reservoir energy.

$$\nabla \cdot \vec{u} = \phi c_t \frac{\partial p}{\partial t} \approx \pm \frac{q_f}{V_p(t)} \phi \tag{1.20}$$

DS upscaling applied the asymptotic solution of the diffusivity equation to a local upscaling method (King et al. 2016, Nunna and King 2020). This method considers the local upscaling domain solutions under a transient state. In specific, the fixed rate drawdown solution is used to evaluate the source/sink distribution for a local upscaling calculation. The diffuse source formulation provides an asymptotic approximation to the solution of the diffusivity equation.

$$\nabla \cdot \vec{u} = \phi c_t \frac{\partial p}{\partial t} \approx \pm \frac{q_f}{V(t)} \phi e^{-\tau^2/4t} \tag{1.21}$$

The exponential term in Eq. (1.21) contains the diffusive time of flight, τ (Vasco and Datta-Gupta 1999), which is obtained from the solution of the Eikonal equation, subject to the boundary condition that the diffusive time of flight is equal to zero on the interface of the coarse cell pair. The Eikonal equation is solved by using Dijkstra's algorithm (Dijkstra 1959) in this study. The physical meaning of the exponential term is that it describes the early time transient pressure propagation, which moves outward from the interface of a coarse cell pair. The time dependent drainage volume term, $V(t)$, is the volume determined by the diffusive time of flight at a given time.

$$V(t) = \int_0^\infty dV_p(\tau) \cdot e^{-\tau^2/4t} \approx \sum_{Cell,\, j} PV_j e^{-\tau_j{}^2/4t} \tag{1.22}$$

In the well testing literature, the limit of detectability (LOD) described the time that one could detect the distance of pressure disturbance arriving at the boundaries (or faults) of the reservoir through the well-test derivative. Borrowing this concept of limit of

detectability from well testing literature to the diffuse source upscaling, we can identify the well-connected sub-volume in the given upscaling region by using the DTOF. The physical meaning of the well-connected sub-volume represents the system that reaches the pseudo steady-state condition.

1.3.4 Discussion

Nunna et al. (2015) first proposed using the limit of detectability (LOD) to define the pressure front propagation limit to include a more rigorous description of non-pay that would still provide low yet non-zero permeability values, making the results less sensitive to the choice of a net-pay cutoff. Following this concept, the hard threshold is applied and implemented in several literatures works based on the LOD at the PSS limit as the representative time for DS upscaling (Nunna and King 2020, Nunna et al. 2019, Nunna and King 2017). An alternative threshold of the strength of diffuse source (or sink) is used the median value of DTOF for a coarse pair of cells. Nunna et al. (2019) demonstrated the improvement of the upscaling solution using the twice mean median value of DTOF for the SPE 10 model. Syed et al. (2020) showed a similar method using the PSS limit at twice median DTOF as the threshold.

There is, however, no clear physical meaning that supports the median value of DTOF for use as a threshold. While the hard threshold is an intuitive way to cut the non-pays, all the heterogeneity of information beyond the threshold boundary has been eliminated. The further experiment may require to sophisticate the source/sink distribution and been validated for more model.

1.4 Near Well Upscaling

The upscaling methods described above are assumed that the specified pressure isobars boundary conditions have a generally linear pressure (constant pressure gradient) for driving the local flow. For example, the steady state upscaling specified the isobar pressure boundary on the upstream and downstream and no flow boundary on the side boundary, which results in a constant pressure gradient along the longitudinal direction (Figure 1-2 (a)). However, it is not the same case for the near well region. In the near well region, the outer boundary around the well cell is specified with pressure isobars boundary, which results in a radial flow, and the pressure gradient changes significantly (Durlofsky et al. 2000). The pressure gradient rises near the well and is strongly dependent upon he spatial variability of heterogeneity (Desbarats 1992).

In this section, we begin with a review of the Peaceman's well index related to the derivation and limitation of the usage. We followed by reviewing the static well index upscaling (known the well trajectory) and flow based well index upscaling (unknown the well trajectory), and discussed the issue of near well upscaling.

1.4.1 Peaceman well index

The industry standard for the well index follows Peaceman (1978), where an numerical solution has been introduced for a well with trajectory aligned with the cell centered on Cartesian grids. In reservoir simulation, Peaceman's well model is the standard method used to describe the relationship between flow rate, the bottomhole

flowing pressure, and the well cell pressure. A vertical fully completed well, for instance, can be represented as:

$$q_w = \frac{1}{\mu} WI \left(p_0 - p_{wf} \right) \tag{1.23}$$

Here, p_0 is the well cell pressure and p_{wf} is the bottomhole flowing pressure. They are related to the single-phase flow rate of the well q_w by the well index WI and fluid viscosity μ, following Peaceman (1978):

$$WI = \frac{2\pi k \Delta z}{\ln\left(r_0 / r_w\right)} \tag{1.24}$$

Here r_w is the wellbore radius, k is the geometric mean of k_x and k_y, Δz is the thickness of the grid cell and r_0 is the Peaceman equivalent well radius, which depends upon the directional cell permeability and cell dimensions. The well-known equivalent well radius (denoted as r_0) was obtained by careful numerical calculations as well as by a mathematical derivation based on an infinite non-square grid (Peaceman 1983). The use of the infinite non-square grid is equivalent to a numerical convergence study with a line source wellbore. With anisotropic permeability, the radial line source pressure contours are elliptical. To obtain a pressure solution, we rescale the spatial coordinates.

$$x \to x' = x \cdot \sqrt{k/k_x}, \quad y \to y' = y \cdot \sqrt{k/k_y} \tag{1.25}$$

$$\Delta x' = \Delta x \cdot \sqrt{k/k_x}, \quad \Delta y' = \Delta y \cdot \sqrt{k/k_y}, \quad \Delta z' = \Delta z \tag{1.26}$$

The requirement that volumes be invariant fixes the permeability $k = \sqrt{k_x k_y}$, i.e., $\Delta x' \Delta y' = \Delta x \Delta y$. In the transformed coordinates, the line source pressure contours are

circular. The bottomhole flowing pressure p_{wf} in the rescaled coordinates is referenced to a contour at r_w':

$$r_w' = \frac{1}{2} r_w \cdot \left(\sqrt{k/k_x} + \sqrt{k/k_y} \right) \tag{1.27}$$

The Peaceman radius is a circular contour in the rescaled coordinates at r_0':

$$r_0' = \frac{1}{4} e^{-\gamma} \sqrt{\Delta x'^2 + \Delta y'^2} = \frac{1}{4} e^{-\gamma} \sqrt{\Delta x^2 \cdot k/k_x + \Delta y^2 \cdot k/k_y} \tag{1.28}$$

Here, γ is the Euler-Mascheroni constant. Expressed in the original coordinates, $r_0/r_w = r_0'/r_w'$, Eq. 1.22 and Eq. 1.23 give the usual expression for the Peaceman well index.

$$r_0 = \frac{1}{2} e^{-\gamma} \frac{\sqrt{\Delta x^2 \cdot k/k_x + \Delta y^2 \cdot k/k_y}}{\sqrt{k/k_x} + \sqrt{k/k_y}} \tag{1.29}$$

Notice that the ratio r_0/r_w must be greater than one to preserve the positivity of the well index. The Peaceman diameter $2r_0'$ will always be smaller than the length of the hypothenuse of the cell, $2r_0' < \sqrt{\Delta x'^2 + \Delta y'^2} = \sqrt{\Delta x^2 \cdot k/k_x + \Delta y^2 \cdot k/k_y}$, but may be greater than either $\Delta x'$ or $\Delta y'$.

Peaceman also defined the early time validity of simulation result for Peaceman well index, as shown in Figure 1-8.

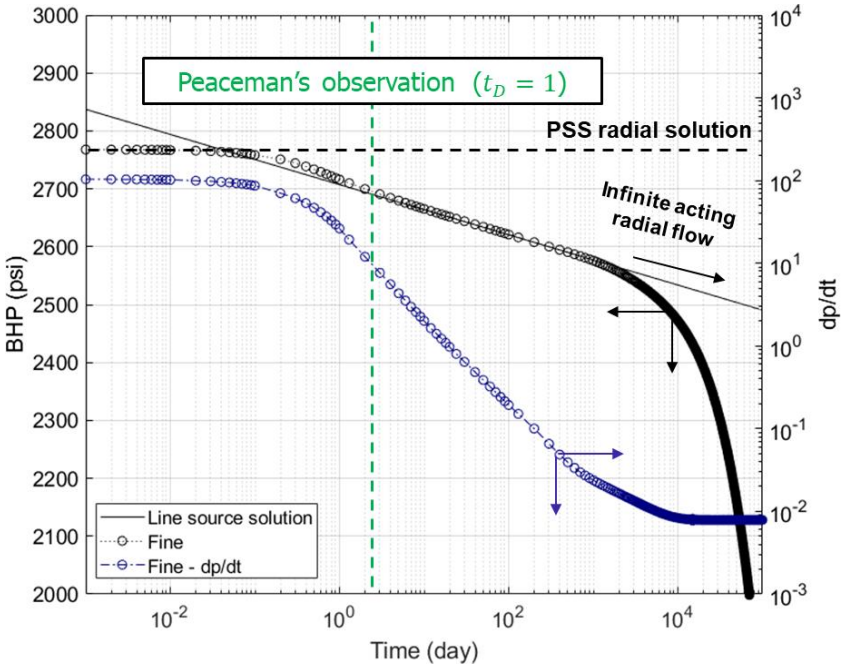

Figure 1-8 Bottom hole pressure (black circle) and pressure derivative (blue circle) profile; the black line is the line source solution; the black horizontal line represents the PSS radial solution; the green vertical line represents the early valid of simulation time at dimensionless time at one.

Figure 1-8 shows the bottom hole pressure and pressure derivative profile for a well in the center of a homogenous reservoir. The black line is the line source solution and the exact calculation which represents the infinite acting radial flow. On the other hand, the black circle is the finite difference calculation, which shows a minimum spatial resolution given by the well cell. Besides, this corresponding minimum temporal resolution given by the time that for a transient pressure to move beyond the well cell is the Peaceman's analysis. In the short time after production (time before 10^{-1} day), inside the well cell is the initial PSS radial solution (the black horizontal line in Figure 1-8). The blue circle is the pressure derivative as reference. The green vertical line represents the early valid time at $t_D = 1$.

The early time validity of simulation results based on Peaceman well index is when the dimensionless time larger than one for a single well perforation.

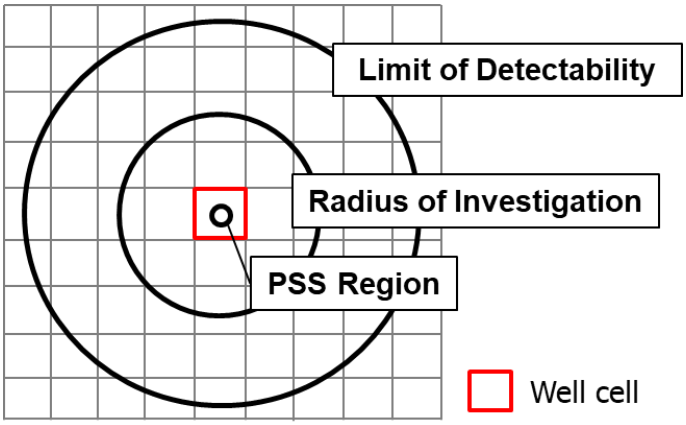

Figure 1-9 Schematics shows the PSS region is at well cell; the radius of Investigation is two cells out at $t_D = 1$; the limit of detectability is at twice of the radius of radius of investigation.

The Peaceman's observation represents the time that volumetric flow basically stabilized going into the well cell. If we think of radial flow, the radius of investigation related to PSS limit of the well cell is at two cells out, and the corresponding limit of detectability in this figure is at twice of radius of investigation. At the mean time the PSS region is still in the well cell.

1.4.2 Near well upscaling without known the well trajectory

In this section, we reviewed the near well upscaling without known the well trajectory, which is also called the static well index upscaling. In the context of a flow simulation calculation, the geologic model is usually upscaled prior to simulation. In

such a workflow, all of the reservoir properties in Eq. (1.24) and Eq. (1.29) will be upscaled properties, while the location of the injection and production well trajectories will only be defined at the coarse resolution of the flow simulator. In this case, we can only have static well index upscaling as the field development well trajectories are not simultaneously available with the detailed geologic model.

The basic geometric properties for each coarse cell are obtained by integration of the differential relationships between area, length and volume: $dV = A_x dx = A_y dy$.

Hence:

$$\Delta x = \sum_i \left(\sum_{j,k} V_{b,ijk} \Big/ \sum_{j,k} \left(\Delta y \cdot \Delta z \right)_{ijk} \right), \quad \Delta y = \sum_j \left(\sum_{i,k} V_{b,ijk} \Big/ \sum_{i,k} \left(\Delta x \cdot \Delta z \right)_{ijk} \right) \tag{1.30}$$

These sums are only taken over those columns of the fine scale model that have a non-zero volume, $\sum_k V_{b,ijk} > 0$. To simplify notation, we have suppressed the coarse cell indices (I, J, K) and express the summations in terms of the fine cell indices (i, j, k) for each coarse cell. The cell thickness and cell porosity are defined to preserve the total bulk volume and the total pore volume of the fine cells, respectively.

$$\Delta z = \sum_{i,j,k} V_{b,ijk} \Big/ \left(\Delta x \Delta y \right), \quad \phi = \sum_{i,j,k} \left(\phi \cdot V_n \right)_{ijk} \Big/ \sum_{i,j,k} V_{n,ijk} \tag{1.31}$$

The pore volume, $V_p = \phi \cdot V_n$, and the upscaled porosity, ϕ , have been expressed in terms of the net rock volume, V_n . In models that do not utilize a net-to-gross ratio, the net rock volume is identical to the bulk rock volume, $V_n = V_b$.

The literature includes two methods for the calculation of the upscaled permeability for the specific purpose of obtaining the well index. Perhaps the simplest

way to calculate the coarse cell permeability is to use a pore volume weighted average (PVWI) (Schlumberger 2017).

$$k_x = \sum_{i,j,k}\left(k_x \cdot V_p\right)_{ijk} \Big/ \sum_{i,j,k} V_{p,ijk}\,, \quad k_y = \sum_{i,j,k}\left(k_y \cdot V_p\right)_{ijk} \Big/ \sum_{i,j,k} V_{p,ijk}\,, \quad k_z = \sum_{i,j,k}\left(k_z \cdot V_p\right)_{ijk} \Big/ \sum_{i,j,k} V_{p,ijk} \quad (1.32)$$

However, there is no clear relationship between the physical flow properties on the fine and coarse grids, and as a result, this technique will be found to be among the least reliable. It will be included in the current study as it is readily available in commercial software.

A second method for permeability upscaling is based on the net rock volume weighted average of the well index relationships (King 2007, King et al. 1998). Conceptually, this volume average has placed three hypothetical line source well trajectories in each coarse cell, oriented in the I, J, and K directions.

$$\begin{aligned}
\sqrt{k_x \cdot k_y} &= \sum_{i,j,k}\left(\sqrt{k_x \cdot k_y} \cdot V_n\right)_{ijk} \Big/ \sum_{i,j,k} V_{n,ijk} \\
\sqrt{k_x \cdot k_z} &= \sum_{i,j,k}\left(\sqrt{k_x \cdot k_z} \cdot V_n\right)_{ijk} \Big/ \sum_{i,j,k} V_{n,ijk} \\
\sqrt{k_y \cdot k_z} &= \sum_{i,j,k}\left(\sqrt{k_y \cdot k_z} \cdot V_n\right)_{ijk} \Big/ \sum_{i,j,k} V_{n,ijk}
\end{aligned} \quad \Rightarrow \quad \begin{aligned}
k_x &= \left(\sqrt{k_x \cdot k_y}\right)\left(\sqrt{k_x \cdot k_z}\right) \Big/ \left(\sqrt{k_y \cdot k_z}\right) \\
k_y &= \left(\sqrt{k_x \cdot k_y}\right)\left(\sqrt{k_y \cdot k_z}\right) \Big/ \left(\sqrt{k_x \cdot k_z}\right) \\
k_z &= \left(\sqrt{k_x \cdot k_z}\right)\left(\sqrt{k_y \cdot k_z}\right) \Big/ \left(\sqrt{k_x \cdot k_y}\right)
\end{aligned} \quad (1.33)$$

The use of the net rock volume as the weight is consistent with the definition of the well index for vertical and inclined wells (Schlumberger 2017). The equivalent coarse cell directional permeability is determined from the geometric mean of the permeability on the coarse grid. This algebraic well index (AWI) upscaling approach is as simple to implement as the pore volume weighted calculation, but gives consistently better estimates of well performance. It will also be included as a reference in the current study.

Although static well index upscaling is a computationally efficient method, the flow based well index upscaling techniques are considered more accurate in preserving the impact of heterogeneity in the near well region. Many studies have shown that numerical flow based upscaling approaches can accommodate complex near well heterogeneity, and provide representative properties (i.e., link permeability or well index) for a coarse well block through properly integrating the numerical solution of the fine-grid pressure equation in the near well area (Liu et al. 2019, Durlofsky et al. 2000, Karimi-Fard and Durlofsky 2012, Ding 1995, Li and Durlofsky 2016, Zhou and King 2011, Ding 2010, Li et al. 2014). We will review this literature as a prelude to investigating whether a PSS upscaling approach can be utilized to improve the calculation.

1.4.3 Near well upscaling with well trajectory

The literature for flow based well index upscaling shares two elements: the numerical calculation of the well index but also the modification of the intercell transmissibility in the near well region, as shown in Figure 1-10 (Ding 2004, Durlofsky et al. 2000, Karimi-Fard and Durlofsky 2012, Fu et al. 2011, Ding 1995, Muggeridge et al. 2002, Mascarenhas and Durlofsky 2000, Nakashima et al. 2012, Soeriawinata et al. 1997). Following Eq. (1.23) we have an expression for the upscaled well index, and similarly for the upscaled intercell transmissibility based on the total flux across a coarse cell face in the Steady State flow (SS) , and similarly for the upscaled intercell transmissibility based on the total flux across a coarse cell face.

$$\frac{1}{WI} = \frac{\left(\bar{p}_0^{SS} - p_{wf}\right)}{\mu q} \tag{1.34}$$

$$\frac{1}{T_f} = \frac{\Delta \bar{p}^{SS}}{\mu q_f^{SS}} \tag{1.35}$$

Where the literature references differ is in the choice of the flow calculation itself, and to some extent on the method of the pressure average. It should be recognized that both of these expressions are fundamentally correlations and may result in non-physical negative values. For the well index, this may be the case for a weak well in the immediate vicinity of strong wells (Peaceman 1990). For the intercell transmissibility, negative values may arise from the impact of local heterogeneity and misalignment of local flow with the global pressure field (Chen et al. 2003, Chen and Durlofsky 2006, Wen et al. 2006).

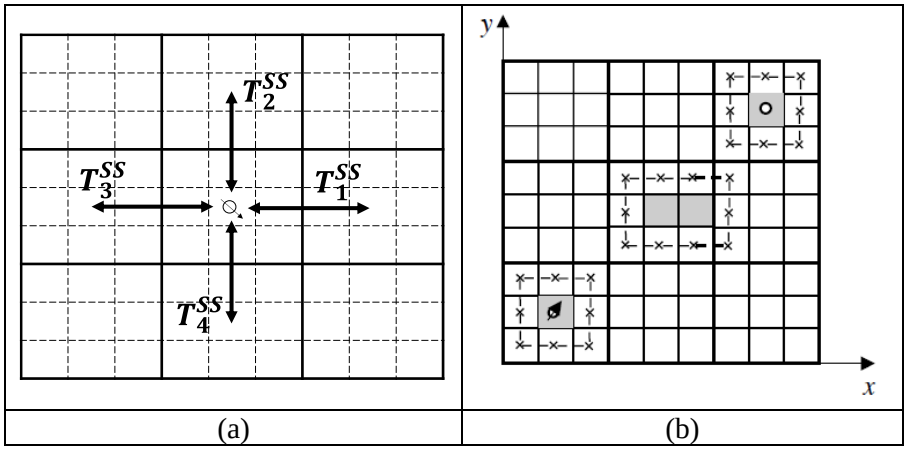

Figure 1-10 Schematic showing (a) Equivalent well cell intercell transmissibility on a coarse grid (from Ding (1995)); (b) Coarse domain with well driven global flow and local boundary conditions for near-well upscaling and transmissibility upscaling. The ×'s represent coarse pressures (from Chen and Durlofsky (2006)).

Ding (1995) uses steady state incompressible flow with wells uniformly distributed to simulate the reservoir region in the vicinity of the well on the fine grid. The use of a potentially large fine scale region may be computationally expensive, while the choice of additional wells may introduce arbitrariness into the flow pattern. The steady state pressure averages for each cell are defined by a reservoir storage (pore volume) weighted average to obtain the upscaled well index and the four intercell transmissibilities (Figure 1-10 (a)).

Durlofsky et al. (2000) used a similar approach as Ding (1995), but specifies a generic steady state boundary condition in a more localized region and utilizes a bulk rock volume weighted average for the pressure. The boundary conditions are specified as pressure isobars along with the x and y faces of the outer boundary of the local region with no flow in the z direction. The well is specified as a fixed bottomhole flowing pressure on the perforated well cell. This was generalized through the adaptive local-global upscaling of Chen and Durlofsky (2006) (Figure 1-10 (b)) in which global pressures are computed on the coarse scale and are then interpolated to provide local fine scale pressure boundary conditions for either the well index or the intercell transmissibility. As discussed in Nunna et al. (2019) and Fincham et al. (2004), the choice of specific global wells may introduce arbitrariness into the flow pattern. This approach is probably best thought of as a precursor to multi-scale simulation, in which the global flow pattern is obtained during the flow simulation itself (Hou and Efendiev 2009).

Muggeridge et al. (2002) extended the approaches of Ding (1995) and Durlofsky et al. (2000) and compared the upscaling results on a variety of 2D and 3D problems, including cases with horizontal and deviated wells. In the extension to Ding's work, single-phase flow simulation with a producer is run on the full fine grid for a few time steps until PSS flow has been reached, rather than simulating a more arbitrary SS flow solution. In the modification of Durlofsky's approach, the buffer zone was extended in all directions, including above and below, but does not extend beyond the boundaries of the reservoir. Their reduced computational domain is larger than that employed by Durlofsky et al. (2000), who considered each perforated coarse grid layer individually with a region only one coarse grid layer thick. According to their findings, both the well index and modified intercell transmissibility with the direction perpendicular to the well trajectory are required for satisfactory results, while a modified intercell transmissibility aligned with the direction of the well trajectory appears to be unnecessary.

Ding (2004) extended the near well upscaling work of Ding (1995) to complex wells on both cartesian and corner point grids. Again, steady state incompressible fine scale flow is simulated in the selected near well region. The accuracy of the absolute permeability upscaling around a complex well depends on the choice of the global boundary utilized on the fine grid simulation. The question of the size of the near well zone for fine scale simulation remains unresolved.

1.4.4 Discussion

In this section, we first discussed the time of validity of Peaceman well index and followed by the current near well upscaling. As discussed in Peaceman (1978, 1983), there is a minimum time of validity for the SS flow contact can be applied for the usage of Peaceman well index in the fine scale model. However, the time of validity for the well index upscaling and coarse model has not been addressed. How to extend the time of validity to a well index upscaling calculation is crucial for the usage of simulation results in coarse model.

Much of the near well and well index upscaling literature is based on the principle of steady state flow, where the local flow solution must be dependent upon the global boundary conditions (Ding 1995, Renard and de Marsily 1997, Durlofsky et al. 2000, Ding 2004, Muggeridge et al. 2002, Chen and Durlofsky 2006). However, as Ding (2004) discussed, the near well upscaling results are only weakly linked to the external boundary conditions, as well-driven flow dominates in the vicinity of the well. As discussed in Nunna et al. (2019), the use of pseudo steady state (PSS) and transient flow as a means of decoupling the local upscaling problem from the global boundary conditions. The current study applies the same upscaling strategies to the near well region to obtain local transport properties independent from the global boundary conditions, consistent with the insight of Ding (2004).

1.5 Waterflood Flow Diagnostics

The streamline-based waterflood flow diagnostics have been used for reservoir flow description and diagnostics through variety of field scale applications (Olalotiti-Lawal et al. 2017, Datta-Gupta and King 2007, Yin et al. 2010, Kam and Datta-Gupta 2016). The application of streamline-based waterflood flow diagnostics includes in rapid screening and ranking 3D reservoir models (Ates et al. 2005, Idrobo et al. 2000) and in fast flow simulation accounting for the realistic flow physics including gravity, compressibility and multiphase and multicomponent flow (Tanaka et al. 2013, Tanaka et al. 2015, Blunt et al. 1996, Bratvedt et al. 1996, Jessen and Orr 2002, Cheng et al. 2006).

In the flow analysis, the Lorenz plot is commonly used to measure the heterogeneity of reservoirs, which is based on ranking the fraction of thickness weighted permeability of one layer over the sum of all layers (Schmalz and Rahme 1950, Lake and Jensen 1989, Shook and Mitchell 2009). The earlier version of the Lorenz plot is derived from core or log data, which can be called the static Lorenz plot. Later, Shahvali et al. (2012) adapted the Lorenz plot to their cell-based time-of-flight calculations. They redefined the Lorenz plot by ranking the fraction of flow capacity for an injector/producer well pair. The new Lorenz plot can be called the dynamic Lorenz plot because the flow capacity represents the total time-of-flight summing up from time-of-flight tracing forward from the injector and backward from the producer at any given time.

Although the streamline-based flow diagnostic has been successful applied in the unstructured grid (Prevost et al. 2002, Pomata et al. 2007, Sun et al. 2005), explicit

tracing of the tracer front in the unstructured grid is still challenging. In contrast to explicitly tracing the streamlines in the flux field, the finite difference waterflood flow diagnostic computed directly on the physical based grid by solving advection equations without the numerical iterations (Shahvali et al. 2012, Møyner et al. 2015a, Borregales et al. 2020, Olalotiti-Lawal et al. 2020). The finite difference waterflood flow diagnostic have been applied to manage production strategy and rank the geostatistical models (Møyner et al. 2015a), to interactive visualization and fast simulation approximations to also account for polymer mobility effects (Krogstad et al. 2016, Krogstad et al. 2017), to implement for geomodel ensembles (Watson et al. 2020), to extend to account for geomechanical effects without increasing the computational overhead significantly (Sosa et al. 2020), to implement for mimicking the streamline-derived analytical sensitivity computation used in the generalized travel-time inversion technique (Olalotiti-Lawal et al. 2020), to employ as a proxy model to accelerate the optimization process for designing the well placement and trajectory (Krogstad and Nilsen 2020), and to substitute streamline simulation-based finite difference for optimizing waterflooding (Spooner et al. 2019, Boumi Mfoubat and Zaky 2020).

1.5.1 Discussion

The finite difference waterflood flow diagnostic is based on incompressible fluid flow, limiting usage in water flooding scenarios, requiring an injector and producer well pair. This method provides a simpler analysis of single phase (or multiphase) steady flow scenarios that can be done in a far shorter period than a complete dynamic

simulation. However, the usage of current waterflood flow diagnostics is limited in the steady state flow regime, which may not be available for the reservoir, such as primary depletion reservoir and unconventional reservoir. Hence, the effort of extending the waterflood flow diagnostics to the compressible flow diagnostics is required and motivated for this study.

In the water flooding scenarios, the lower total time-of-flight region represents the path of strong interwell interaction, and the higher tracing time signifies the area difficultly reaching from the current water flooding scenarios, also called the stagnation zone. However, in the unconventional reservoir, due to the lack of the injectors as a source, the total time-of-flight is missing, and the time-of-flight tracing from the producers tends to reach infinite value at the boundary of the drainage region. Therefore, the development of a modified dynamic Lorenz plot for the unconventional reservoir is required.

1.6 Geologic Models

This study considered three geological models for upscaling purpose. The first model is the full SPE10 Comparative Solution (Christie and Blunt 2001). The second model is the Amellago Carbonate outcrop model provided by the Carbonate Reservoir Group at Heriot-Watt University for research purposes (Geiger 2016). The third model is the former Soviet Union shale reservoir model (FSU).

1.6.1 SPE 10 Model

The SPE10 model is a North Sea sector model designed to test upscaling approaches (Figure 1-11). The top 35 layers consist of the Tarbert formation and represent a prograding near shore environment. The permeability architecture consists of low contrast high permeability stratified sheet-like sand structures in a low permeability background. The bottom 50 layers are part of the Upper Ness sequence representing a fluvial environment. The reservoir consists of high permeability channels embedded in a background of low permeability, providing abrupt local contrast in the permeability.

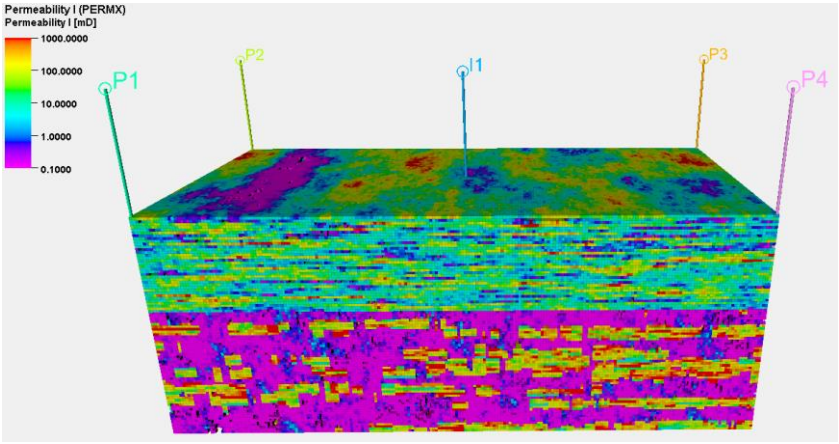

Figure 1-11 SPE10 3D permeability (md) with the five-spot pattern well placement

Our SPE10 reference calculation consists of a standard five-spot pattern with one injector located at the center of the grid blocks at (i, j) coordinates of (30, 110), and four producers at the outside corners of the four corner grid blocks. Finite difference flow simulation is performed and rapidly approaches steady state by fixing the producers and the injector with a bottomhole pressure constraint at 1000 psi and 4000 psi, respectively.

The reservoir is modelled as a single-phase oil system. The total compressibility was 8.9×10-6/psi and the oil viscosity was 1 cp at the initial reservoir pressure. FIELD units are used for this model consistent with the SPE10 literature. As the bottomhole flowing well pressures are defined, the accuracy of the near well upscaling techniques is assessed from the total well liquid flow rates in comparison between the fine and coarse models.

1.6.2 Amellago Carbonate Outcrop Model

Amellago, a Jurassic age carbonate ramp outcrop in the High Atlas Mountains of Morocco, has been extensively researched from a geologic perspective and has been provided to us as a 3D geologic model for research purposes (Shekhar et al. 2014). It will be used to demonstrate the flow upscaling approaches in this study. The reservoir model consists of 8 stratigraphic units with 5 major faults that segment the reservoir into 3 fault blocks, although there is no expectation that these faults are sealed (Figure 1-12).

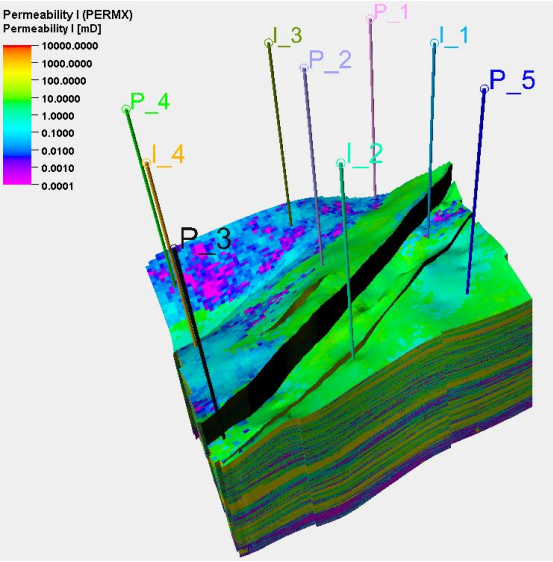

Figure 1-12 Amellago permeability (md) with the inverted five-spot pattern well placement

To focus the current study on the property upscaling, we will represent flow in the model in an un-faulted, pseudo-depositional space. The internal architecture of the reservoir is based on 8 depositional environments, each of which may extend across multiple strata. The depositional environments control the spatial distribution of 14 major facies associations. The facies association is the primary control on porosity, although the porosity is further modified by diagenetic effects. The depositional environments, the facies associations, and the porosity are distributed spatially using geostatistical approaches. Different porosity-permeability correlations and vertical to horizontal permeability ratios, are specified for each facies, and are used to determine the permeability distribution.

Table 1-1 Elements of the Amellago model and data for the simulation

Geologic elements	8 stratigraphic units 5 faults (3 fault blocks) 8 depositional environments: geostatistical distributions 14 facies associations: geostatistical distributions conditioned by the depositional environment
Reservoir geometry	Number of cells: 79×80×1099 cells of which 6,480,803 are active (93.31%) Average grid block size: 15.19 m × 15.49 m × 21 cm
Porosity	Geostatistical distributions conditioned by the facies, with additional diagenetic effects
Permeability	Horizontal permeability: $k_H(\phi)$ transform is uniform per facies, $k_x = k_y = k_H$ Vertical permeability: k_V/k_H ratio values are specified for each facies
Reservoir conditions	Initial pressure: 2.07×10^7 *Pa*
Fluid properties	Initial oil viscosity: 0.001 $Pa\cdot\sec$ Initial total compressibility: 1.1×10^{-9} Pa^{-1}
Well conditions	4 Injector wells with BHP pressure constraint at 2.4×10^7 *Pa* 5 Production wells with BHP pressure constraint at 1.6×10^7 *Pa*

For flow simulation, the outcrop model is developed with a nine well inverted five-spot pattern well placement (Figure 1-12). Following Liu et al. (2019), we utilize single phase oil finite difference reservoir simulation, which rapidly approaches steady state. We extend the earlier study of transmissibility upscaling to include near well upscaling. The elements involved in the development of the model and simulation data are summarized in Table 1-1. We utilize SI units for consistency with the Amellago literature.

1.6.3 Former Soviet Union Shale Reservoir Model

The former Soviet Union shale reservoir model (FSU) is a shale reservoir model in the Russian region. The reservoir model consists of 3 zones with sand and shale facies. There are no sealed faults or isolation segments in the model. The facies association is the primary control on porosity and distributed spatially using geostatistical approaches; especially for the shale facies, there is no pore volume in the associated cells. For flow simulation, the simulation model is developed with a nine well inverted five-spot pattern well placement (Figure 1-13).

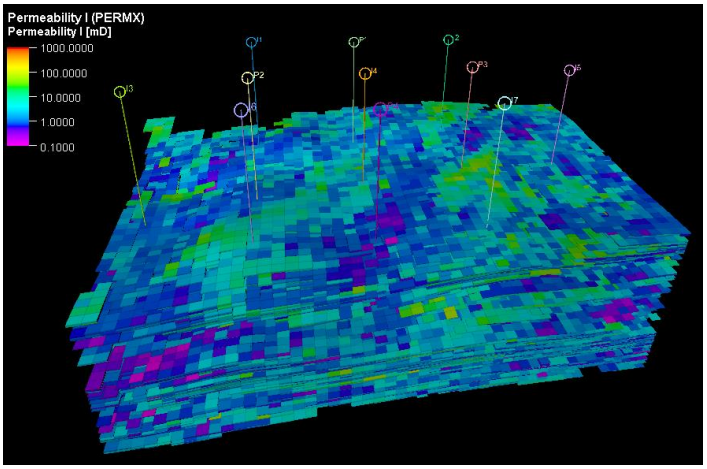

Figure 1-13 FSU permeability (md) with the inverted five-spot pattern well placement

Table 1-2 Elements of the FSU model and data for the simulation

Geologic elements	2 facies: shale and sand facies 3 zones: a10, a11, and a12
Reservoir geometry	Number of cells: 50×35×575 cells of which 130,706 are active (12.99%) Average grid block size: 100 m × 100 m × 64.5 cm
Porosity	Geostatistical distributions conditioned by the facies
Permeability	Single model distribution; range from 0.1 md to 113 md with the mean value 4.366 md and standard deviation 7.648 md
Reservoir conditions	Initial pressure: 200 bar
Fluid phases	Consider oil, water, and gas phases in the simulation
Fluid properties	Initial oil viscosity: $5.772\times10^{-1}\ Pa\cdot\sec$ Initial gas viscosity: $1.9762\times10^{-2}\ Pa\cdot\sec$ Initial water viscosity: $4.008\times10^{-1}\ Pa\cdot\sec$ Initial total compressibility: $5.9\times10^{-5}\ Pa^{-1}$
Well conditions	7 Injector wells with BHP pressure constraint at 600 bar 4 Producer wells with BHP pressure constraint at 25 bar
Simulation time	15 years

The elements involved in the development of the model and simulation data are summarized in Table 1-2. Although it's more realistic to schedule the target well rates for field modeling, for testing purposes, both injectors and producers are fixed pressure

constrained. This allows us to utilize the upscaled well rates to test the upscaling calculation.

1.7 Research Objectives

The goal of this research has three folds. First, we will examine the current DS upscaling by using the Amellago carbonate outcrop model and improve the current state of the art in DS upscaling methods. Second, we will extend the usage of the time of validity in the well index upscaling calculation, and develop the near well upscaling by analyzing the near well flow behavior to adjust the coarse well block half-cell transmissibility. Third, we will develop the compressible flow diagnostics that extended the previously proposed flow diagnostics to compressible flow and new Lorenz plot that extended from the dynamic Lorenz plot to the primary depletion and unconventional reservoir. In the end, we apply the flow diagnostics for the field analysis of multi transverse hydraulically fractured well. The research indicates a great potential for flexibility and scalability suitable for high-fidelity simulators and fast and robust diagnostic methods.

We proposed a novel coupling DS transmissibility upscaling and near well upscaling strategies for high contrast geological models, which can generate a minimum number of active cells consistent with fine scale reservoir continuity and barriers. The results are validated with SPE 10, Amellago carbonate outcrop reservoir, and FSU shale gas model. This technique is also applicable to other conventional and unconventional reservoirs

As for the flow diagnostic, we propose a compressible flow diagnostic formulation to determine the convective time of flight for the unconventional reservoir management. We also applied the depletion Lorenz plot and Lorenz coefficient, which measure the heterogeneity of the dynamic flow, to quantitatively analyze the loss of heterogeneity for the coarse reservoir model. The compressible flow diagnostic relieves the restriction of the assumption of the steady state dynamic flow model for the existing flow diagnostic state, which allows us to manage the primary depletion model. The application of this methodology to analyze the multi-stage fractured horizontal well in the unconventional reservoir model is our further work plan. The compressible flow diagnostics in an unconventional reservoir model could provide a fast and robust way to analyze the progress of the flow regime. Furthermore, simultaneously analyzing the convective time of flight and the diffusive time of flight would be useful to measure the dynamic growth of the pressure and convective tracer fronts during transient flow around the hydraulic fractures of a multi-stage fractured horizontal well.

CHAPTER II

IMPROVED DIFFUSE SOURCE UPSCALING*

In this chapter, we begin with review the current DS upscaling from Nunna et al. (2019) and examined the method on the Amellago model. We then reanalyzed the diffuse source distribution based on threshold and exponential method to search a better distribution method to improve the upscaling results.

2.1 Examine Current Diffuse Source Upscaling

In the well testing literature, the limit of detectability (LOD) described the time that one can detect the distance of pressure disturbance arriving at the fault or the boundary of the reservoir through the well-test derivative. As shown in the Chapter 1.3.3, the well-connected sub-volume in the given upscaling region can be identified by using DTOF (Figure 1-7). The previous studied from Nunna et al. (2019) introducing the twice mean median DTOF method as a threshold to identify the well-connected sub-volume, which provides an effective solution for the SPE 10 model but may lack the rationally physical meaning with it.

* Part of this section is reproduced with the permission from Liu, C.H., Nunna, K., Syed, I. et al. 2019. Evaluation of Upscaling Approaches for the Amellago Carbonate Outcrop Model. Paper presented at the SPE Europec featured at 81st EAGE Conference and Exhibition, London, England, UK. 51. Society of Petroleum Engineers. DOI: 10.2118/195560-MS.

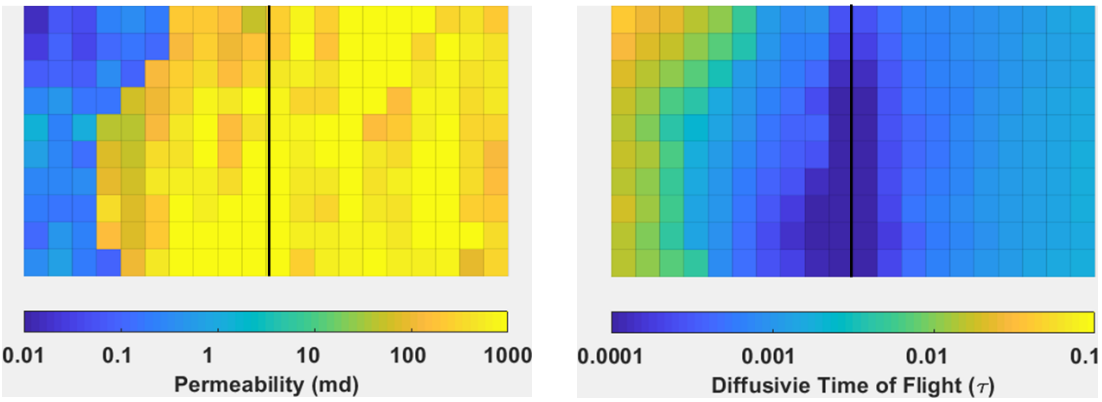

(a) (b)

Figure 2-1 (a) Permeability distribution (md); (b) DTOF distribution in a pair of 10x10 coarse cells (After Nunna et al. (2019))

Followed the discussion from Nunna et al. (2019), We use a pair of 10x10 coarsened cells to analyze the source/sink distribution. Figure 2-1 (a) shows the permeability distribution for this pair of cells from SPE 10 layer 55, which is the layer with banded channel pattern. The black line shown in the middle of the figure represents the interface between the coarse cells. We can see that the right cell has a relatively large and homogeneous permeability distribution. On the other hand, the left cell has part of large permeability connecting with the interface and suddenly drops to low permeability toward the outer boundary. We were now tracing the diffusive time of flight from the interface between the pair of cells to the outer boundary for each cell using the Dykstra method. The resulting diffusive time of flight will then use in the calculation of diffusive source distribution (Figure 2-1 (b)). The DTOF tracing from the interface represents the pressure propagation from the interface to the upstream and downstream of the cell pair. In DTOF map, the blue color represented the region which is easily accessible, and the yellow color represented the region which is harder to reach.

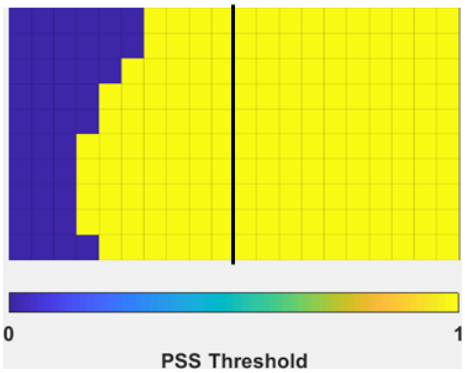

Figure 2-2 The well-connected cells (yellow color) and discarded cells (blue color) based on the mean median threshold method

As reported from Nunna et al. (2019), Figure 2-2 represents that the mean median threshold method provides a good measure to capture the permeability pattern shown in the Figure 2-1 (a). For the SS flow based upscaling (referenced Figure 1-2), the local steady state flow will across all the low permeability cell in the left coarse cell, which will underestimate the intercell transmissibility.

We then tested the mean median threshold method on the SPE 10 model again and compared with the fine scale results and AHCSS method (method from commercial software as discussed in Chapter 1.3).

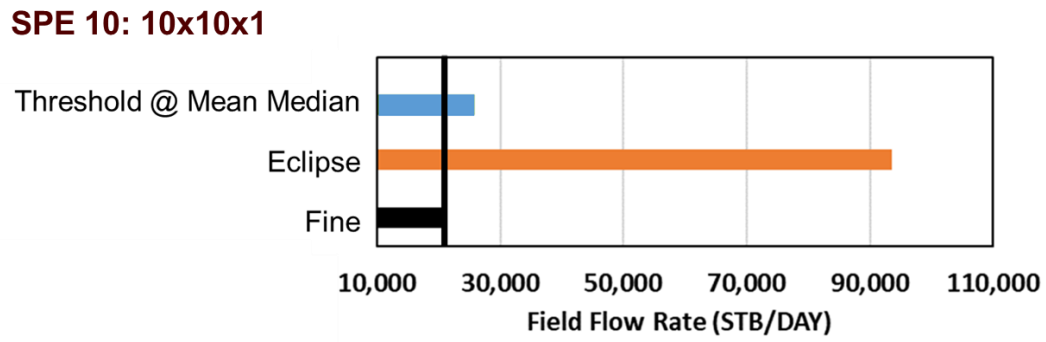

Figure 2-3 Comparison of field flow rate for SPE 10 model

The reservoir parameters and simulation schedule for the SPE10 model has reported in Chapter 1.6. The simulation result is showing the Figure 2-3 by comparing the field flow rate with the coarsen ratio 10x10. The mean median threshold method provides a excellent result compared to the AHCSS method, as reported from Nunna et al. (2019).

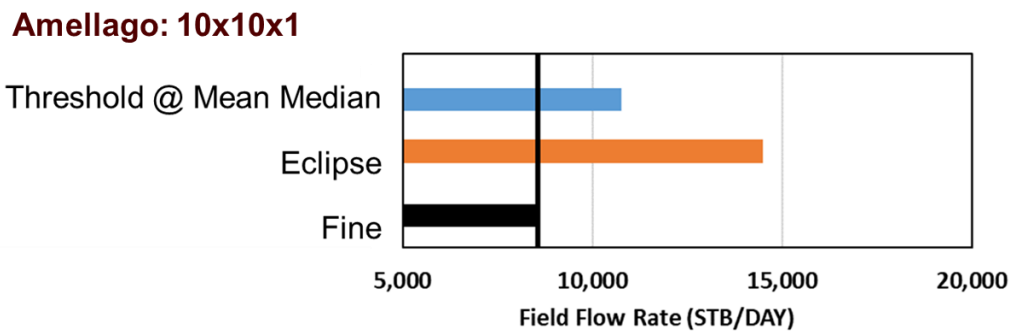

Figure 2-4 Comparison of field flow rate for Amellago model

We then tested the mean median threshold method on the Amellago carbonate outcrop model (Figure 2-4). With the same coarsen ratio 10x10, the simulation results by using the mean median threshold method is not as better as the SPE 10 model seen in the Figure 2-3. In order to better identify the well-connected sub-volume, we revisited the

concept of limit of detectability and use LOD to examine the well-connected sub-volume in the given upscaling region. The physical meaning of the well-connected sub-volume should represent the system that reaches the pseudo steady-state condition.

2.2 Analysis of Diffuse Source Distribution

The choice of the distribution of diffuse source (or sink) to help describe the sub-volume that is well-connected to the coarse cell pair interface impacts the upscaling solution. The following diffuse source distribution, including threshold method and exponential method, were examined in this study:

1. Mean DTOF evaluated at a characteristic time (threshold method)

   This method evaluated the average DTOF ($\bar{\tau}$) at the characteristic time ($\bar{\tau}^2/4t=1$) for the upscaling region (Ω) using the effective pore volume weight as shown in (2.1)

$$\begin{cases} \bar{\tau}_{\Omega_L} = \sum_{ijk} V_{p,ijk} e^{-\tau_{ijk}^2/\bar{\tau}_{\Omega_L}^2} \tau_{ijk} \Big/ \sum_{ijk} V_{p,ijk} e^{-\tau_{ijk}^2/\bar{\tau}_{\Omega_L}^2}, \tau \in \Omega_L \\ \bar{\tau}_{\Omega_L} = \sum_{ijk} V_{p,ijk} e^{-\tau_{ijk}^2/\bar{\tau}_{\Omega_R}^2} \tau_{ijk} \Big/ \sum_{ijk} V_{p,ijk} e^{-\tau_{ijk}^2/\bar{\tau}_{\Omega_R}^2}, \tau \in \Omega_R \end{cases} \tag{2.1}$$

   Then we selected the maximum average diffusive time of flight from the upstream (denoted as left) and downstream (denoted as right) region as the represented value for the full upscaling region.

$$\bar{\tau}_{\Omega} = \max\left(\bar{\tau}_{\Omega_L}, \bar{\tau}_{\Omega_R}\right) \tag{2.2}$$

   When the upscaling region reached the PSS limit ($\bar{\tau}^2/4t=0.01$), we have the relationship of averaged DTOF (Nunna and King 2020).

$$4t_{PSS} = 100\bar{\tau}_{\Omega}^{2} \tag{2.3}$$

Taking Eq. (2.3) as the time of LOD, we can, consequently, form the threshold of diffuse source (or sink) as Heaviside function at the LOD was defined to identify the well-connected sub-volume region.

$$\Theta(\tau) = \begin{cases} 0, & e^{-\tau^2/4t_{pss}} < 0.018 \\ 1, & e^{-\tau^2/4t_{pss}} > 0.018 \end{cases} \tag{2.4}$$

2. Twice mean median value of DTOF (threshold method)

   Nunna et al. (2019) identifies the well-connected sub-volume region that reaches the PSS condition by estimating the LOD region as the twice median value of DTOF ($\tau_{LOD} = 2\tau_{median}$). The resulting median value of DTOF is calculated by averaging the upstream and downstream upscaling region.

$$\tau_{median} = \text{mean}\left(\tau_{median,\Omega_L}, \tau_{median,\Omega_R}\right) \tag{2.5}$$

   Subsequently, the threshold of the diffuse source (or sink) can be similarly defined as the Heaviside function with respect to twice DTOF value.

$$\Theta(\tau) = \begin{cases} 0, & \tau > 2\tau_{median} \\ 1, & \tau < 2\tau_{median} \end{cases} \tag{2.6}$$

3. Twice pore volume weighted median value of DTOF (threshold method)

   This method is the second alternative form of the twice median value of DTOF, where the median value is weighted by the pore volume of each fine cell in the upstream and downstream. The threshold of diffuse source (or sink) is then defined in the same way shown in Eq. (2.6).

$$\tau_{V_p\,median} = \max\left(\tau_{V_p\,median,\Omega_L}, \tau_{V_p\,median,\Omega_R}\right) \tag{2.7}$$

4. Pore volume weighted exponential method based on pore volume weighted median value of DTOF for each coarsen cell

   The exponential method is capable of preserving the continuity of heterogeneity compared to the threshold of DTOF. This method applied the pore volume weighted median value of DTOF for both the upstream and downstream upscaled region, as shown in Eq. (2.8). The averaged DTOF is then applied to the exponential term, to calculate the diffuse source (or sink).

   This method is similar to the porosity weighted exponential method but changing to the pore volume weighted diffuse source solution for both the near initial and PSS limit time.

   a. At the near initial time

      For the time that the upscaling region reached the near initial time ($4t_{near\,initial} = \left(2\bar{\tau}\right)^2 / 4$), we can determine the porosity weighted diffuse source solution.

$$\begin{cases} S_{ijk,\Omega_L} = V_{p,ijk,\Omega_L} e^{-\tau^2_{ijk,\,\Omega_L} / \bar{\tau}^2_{V_p\,median,\Omega_L}}, \tau \in \Omega_L \\ S_{ijk,\Omega_R} = V_{p,ijk,\Omega_R} e^{-\tau^2_{ijk,\,\Omega_R} / \bar{\tau}^2_{V_p\,median,\Omega_R}}, \tau \in \Omega_R \end{cases} \tag{2.8}$$

   b. At PSS limit time

      For the time that the upscaling region reached the PSS limit time ($4t_{PSS} = 100\left(2\bar{\tau}\right)^2$), we can determine the porosity weighted diffuse source solution.

$$\begin{cases} S_{ijk,\Omega_L} = V_{p,ijk,\Omega_L} e^{-\tau_{ijk,\Omega_L}^2 / 400\bar{\tau}_{V_p\,median,\Omega_L}^2}, \tau \in \Omega_L \\ S_{ijk,\Omega_R} = V_{p,ijk,\Omega_R} e^{-\tau_{ijk,\Omega_R}^2 / 400\bar{\tau}_{V_p\,median,\Omega_R}^2}, \tau \in \Omega_R \end{cases} \tag{2.9}$$

5. Pore volume weighted exponential method based on twice of pore volume weighted median value of DTOF for a pair of coarsen cell

   If we consider the pair of the upscaling region as a full core, taking the averaged for full cells in the upstream and downstream instead of separating averaging is another intuitive way to do it. The pore volume weighted median DTOF is then determined as a single value for the full cells.

$$\bar{\tau}_{V_p\,median,\Omega}, \tau \in \Omega \tag{2.10}$$

   By applying twice of the median value of DTOF to represent the LOD, the pore volume weighted diffuse source solution for both the near initial and PSS limit time are determined as below.

   a. At near initial time

$$S_{ijk,\Omega} = V_{p,ijk,\Omega} e^{-\tau_{ijk,\Omega}^2 / \bar{\tau}_{V_p\,median,\Omega}^2}, \tau \in \Omega \tag{2.11}$$

   b. At PSS limit time

$$S_{ijk,\Omega} = V_{p,ijk,\Omega} e^{-\tau_{ijk,\Omega}^2 / 400\bar{\tau}_{V_p\,median,\Omega}^2}, \tau \in \Omega \tag{2.12}$$

The effective intercell transmissibility for the interface of coarse cell pair is determined by the ratio of the face flux to the difference in far upstream and downstream face pressure averages.

$$\frac{1}{T^{DS}} = \frac{\Delta p^{DS}}{\mu q_f} = \frac{\bar{p}_{up}^{DS} - \bar{p}_{down}^{DS}}{\mu q_f} \tag{2.13}$$

The upstream and downstream pressures are averaged weighted by the intercell transmissibility, T_i , on their respective faces with the flux conservative term as in Eq. (2.14). The flux conservative term preserves the flux across the upstream and downstream surface. For further details, please refer to Nunna and King (2020).

$$\bar{p}^{DS} = \frac{\mu q_f}{2} + \frac{\sum_i T_i \cdot p_i^{DS}}{\sum_i T_i} \tag{2.14}$$

It remains to determine the time for this transient calculation. The development in Nunna and King (2020) shows how to distribute the source/sink terms at a large but finite time to approach the PSS limit on a well-connected sub-volume.

2.2.1 Diffuse Source Distribution Analysis

In the previous section, we considered three threshold methods and two exponential methods for the diffusive source calculation. The analysis of diffuse source distribution is also summarized in Table 2-1.

Table 2-1 Analysis of Diffuse Source Distribution

		DTOF Equation	Source/Sink Equation	Source/Sink Distribution (-)
Threshold	**DTOF evaluated at characteristic time** (Nunna et al., 2017)	$\bar{\tau}_{\Omega_{L,R}} = \sum_{ijk} V_{p,ijk} e^{-\tau_{ijk}^2/\bar{\tau}_\Omega^2} \tau_{ijk} \Big/ \sum_{ijk} V_{p,ijk} e^{-\tau_{ijk}^2/\bar{\tau}_\Omega^2}$ $\bar{\tau}_\Omega = \max\left(\bar{\tau}_{\Omega_L}, \bar{\tau}_{\Omega_R}\right)$	$\Theta(\tau) = \begin{cases} 0, & e^{-\tau^2/4t_{pss}} < 0.018 \\ 1, & e^{-\tau^2/4t_{pss}} > 0.018 \end{cases}$	
	Twice mean median DTOF (Nunna et al., 2019)	$\tau_{median} = \text{mean}\left(\tau_{median,\Omega_L}, \tau_{median,\Omega_R}\right)$	$\Theta(\tau) = \begin{cases} 0, & \tau > 2\tau_{median} \\ 1, & \tau < 2\tau_{median} \end{cases}$	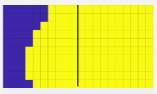
	Twice pore volume weighted median DTOF	$\tau_{median}(V_p) = \max\left(\tau_{median,\Omega_L}, \tau_{median,\Omega_R}\right)$	$\Theta(\tau) = \begin{cases} 0, & \tau > 2\tau_{median}(V_p) \\ 1, & \tau < 2\tau_{median}(V_p) \end{cases}$	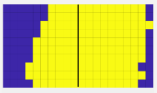
Exponential	**Pore volume weighted exponential method based on $\tau_m(V_p)$ for each coarsen cell**	$\begin{cases} \bar{\tau}_{median,\Omega_L}(V_p), \tau \in \Omega_L \\ \bar{\tau}_{median,\Omega_R}(V_p), \tau \in \Omega_R \end{cases}$	$\begin{cases} S_{ijk,\Omega_L} = V_{p,ijk,\Omega_L} e^{-\tau_{ijk,\Omega_L}^2/4t_{pss}}, \tau \in \Omega_L \\ S_{ijk,\Omega_R} = V_{p,ijk,\Omega_R} e^{-\tau_{ijk,\Omega_R}^2/4t_{pss}}, \tau \in \Omega_R \end{cases}$	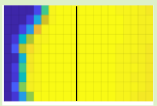
	Pore volume weighted exponential method based on $\tau_m(V_p)$ for a pair of coarsen cells	$\bar{\tau}_{median}(V_p), \tau \in \Omega$	$S_{ijk,\Omega} = V_{p,ijk,\Omega} e^{-\tau_{ijk,\Omega}^2/4t_{pss}}, \tau \in \Omega$	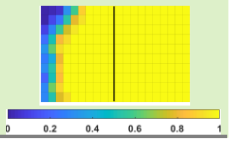

The top three rows are threshold methods in this table, and the bottom two rows are exponential methods. The equations used in each diffuse source/sink calculation and criteria are listed on it. The last column shows the diffuse source/sink distribution on this pair of cells. Both the threshold and exponential methods can capture the permeability heterogeneity in the left cell (i.e., the sharp transition of permeability). Still, they show a different way to distribute the source/sink strength. The threshold methods have shown that the source/sink strength beyond the calculated threshold has been removed (denoted as blue color), and the cells in the threshold have the same source/sink strength (marked as yellow color).

On the other hand, the exponential method has shown a transition zone that source/sink strength gradually decreases to zero. Another observation is that the twice

mean median DTOF method has perfectly captured the permeability distribution in the threshold method. However, the mean median DTOF method may lack of a reasonably physical meaning to support it. We proposed the exponential method, which also captured the permeability distribution, and our approach relies on the capacity of cell pore volume. The later part of this chapter will validate which way provides better upscaling results through numerical experiments.

2.2.2 Pressure Averaging Surface Analysis

Before we move to the numerical experiments, another analysis required for the exponential method is how to define the pressure average surface. In contrast to the threshold method, we don't have clear cutoff (or constraint) for defining the pressure surface, as shown in Figure 2-5. Here, we proposed two method to defining the pressure surface. First method is defined the pressure front on the LOD. Following the well testing literature, the PSS limit time is defined as Eq. (2.15).

$$e^{-\tau^2/4t} \geq 0.99 \text{ or } t_{PSS} = 100\tau_m^2 \tag{2.15}$$

We then need to defined the LOD for pressure front in the DS construction. If LOD at a given time that the pressure transient source strength is negligible beyond the region, the relationship can be written as Eq. (2.16).

$$e^{-\tau_{LOD}^2/4t} < 0.018 \text{ or } \tau_{LOD}^2/4t > 4 \tag{2.16}$$

Then the LOD at PSS limit can be defined as 40 times median DTOF value which implies as the PSS time, as shown in Eq. (2.17).

$$\tau_{LOD} = 40\tau_m \tag{2.17}$$

Another method is simply defined the LOD at the twice median value of DTOF. In the linear flow, the median DTOF would be the halfway across the upscaling region of DTOF has, as shown in Eq. (2.18). We will test which one is better later in numerical experiments.

$$\tau_{LOD} = 2\tau_m \tag{2.18}$$

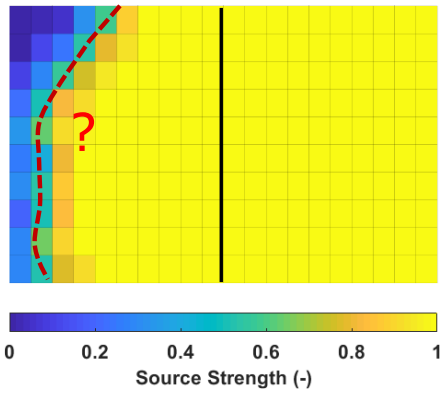

Figure 2-5 Illustration of the issue of choosing the pressure surface

2.2.3 Numerical Experiments

In this section, we will utilize the reservoir scale sector models to examine the further novel upscaling workflow. The first model is the SPE10 Comparative Solution (Christie and Blunt 2001), the second is the Amellago Carbonate outcrop model provided by the Carbonate Reservoir Group at Heriot-Watt University for research purposes (Geiger 2016). The reservoir parameter and simulation schedule has reported in section 1.6.

2.2.3.1 Analysis of Diffuse Source Distribution

We considered a 10x10 areal coarsen ratio for both SPE 10 and Amellago model as what we shown in the section 2.1. Let's look the SPE10 results first. The simulation results and L2 Norm error are shown in Figure 2-6. The diffuse source/sink distribution for each method are listed in the bottom for reference. This bar chart shows the well flow rates for each well with different color, and summed it up to the total rate. The well flow rate is the slope of cumulative production or injection and we found out that is more useful to compare with coarse model.

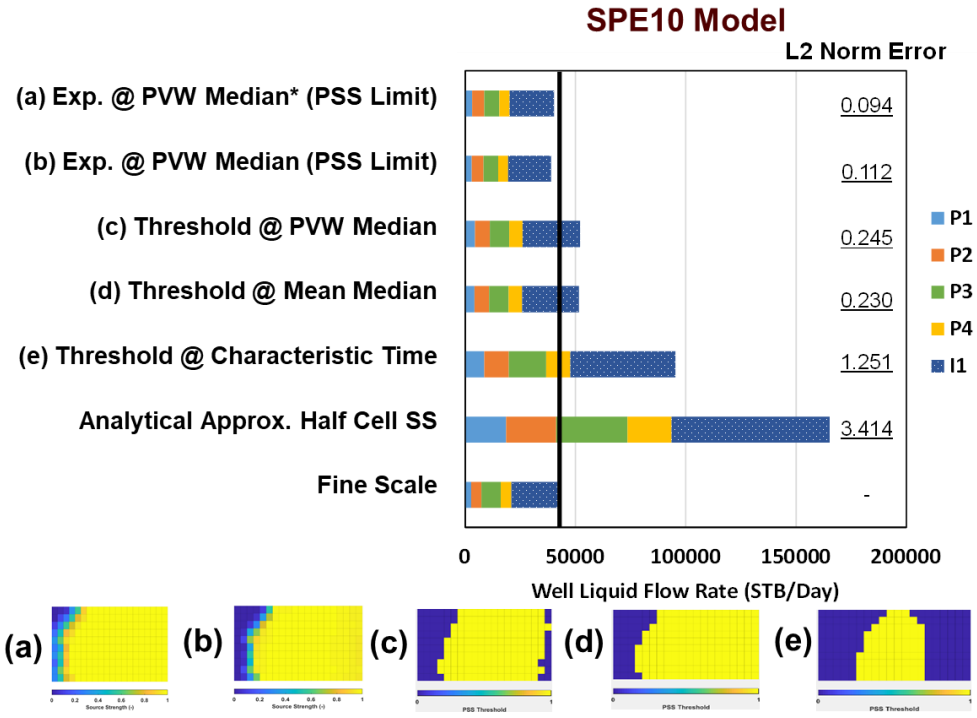

Figure 2-6 Comparison the simulation result and L2 Norm error for diffuse source/sink distribution methods for SPE 10 model; The diffuse source/sink distribution for each method are listed in the bottom for reference.

Following the sequence of bar from bottom to top. The first bar represents the fine scale results and we put the black vertical line on it to compare with the following upscaling methods. We also compared the analytical approximate half-cell SS upscaling as a reference of the industry standard upscaling. This method is commonly used in the commercial upscaling method. The following three bars are threshold methods and top two bars are exponential methods. Noted that the mean median threshold method provides a good match with the fine scale simulation as proposed from Nunna et al. (2019).

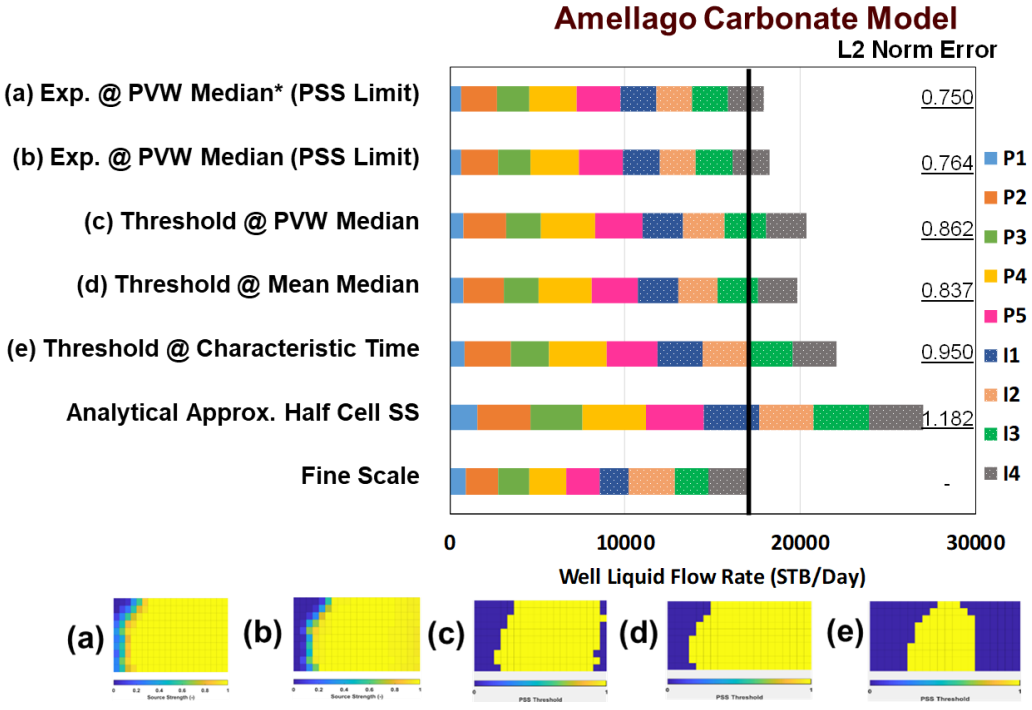

Figure 2-7 Comparison the simulation result and L2 Norm error for diffuse source/sink distribution methods for Amellago model; The diffuse source/sink distribution for each method are listed in the bottom for reference.

Although the mean median method has such a good result, the exponential methods even improved the upscaling results and gave the smallest L2 Norm error. Besides, in the two exponential methods, the Pore volume weighted exponential method based on median DTOF for a pair of coarsen cells are better than the other exponential method. The similar results are validated again in the Amellago carbonate model. Hence, we would then suggest apply this method for following study (Figure 2-7).

2.2.3.2 Analysis of Pressure Averaging Surface

In this section, we consider three areal coarsen ratio (1x1, 3x3, and 5x5) and a uniform vertical coarsen ratio (x6) in the upscaling calculation for analyzing the two pressure averaging surface methods. Two numerical reservoir results (SPE 10 and Amellago model) are reported here and both shows the similar trends, as shown in Figure 2-8 and Figure 2-9.

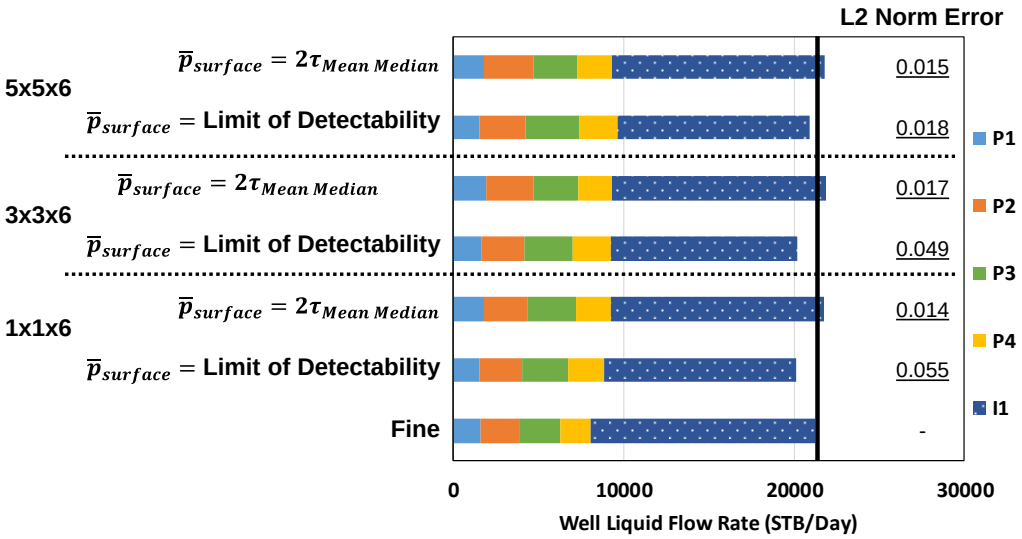

Figure 2-8 Comparison the SPE 10 simulation result and L2 Norm error for pressure averaging methods

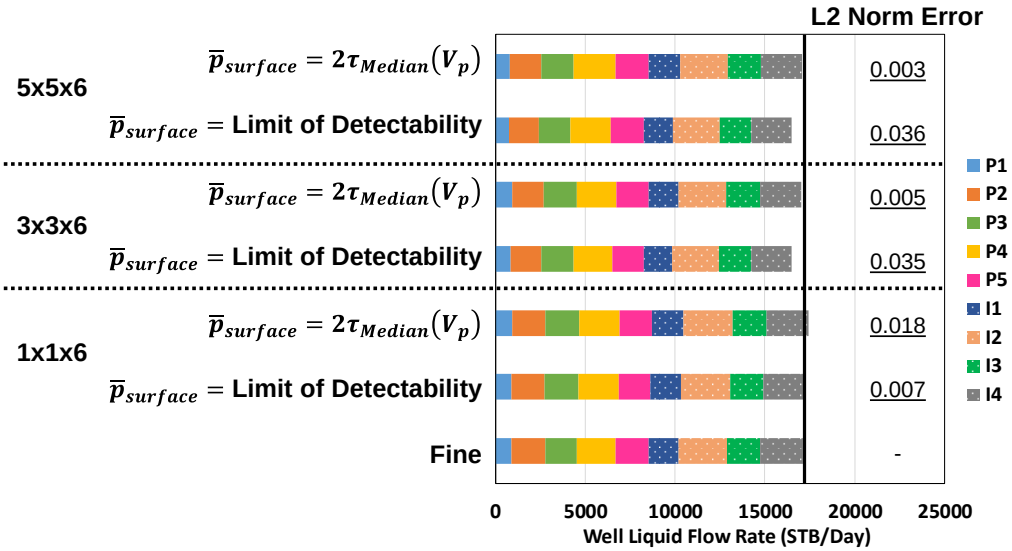

Figure 2-9 Comparison the Amellago carbonate model simulation result and L2 Norm error for pressure averaging methods

These figures show the well flow rate for each well and sum up to total rate with the L2 norm error listing on it. Here, we use Figure 2-8 to describe the results. The bar chart shows the range of two pressure averaging surface method are not large. Actually, they are both closed to the fine scale results because the benefits of the better diffuse source/sink distribution. However, in these two pressures averaging methods, the twice median DTOF consistently works better than the other method.

2.3 Discussion

The Diffuse Source transmissibility upscaling has been studied for couple of years (Liu et al. 2019, Nunna and King 2020, 2017, Nunna et al. 2019, Nunna et al. 2015, Liu et al. 2020, Syed et al. 2020). Unlike other transmissibility upscaling

algorithms, this method is completely localized without the need to set the outer boundary. This advantage is accompanied by the issue of the ambiguous pressure averaging surface. In our study, the answer depends on which type of diffuse source/sink distributions were used in the upscaling calculation. Two types of diffuse source/sink distributions have been discussed in this study: the threshold and exponential methods. The threshold method has a clear inner boundary separated the cells with or without the source/sink strength, and therefore could easily define the pressure averaging surface. The exponential diffuse source/sink distributions, on the other hand, don't have a clear inner boundary. We studied two methods to identify the pressure averaging surface for the exponential method, and both ways are based on the concept of LOD. In our study, defining the LOD at the twice median value of DTOF shows a better result than utilizing the LOD at the PSS limit can be defined as 40 times the median DTOF value. This result may not be a coincidence and could be related to the twice mean median DTOF threshold method, reported in the literature as the most accurate threshold method (Nunna et al. 2019). The possible physical meaning is that the flow behavior in the pair of coarse cells is linear flow, and, for the linear flow, DTOF is twice the median DTOF.

2.4 Chapter Summary and Conclusions

In this chapter, we reported the improvement of the existing Diffuse Source upscaling with a better distributed source/sink strength and pressure averaging method. Previous DS Upscaling well captures the heterogeneity distribution for high contrast model by applying a sharp threshold and validates in SPE 10 model. This study testing

against carbonate reservoir model with a much boarder distribution of heterogeneity. The results made from threshold method becomes unstable in this kind of model.

The exponential form of Source/Sink distribution and new pressure averaging method proposed from this studied shows an improvement of the DS upscaling and has been validated on two reservoir sector models (SPE10 and Amellago carbonate outcrop). We conclude that a better physical based DS upscaling contains three keys:

1. DS source/sink strength distribution:
    - Apply the exponential method instead threshold method is better to capture the transition of the DS source/sink distribution
    - Apply pore volume weighted based diffusive time of flight (DTOF) instead pure statistics based DTOF is better to align with the cell intrinsic properties
2. Pressure averaging surface:
    - Use pressure front at twice $\tau_m\left(V_p\right)$ instead at limit of detectability (LOD) of DTOF works better for the exponential method
3. Include the flux conservative connection in the pressures averaging calculation always provides better results

CHAPTER III

NEAR WELL UPSCALING[†]

In this chapter, we start with reviewing the Peaceman well index calculation. The study of near well upscaling includes both the well index upscaling and well cell face upscaling. The resulting near well upscaling method then combines with the improved DS upscaling method, and is validated in three sector of reservoir models (SPE10, Amellago carbonate reservoir, and FSU shale reservoir). The last but not least, we report the analysis of time of validity for the Peaceman well index

3.1 Peaceman Well Index Calculation

As an introduction to the near well upscaling, we return to Peaceman's derivation and a numerical refinement study of 2D single-phase flow in a homogeneous reservoir model with a single well at the center of the model. We will examine both steady state and pseudo steady state flow solutions. Peaceman initially utilized radial analytic solutions to determine the boundary conditions for his refinement study, but later showed that the well index was not strongly influenced by the choice of boundary condition, so long as the well was sufficiently far from the well cell boundary (Peaceman

---

* Part of this section is reproduced with the permission from Liu, C.H., Nunna, K., and King, M.J. 2020. Application of Diffuse Source Basis Functions for Improved near Well Upscaling. 2020 (1): 1-31. DOI: 10.3997/2214-4609.202035156.
* Part of this section is reproduced with the permission from Syed, Imroj, Liu, Ching-Hsien, Kelkar, Mohan G., and Michael J. King. "Improved Distance Based Upgridding and Diffuse Source Upscaling for High Resolution Geologic Models." Paper presented at the SPE Annual Technical Conference and Exhibition, Virtual, October 2020. DOI: 10.2118/201727-MS.

1978, 1983). For these calculations, the bottomhole flowing pressure is set to zero, and the outer boundary is also an isobar. For steady state flow, the outer boundary pressure is specified and the flow rate is to be determined. For pseudo steady state flow, the flow rate of the well is specified, total flux through the outer boundary vanishes, and the outer boundary pressure is to be determined. The outer boundary pressure is a connection pressure, and the fine scale flow equations are based upon twice the intercell transmissibility.

The results of our convergence study are shown in Figure 3-1. Here the pressure computation is on a $(2N+1)\times(2N+1)$ cell grid, ranging from $N=0$ (one cell) to $N=40$, with a bottomhole flowing pressure of $p_{wf}=0$ use for reference, and normalized to the value for μq_w. From bottom to top in the figure, other than the p_{wf} reference profile, four pressure profiles are included on the plot, although only three are evident.

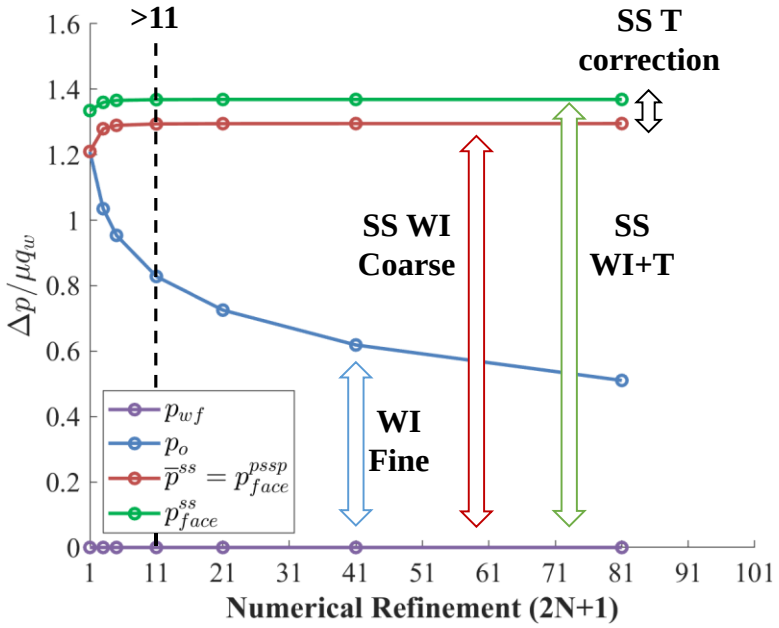

Figure 3-1 Variation of the normalized numerical pressure drop with respect to numerical refinement on a $(2N+1)\times(2N+1)$ cell grid with the well at the grid center. Here, $p_{wf}=0$ is the well bottomhole flowing pressure, and p_o, $\bar{p}^{SS}$, p_{face}^{PSSP} and p_{face}^{SS} are described in detail in the text.

First, we have the fine scale Peaceman well cell pressure, p_0. This profile shows the pressure difference between the bottomhole flowing pressure and the fine scale well cell pressure, which is obtained from the fine scale well index. Second, we have the pore volume weighted average of the steady state solution, $\bar{p}^{SS}$, and the outer boundary PSS pressure, p_{face}^{PSSP}, which are identical. This equality is rigorous in one dimension (Nunna and King 2020), but it seems to hold true in higher dimensions for radial dominated flow, even in the presence of heterogeneity. Interestingly, Peaceman also took advantage of the equivalence between the SS and PSS solutions, where he re-derived the Dietz

shape factors for rectangular domains based upon the expression for p_0 (Peaceman 1990).

If we utilize well index upscaling, then the pressure difference $p_{face}^{PSSP} - p_{wf} = \bar{p}^{SS} - p_{wf}$ determines the coarse well index. It is remarkable how close to a converged value we are for $\bar{p}^{SS}$, even on a coarse 5×5 grid (N=2), showing the importance of Peaceman's p_0 construction. The figure includes the normalized p_{face}^{SS} profile, which also converges quickly. Convergence of the calculation is evident once we reach a grid size larger than 11, consistent with what Peaceman (1990) suggested for the minimum distance from the well to the nearest boundary (N=5 cells).

The pressure difference $p_{face}^{SS} - \bar{p}^{SS}$ is also shown in the figure. We will return to a discussion of how it can be used to determine the half cell transmissibility for each coarse cell face. We will show that this is not as accurate a calculation as the use of a mixed steady state (SSM) pressure solution, once we go beyond a single cell, but it is consistent with the simple analytic construction provided by Peaceman (1978).

3.2 Well Index Upscaling

Three possible calculations for the upscaling of the well index are shown in Figure 3-2. The results of two are shown in Figure 3-1: Steady State flow and PSS flow with an outer boundary isobar (PSS(P)).

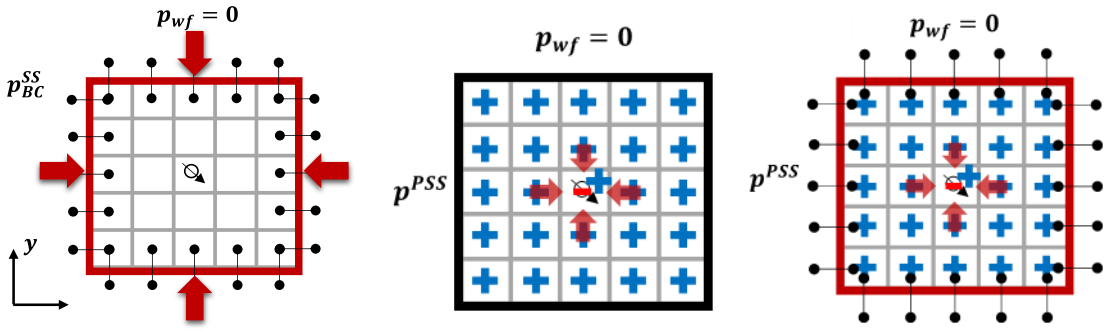

(a) (b) (c)

Figure 3-2 Schematic showing (a) Steady state well index upscaling with a specified pressure isobar on the outer boundary (SS), and a total inflow to the well to be calculated; (b) Pseudo steady state well index upscaling with no flow outer boundary (PSS(Q)), and the summation of source terms equals the well flux; (c) Pseudo steady state well index upscaling with an unknown isobar pressure (PSS(P)) on the outer boundary, and the summation of source terms equals the well flux.

A third possible calculation is PSS flow with a no flow outer boundary (PSS(Q)), where the outer boundary pressure is obtained from a transmissibility weighted average, following Eq., however, we find that the pressure drop in this calculation is generally larger than for PSS(P) and is not consistent with the SS solutions. Example solutions and flow patterns for all three choices are shown in Figure 3-3 (homogeneous model) and Figure 3-4 (heterogeneous model). The numerical calculations and the streamline trajectories have been developed using the MATLAB Reservoir Simulation Toolbox (Lie 2019).

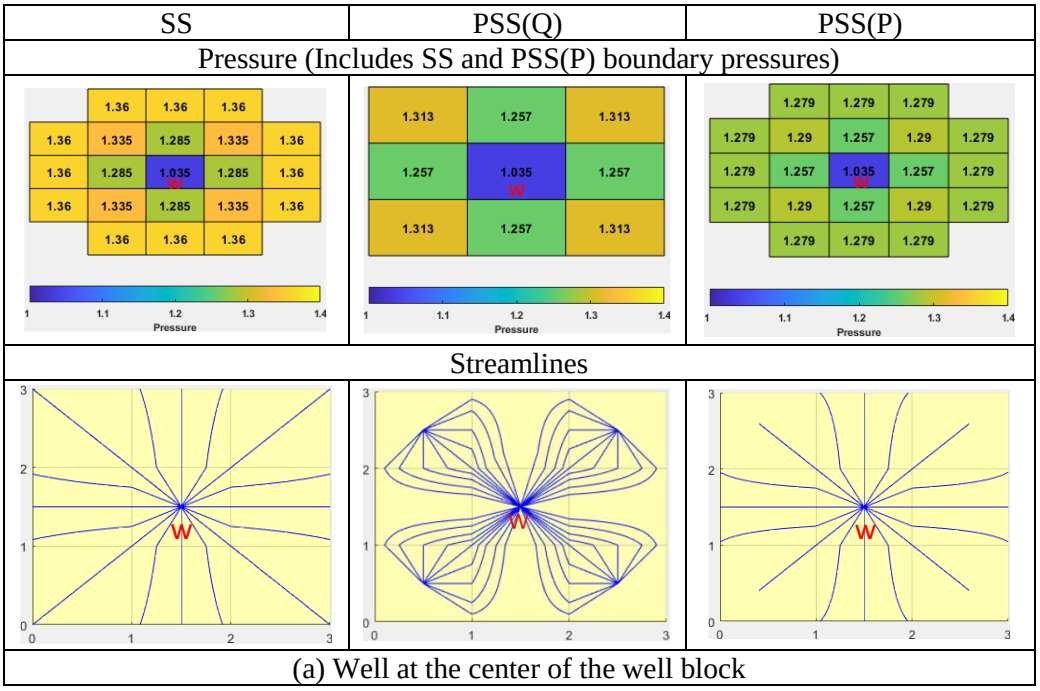

Figure 3-3 Streamline flow visualization for the well index upscaling in a 3x3 homogeneous model with (a) Well at the center of the well block and (b) Well off center in the well block. The first row is the pressure map relative to a bottomhole flowing pressure of $p_{wf} = 0$ with a unit value for μq_w. The second row are the streamlines resulting from the velocity field. The well location is denoted as "w".

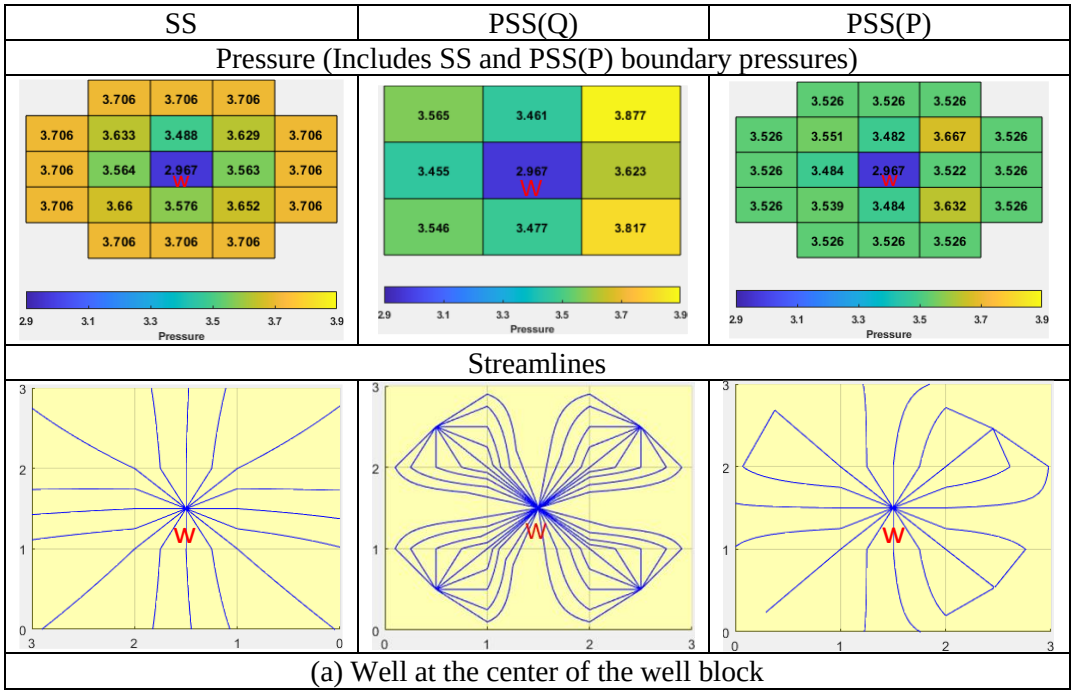

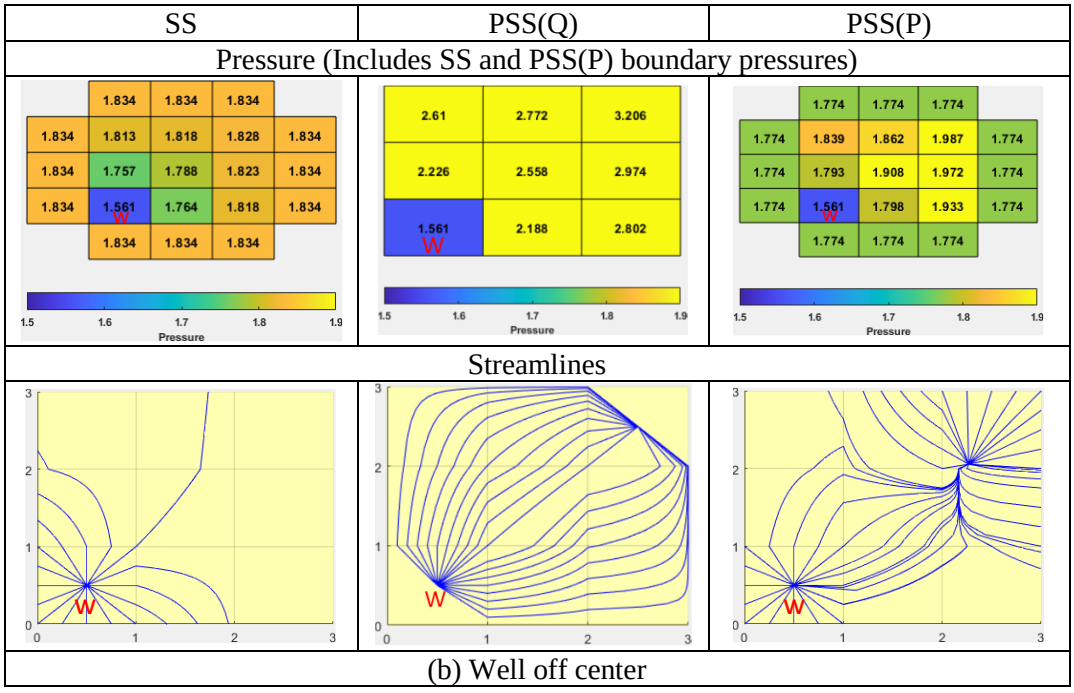

Figure 3-4 Streamline flow diagnostics for the well index upscaling in a 3x3 heterogeneous model with (a) Well at the center of well block and (b) Well off center in the well block. The first row is the pressure map relative to a bottomhole flowing pressure of $p_{wf} = 0$ with a unit value for μq_w. The second row are the streamlines resulting from the velocity field. The well location is denoted as "w".

Solutions in these figures are shown on a 3x3 coarse cell for a centered well and for an off-center well, for both a homogeneous model and a heterogeneous model. If we first examine the SS solutions, it is seen that flow is from the boundary of the coarse cell to the well, as desired. The pressure drops and streamlines shown for the PSS(P) solutions are similar to the SS solution. However, since the total flux across the outer boundary of the model vanishes, additional source terms on the interior of the coarse cell will appear. For PSS(Q), the flow patterns are significantly different from both the SS and PSS(P) solutions. Because of the no flow outer boundaries, flow is transverse to the outer boundary and source terms will again occur within the upscaling region.

In addition to having very different flow patterns, the PSS(Q) pressure drops are, in general, larger than the PSS(P) values. It will be shown that PSS(Q) will provide low estimates of the well index that may not be consistent with near well flow. As the PSS(P) and SS pressure drops are essentially identical, we will utilize the SS solution for the upscaling of the well index, Eq. (1.34), as the flow patterns are more consistent with expectations. The SS solution is also somewhat easier to implement as it has no issues with isolated pay (Nunna and King 2020).

3.3 Well Cell Face Transmissibility Upscaling

A previous study that focused on the development and testing of diffuse source (DS) upscaling for the intercell transmissibility also utilized the PSS(P) calculation for the well index (Nunna et al. 2019). Examination of the detailed results is shown in Figure 3-5 for the Amellago Carbonate outcrop model. These plots provide a comparison

of the coarse scale face fluxes and the summed fine scale fluxes for horizontal (x direction) and vertical (z direction) flow after 1 month of flow for 1x1x6, 2x2x6 and 3x3x6 coarsening ratios for the DS(T) + PSS(P) (WI) upscaling. This quantile-quantile plot indicates how the calculated coarse flux deviates from the fine flux, with the largest fluxes being in the near well region. The L2-Norm of the correlation is used to quantify the error.

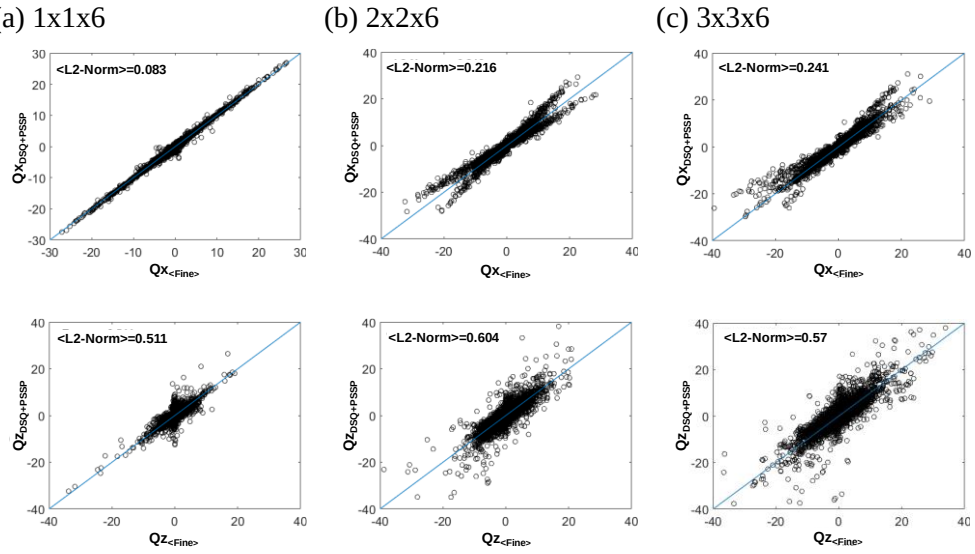

Figure 3-5 DS+PSS(P) upscaling comparison of the coarse and summed fine scale face fluxes in the x direction (first row) and z direction (second row) at 1 month for (a) 1x1x6, (b) 2x2x6, and (c) 3x3x6 coarsening ratios. The L2-Norm error is provided to summarize the total error.

As the areal coarsening ratio increases, we see an increased deviation of the coarse flux from the fine flux, separating into multiple trends, particularly in the horizontal flow. More detailed local examination shows that the flux error trends are controlled by the placement of the well in the coarse cell. 2x2 upscaling shows two trends, associated with the placement of wells in each corner of the coarse well cell. 3x3

upscaling shows three trends, associated with the placement of wells in the corners, faces and center of the coarse well cell. These calculations utilize vertical fully completed wells, so no trend in the error is expected or seen for the vertical flow.

In these calculations, the PSS(P) calculation for the well index, and the flow from cell to well, is consistent with a steady state solution, as just discussed. However, in the PSS/DS calculation for the transmissibility, the flow into the cell follows a diffuse flow pattern and pressure drop, as this is the long time limit of the transient solution. In contrast, in the presence of a well, represented as a point source (or sink), the long time limit of the transient solution is steady state flow, as shown in Figure 3-6.

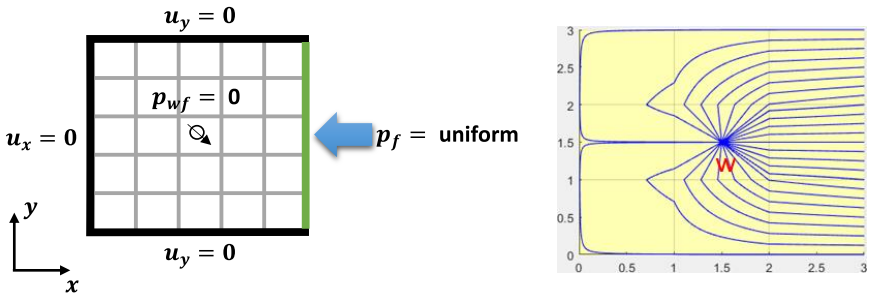

Figure 3-6 Schematic showing well cell steady state face transmissibility upscaling with a bottomhole flowing pressure equal to zero, and an isobar pressure on the one flowing boundary (SSM).

In the calculation of Figure 3-6, as in the PSS/DS upscaling calculation for the transmissibility, we have localized the flow calculation to a single coarse cell face, again modelled as a pressure isobar. The steady flow calculation now provides us with the relationship between the bottomhole flowing pressure of the well, the cell face pressure, and the flow rate of the well.

$$\frac{1}{WI}+\frac{1}{T_f}=\frac{\left(p_{BC}^{SSM}-p_{wf}\right)}{\mu q_f^{SSM}},\quad f=1,2,3,4 \tag{3.1}$$

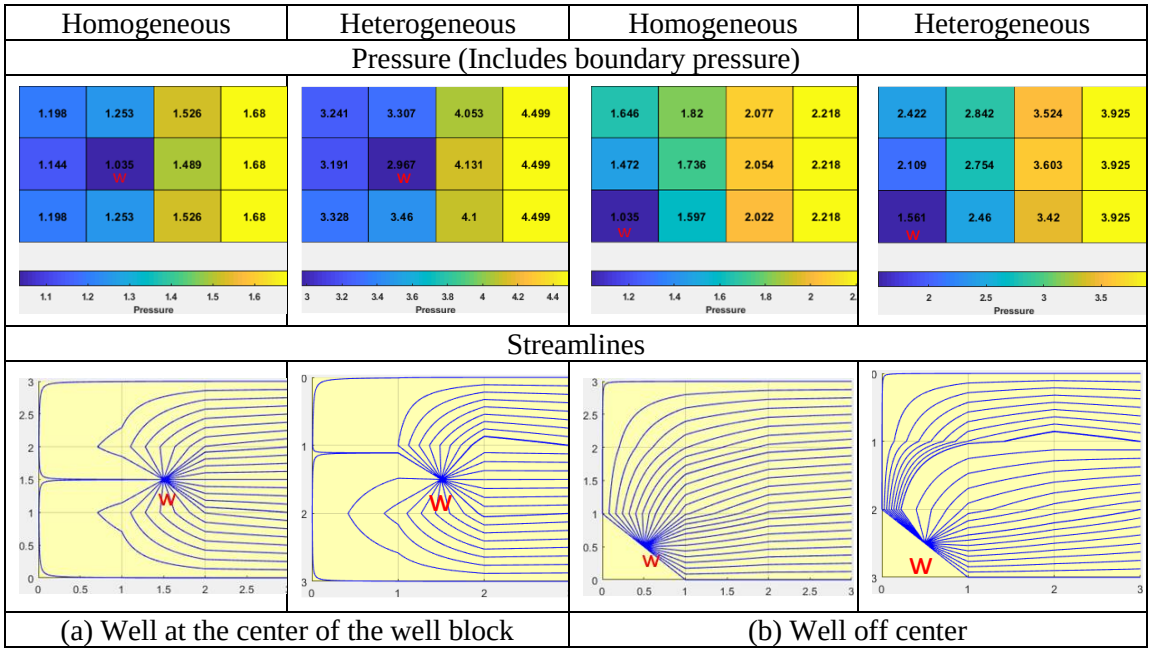

Figure 3-7 Streamline flow visualization for the SSM cell face transmissibility upscaling in a 3x3 model with flow from the right face for (a) Well at center of coarse cell (b) Well off center, for a homogeneous model and for a heterogeneous model; The first row is the pressure map relative to a bottomhole flowing pressure of $p_{wf}=0$ normalized to the value of μq_w. The second row are the streamlines resulting from the velocity field. The well location is denoted as "w".

If the well index has been calculated, then this upscaling calculation determines the half cell transmissibility for the flowing cell face. It is combined in the usual fashion (harmonic sum) with the half cell transmissibility in the adjacent cell determined using DS upscaling. The result is an intercell transmissibility that combines the point source flow pattern in the well cell with the diffuse source flow pattern in the adjacent cell. Example well cell solutions are shown in Figure 3-7.

Comparison with the flow fields for the well index upscaling shown in Figure 3-3 and Figure 3-4 show that these flow patterns may differ from the previous calculations in the fine scale well cells, not just in the overall flow. Eq. (3.1) also places a constraint on the value of the well index. If the value for WI is too low, then the implied value for T_f may be negative. This inconsistency may arise in the presence of heterogeneity for the PSS(Q) calculation of the well index, but not for the SS or PSS(P) calculations. We will provide an example to further demonstrate this issue later.

3.4 Near Well Upscaling

We have specified the methods that will be used for well index and well cell face transmissibility upscaling. These calculations will be combined with the DS transmissibility upscaling for all cells other than the well cells, as shown in chapter 2. The key element of our approach is the use of superposition to ensure that the local calculations are consistent with an arbitrary global flow field. We will use the numerical examples in the following sections to show that the combination of DS (T) + SS (WI) + SSM (T) upscaling will provide the most accurate upscaling approach. The combination is summarized in Figure 3-8.

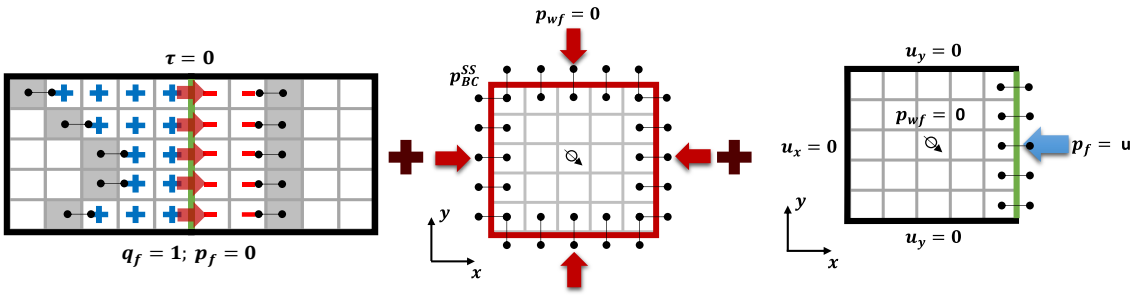

(a) DS Transmissibility Upscaling **(b) SS Well Index Upscaling** **(c) SSM Face Transmissibility Upscaling**

Figure 3-8 The most accurate upscaling approach is based on (a) DS intercell transmissibility upscaling, (b) SS well index upscaling, and (c) SSM face transmissibility upscaling

Here, the DS upscaling differs from the PSS upscaling in that the source and sink terms only occur on sub-volumes that are well connected to the shared flowing face. As in the PSS/DS upscaling, for the flowing faces in the SS and SSM calculations, we specify connection pressures and utilize twice the (heterogeneous) fine scale intercell transmissibilities around the boundaries of the coarse cells.

In addition to this calculation, we will examine two variations of the upscaling methodology as sensitivities. The first was alluded to in the discussion of the steady state well index upscaling of Figure 3-2. In this calculation, we have calculated pressures, as discussed, but we also obtain the flux through each of the four cell faces. These fluxes, together with the pore volume weighted steady state pressure, can also be used to determine the face transmissibility.

$$\frac{1}{T_f^{SS}} = \frac{\left(p_{face}^{SS} - \bar{p}^{SS}\right)}{\mu q_f^{SS}}, \quad f = 1,2,3,4 \tag{3.2}$$

These calculations will be tested and indicated as the SS(T) calculation for the transmissibility. We will show that this calculation does not perform as well as Eq. (3.1), perhaps because unlike Eq. (3.1), it includes flow coupling with the remaining cell faces. The other variation is to estimate the well index from the cell face SSM calculations. In each SSM calculation, we can obtain the pore volume weighted average pressure and use that to define a "directional" well index, WI_f.

$$\frac{1}{WI_f} = \frac{\left(\bar{p}_f^{SSM} - p_{wf}\right)}{\mu q_f^{SSM}}, \quad f = 1,2,3,4, \quad WI = \sum_{f=1}^{4} WI_f \tag{3.3}$$

The expression for the well index follows by equating the cell pressures obtained from each of the cell face transmissibility calculations, $\bar{p}_f^{SSM} = \bar{p}_0$. We will show that this calculation does not perform as well as Eq. (1.34), perhaps because the superposition of these four solutions will not, in general, generate an isobar on the outer boundary of the coarse well cell. These calculations will be indicated as the SSM(WI) calculation for the well index.

Before examining the performance of the near well upscaling methods on specific reservoir models, we will perform numerical experiments similar to those of Peaceman to show the relationship between our current work and Peaceman's well index calculation (Peaceman 1978, 1983). We have shown that the use of the steady state $\bar{p}^{SS}$ pressure for the definition of the well index is consistent with Peaceman's numerical convergence study, and is identical to p_0 for a single cell, for a well located at the center of a homogeneous reservoir model. Now we extend the approach to consider near well reservoir heterogeneity and the off center placement of a well perforation within a

simulation well block. Specifically, in Figure 11 we examine the equivalence of the SS and PSS(P) upscaling for the well index for four calculations.

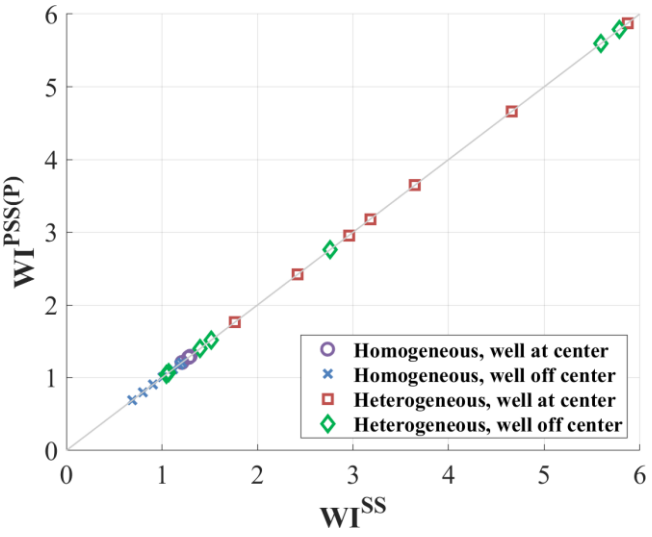

Figure 3-9 Analysis of well cell flow Q-Q cross plot for the SS well index and the PSS(P) well index.

In Figure 3-9, we show a Q-Q cross plot of the well index calculated using either $\bar{p}^{SS}$ or p_{face}^{PSSP} for a well placed in each of the nine fine cell locations within the model. The plot shows that the two well index calculations are essentially identical, both for homogeneous and heterogeneous models, and for any position within the coarse cell.

However, a difference does arise when we determine the cell face transmissibility, shown for each of the nine locations in a 3x3 coarse grid cell, in Figure 12.

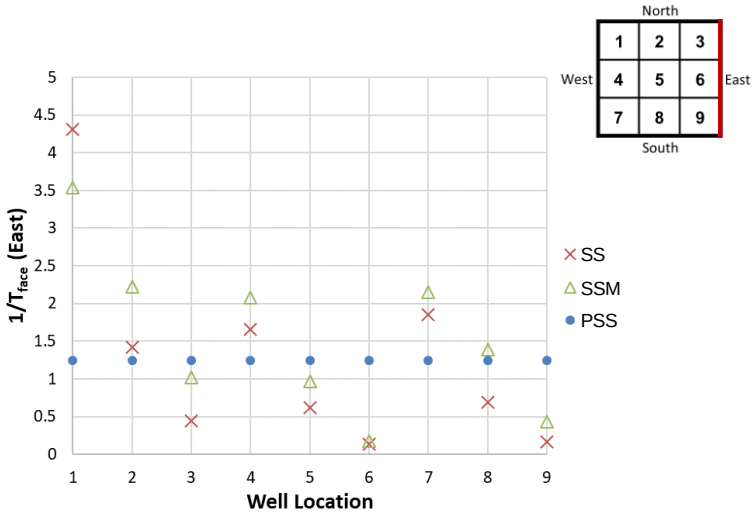

Figure 3-10 The half cell face transmissibility for each upscaling method and placement of well location in the 3x3 heterogeneous well model using the east face as an example.

For the SS calculation, we follow Eq. (3.2) while for the SSM flow we follow Eq. (3.1). The comparison is shown in Figure 3-10, again for each location within a heterogeneous model. This figure also shows the PSS half cell face transmissibility, for reference, which is independent of the well location as it is calculated for a diffuse sink. This difference in transmissibility gives rise to the discrepancies shown in Figure 3-5.

3.5 Validation: Example with a Highly Heterogeneous Near-Well Model

We start with an example of near well upscaling in a highly heterogeneous 3x3 region extracted from the bottom layer of the Amellago model. It has high contrast and low permeability and will show large variations in the upscaled properties between approaches. In this specific case, extremely small values of the upscaled well index were

observed due to the wide range of variation in permeability in this well block, shown in Figure 3-11.

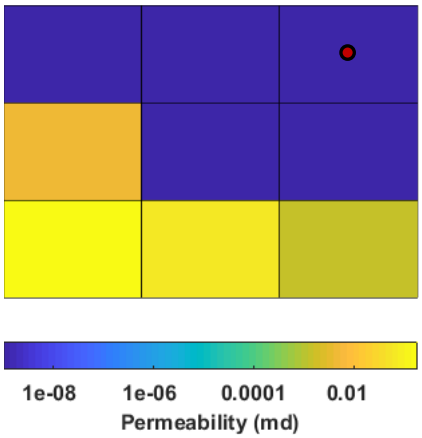

Figure 3-11 Permeability distribution (md) for the case of an extremely heterogeneous near well model. The well location shown by the red dot.

The results of each well index upscaling calculation are shown in Table 1. The SS and PSS(P) well index upscaling calculations give essentially identical well index values, although the flow patterns are different. In contrast, the PSS(Q) well index is about two times smaller than the other methods. It is expected that the PSS(Q) calculation will always give a lower estimate compared to PSS(P).

Table 3-1 Upscaled well index values for Figure 3-11 using the SS, PSS(Q), and PSS(P) methods

	SS	PSS(Q)	PSS(P)
WI [md*m]	1.152×10^{-12}	6.33×10^{-13}	1.151×10^{-12}

Figure 3-12 shows the streamline flow visualization of each well index upscaling solution for this case. The SS well index upscaling shows strong near-radial flow

behavior irrespective of the heterogeneity. The figure includes the magnitude of the flux on the faces of the well block to highlight the variability of the flux on each face. The quantity of flux on each face, as shown in Figure 3-12 (a), will then be used to calculate the face transmissibility for the SS transmissibility upscaling calculation.

The PSS(Q) method, which has a no flow boundary on the face of well block, generates an injector-producer flow pattern with the source term due to fluid expansion in the opposite corner of the model from the well, as shown in Figure 3-12 (b). The PSS(P) calculation, which has vanishing total flux but an isobar pressure boundary on the face of the well block which allows flow across the face, forms a more complicated flow pattern. Here several cells act as source terms and local stagnation lines exist due to the competition of flow through the cells in well block to the wellbore or through the face of the well block to the wellbore, as shown in Figure 3-12 (c). The values of the SS and PSS(P) upscaled well indices are essentially identical. It can be shown that in one dimension that these two quantities must be equal, but it is perhaps surprising that they have close to identical values despite the difference in flow patterns. In detail, it is clear that most of the pressure gradient is in the well cell itself, so the differences in the large scale flow patterns are not as important. In contrast, PSS(Q) shows a reduced angular flow in the fine well cell (180^o vs. 360^o), and the well index is consequently reduced by approximately a factor of 2.

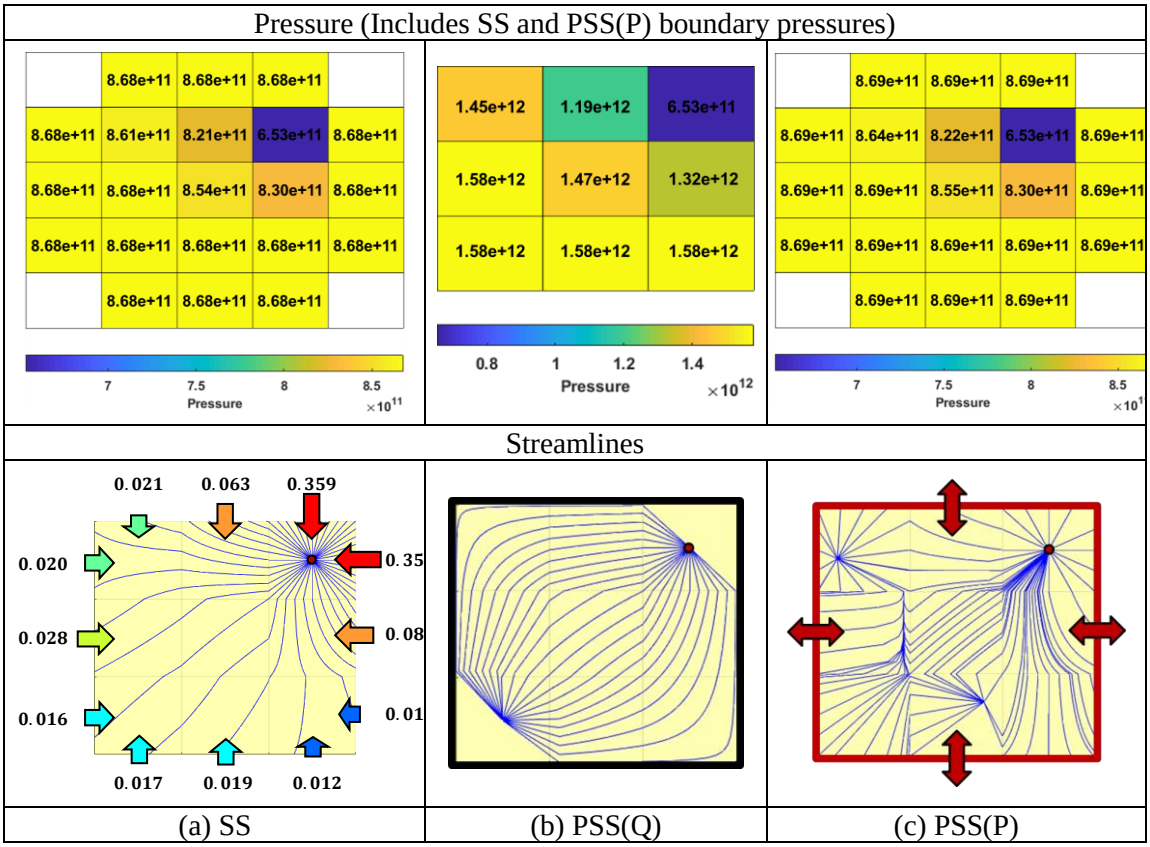

Figure 3-12 Streamline flow visualization for the (a) SS, (b) PSS(Q), and (c) PSS(P) well index upscaling in the highly heterogeneous model. The first row is the pressure map relative to a bottomhole flowing pressure of $p_{wf} = 0$ with a unit value for μq_w. The second row are the streamlines resulting from the velocity field. The red dot represents the well location.

We now investigate the streamline flow visualization of the SSM flow pattern and two variations of SSM method based on PSS(Q) and PSS(P), and the calculation of the SS face transmissibility. Recalling Eq. (3.1), the well index may be obtained from any of three methods, and the face transmissibility by difference. The streamline flow visualization for the SSM calculation for each face of the well block shows how the streamlines are distorted by the heterogeneity and no flow boundary, Figure 15. Despite the high heterogeneity, the flow patterns are near-radial at the well and near-linear on the

flowing face. The density of streamlines on the flowing face is due to the variability of flux along the face.

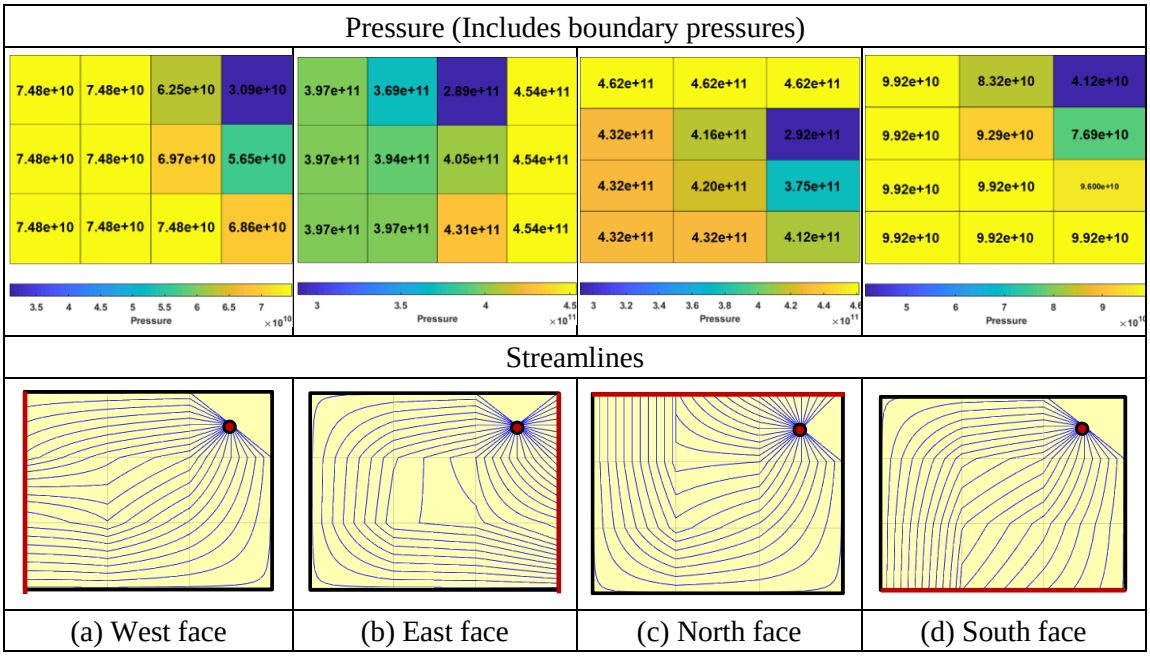

Figure 3-13 Streamline flow visualization of the SSM face transmissibility for the (a) West face, (b) East face, (c) North face, and (d) South face the well block in the highly heterogeneous example. The first row is the pressure map relative to a bottomhole flowing pressure of $p_{wf} = 0$ with a unit value for μq_w. The second row are the streamlines resulting from the velocity field. The red dot represents the location of the well. The red line represents the influx face.

Table 3-2 Upscaled face transmissibility values for each face using the SS and SSM flow patterns, and each well index calculation

WI	Face Transmissibility.	West Face [md*m]	East Face [md*m]	North Face [md*m]	South Face [md*m]
SS	SS	8.486×10^{-8}	6.601×10^{-12}	5.763×10^{-9}	3.453×10^{-12}
	SSM	1.403×10^{-12}	6.296×10^{-12}	6.053×10^{-12}	1.448×10^{-12}
PSS(Q)	SSM	1.222×10^{-12}	-1.805×10^{-12}	-1.826×10^{-12}	-4.458×10^{-12}
PSS(P)	SSM	1.404×10^{-12}	6.319×10^{-12}	6.073×10^{-12}	1.449×10^{-12}

The pressure drop from flowing face to bottomhole is fixed by the SSM calculation, which can be separated into a well index contribution and the remaining face transmissibility. The results for this example are shown in Table 3-2. Of the three examples based on the SSM flow pattern, the SS and PSS(P) calculations are close to identical, due to the near identical values for the well index. However, the PSS(Q) value of the well index is too low, forcing a negative value to arise for the face transmissibility. Clearly, the non-radial distortions in the flow pattern in Figure 3-12 (b), and the non-uniform values of pressure along the boundary of the upscaling region, indicate too high a pressure drop for consistency with Figure 3-13. In contrast, the use of a pressure isobar in the PSS(P) calculation does not develop as high a pressure drop in the well index calculation and gives a result that is essentially identical to the SS well index. In the following numerical examples, we utilize the SS well index with SSM face transmissibility to benchmark our near well upscaling method.

3.6 Analysis of Time of Validity for the Well Index

In the section 3.1, we reviewed the Peaceman's numerical calculation for the well index. The usage for this well index has been reported in Peaceman (1978, 1983), there is a minimum time of validity for the SS flow contact can be applied for the usage of Peaceman equivalent radius, Eq. (1.29), in the fine scale model. The valid time is defined when the dimensionless time larger than one, because the Peaceman equivalent radius is time independent after $t_D = 1$ (Peaceman 1978).

$$t_{valid} = \frac{\phi \mu c_t \Delta x^2}{k} = \frac{\Delta x^2}{\alpha} at\, t_D = 1 \tag{3.4}$$

Here α is the hydraulic diffusivity. However, the time of validity for the well index upscaling and coarse model has not been addressed. How to extend the time of validity to a well index upscaling calculation is crucial for the usage of simulation results in coarse model.

We now redefine the well index, Eq. (1.24), in terms of diffusive time of flight by replacing the ratio r_0/r_w to the ratio τ_p/τ_w.

$$WI^{fine} = \frac{2\pi kh}{\ln\left(\tau_p / \tau_w\right)} \tag{3.5}$$

Here τ_p and τ_w are the DTOF related to Peaceman radius r_0 and well radius r_w, and $kh = \sqrt{k_x k_y}DZ$. The DTOF of Peaceman radius and well radius referring to the diffusivity are defined as:

$$\tau_p = \frac{1}{4} e^{-\gamma} \sqrt{\frac{DX^2}{\alpha_x} + \frac{DY^2}{\alpha_y}} \tag{3.6}$$

$$\tau_w = \frac{r_w}{2}\left(\frac{1}{\sqrt{\alpha_x}} + \frac{1}{\sqrt{\alpha_y}}\right) \tag{3.7}$$

We then redefine the early valid time based on the concept of DTOF, Eq. (3.8). The resulting valid time is also equivalent as the PSS time, t_{PSS}.

$$t_{valid} \approx \frac{1}{2}\left(\frac{DX^2}{\alpha_x} + \frac{DY^2}{\alpha_y}\right) = \frac{1}{2}\left(4\tau_p e^{\gamma}\right)^2 = 25\tau_p^2 = t_{PSS} \tag{3.8}$$

Utilizing the DTOF concept we can also derive the valid time for the coarse well index. First, the coarse DTOF of well radius can be determined by averaging the DTOF with the weights of kh.

$$\tau_w^{coarse} = \frac{\sum_{ijk}\left(kh \cdot \tau_w\right)_{ijk}}{\left(kh\right)^{coarse}},\ \left(kh\right)^{coarse} = \sum_{ijk}\left(kh\right)_{ijk} \tag{3.9}$$

Similar to Eq. (3.5), The coarse well index with respect to the DTOF is defined as:

$$WI^{coarse} = \frac{2\pi\left(kh\right)^{coarse}}{\ln\left(\tau_p^{coarse} / \tau_w^{coarse}\right)} \tag{3.10}$$

By reversing calculation of Eq. (3.10), we can obtain the DTOF of Peaceman radius for coarse well cell, τ_p^{coarse}, and then use it to calculate the PSS time for coarse model.

We now use the derived PSS time to analyze the valid time of simulation results. The first example is a homogeneous 2D model with a single well at the center of the model (Figure 3-14). This model is modified from first layer of SPE10 model with a homogeneous permeability 1 md and porosity 0.1. We enlarged the cell size to allow us to recognize pressure response before $t_D = 1$.

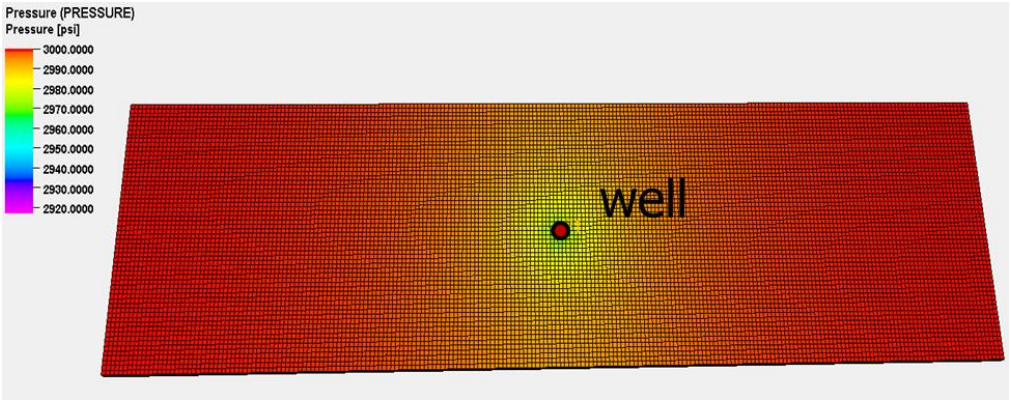

Figure 3-14 Pressure distribution for the homogenous model with a single well at the center of reservoir

The model is coarsened from 60×220 to 6×22, with a coarsening factor of 10×10×1. The constant rate production at 400 STB/day with a pressure constraint at 1000 psi is scheduled for the numerical simulation to the 10^4 day. The total compressibility was 8.9×10-6/psi and the oil viscosity was 1 cp at the initial reservoir pressure. FIELD units are used for this model consistent with the SPE10 literature.

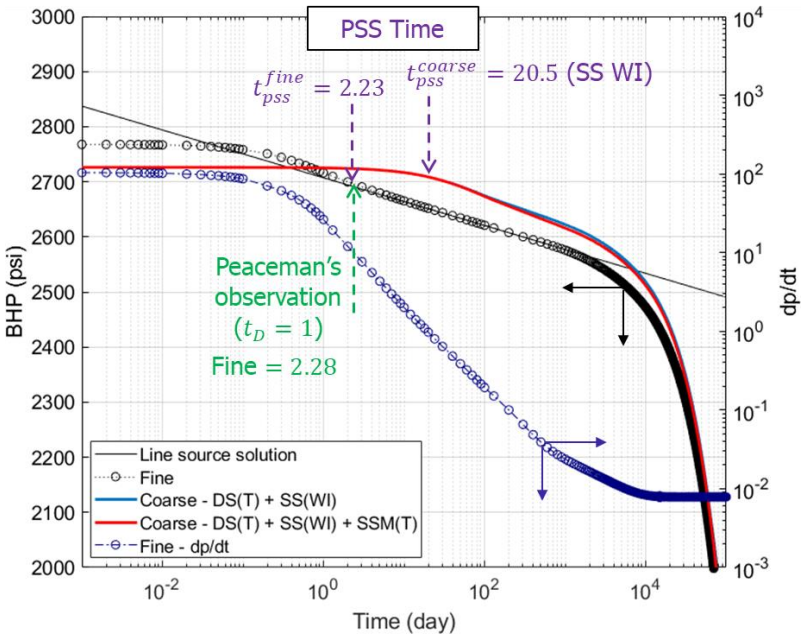

Figure 3-15 Bottom hole pressure (black circle) and pressure derivative (blue circle) profile for the homogeneous model; the black line is the line source solution; the blue line represents the results from the DS (T) + SS (WI) upscaling ; the red line represents the results from the DS (T) +SS (WI) + SSM (T) upscaling.

Figure 3-15 shows the bottom hole pressure and pressure derivative profile for a well in the center of a homogenous reservoir. The black line is the line source solution and the exact calculation which represents the infinite acting radial flow. On the other hand, the black circle is the finite difference calculation, which shows a minimum spatial resolution given by the well cell. The blue circle is the pressure derivative as reference. The blue line represents the results from the DS (T) + SS (WI) upscaling without the face transmissibility. The red line represents the results from the DS (T) +SS (WI) + SSM (T) upscaling. In the homogeneous model, the near well upscaling with or without face transmissibility correction does not impact the upscaling results.

The PSS time for the fine scale and coarse scale model also denoted in the Figure 3-15. The first observation we are making here is that the Peaceman's observation at $t_D = 1$ is essentially at the same 2 decimal point as the PSS time of the Peaceman equivalent radius, t_{PSS}^{fine}. The Peaceman's observation and PSS time both suggest that the finite difference scheme begins to accurate when the pressure profile enter into the steep part of the curve.

Where is the equivalent steep part of the curve for the coarse model is what we try to answer in this analysis. The PSS time for the coarse model, t_{PSS}^{coarse}, can be determined from Eq. (3.10), and the results is denoted in the Figure 3-15. The PSS time for the coarse model also indicated on the steep part of the curve for both the upscaling results.

We have shown the analysis for the homogeneous model (Figure 3-15). Now, we use the top 6 layers from SPE 10 model to analyze the heterogeneous case. Two coarsen ratio are considered for this analysis. The first analysis considers a vertical coarsening. The model is coarsened from 60×220×6 to 60×220×1, with a coarsening factor of 1×1×6. The second analysis considers the horizontal coarsening with 10×10×1 and the model is coarsened from 60×220×6 to 6×22×6. The constant pressure constraint at 1000 psi is scheduled for the heterogeneous case for the numerical simulation to the 10^4 day. The total compressibility and the oil viscosity was followed the homogeneous case as shown before.

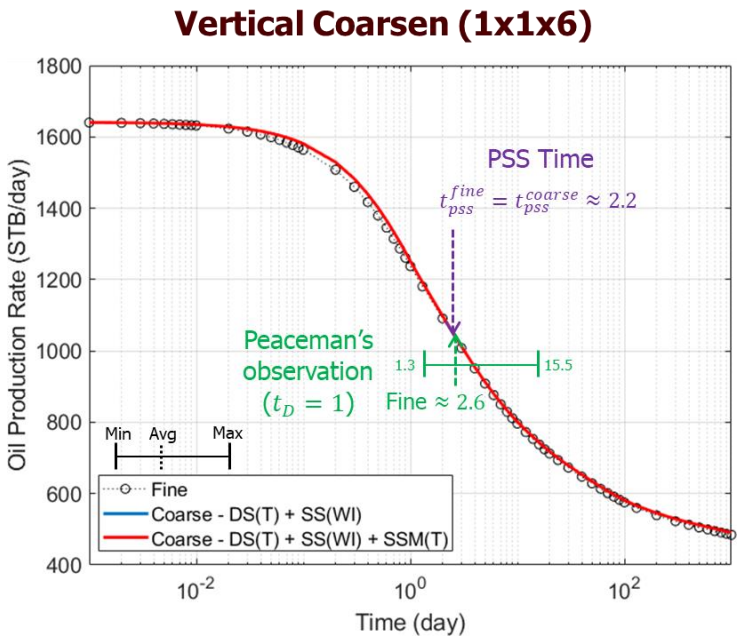

Figure 3-16 Production (black circle) profile for the heterogenous model; the blue line represents the results from the DS (T) + SS (WI) upscaling; the red line represents the results from the DS (T) +SS (WI) + SSM (T) upscaling with 1x1x6 coarsen ratio.

Figure 3-16 represents the production profile for the heterogeneous model and compared with the vertical upscaling results. The black circle represents the production profile for the fine scale model, and the blue and red line overlapped together represent the coarse scale results. Due to the fact that areal resolution does not change, the PSS time for the fine and coarse model are identical. The vertical dash line shows the range of Peaceman's observation and our PSS time for each perforation well cells. The PSS time indicated the same time as Peaceman's observation in the heterogeneous model. Another observation is that the coarse and fine scale are matching together, and no transmissibility correction happen in vertical coarsening.

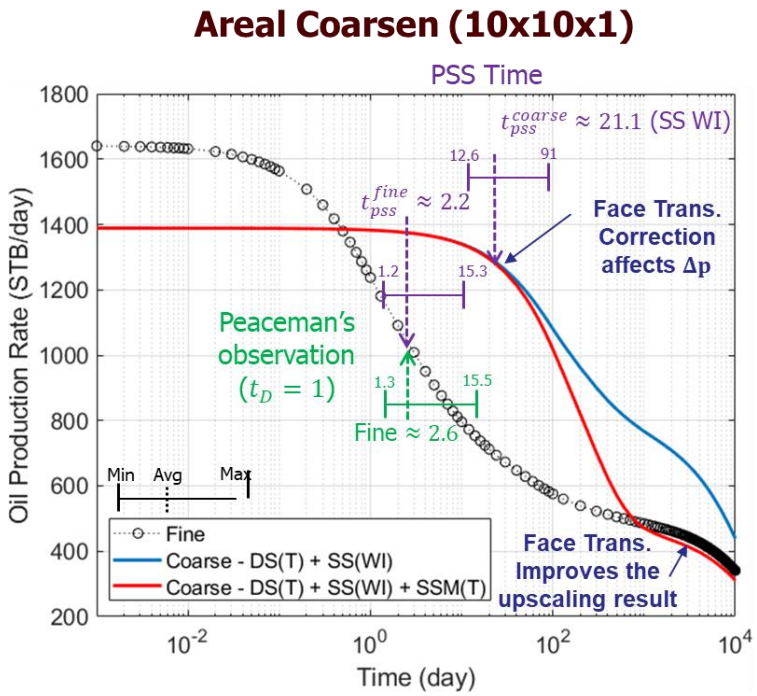

Figure 3-17 Production (black circle) profile for the heterogenous model; the blue line represents the results from the DS (T) + SS (WI) upscaling; the red line represents the results from the DS (T) +SS (WI) + SSM (T) upscaling with 10x10x1 coarsen ratio.

For the results with the areal coarsening, we see similar things in fine scale (Figure 3-17). The vertical dash line shows the range of Peaceman's observation and our PSS time for each perforation well cells in both fine and coarse model, which highlights the usage of the PSS time for the coarse model with multiple peroration well cells. The last observation is that the face transmissibility correction (red line) significantly improve the upscaling results, which is evident again in our previous study again.

3.7 Numerical Experiments

In this section, we utilized three reservoir scale sector models to examine the further novel upscaling workflow which combined the studied for diffuse source/sink distribution and near well upscaling in previous sections. The first two models are the SPE10 Comparative Solution and the Amellago Carbonate outcrop model described before. The third model is the Former Soviet Union shale reservoir model, which will be illustrated later.

3.7.1 SPE 10 Model

The reference calculation consists of a standard five-spot pattern with one injector located at the center of the grid blocks at (i, j) coordinates of (30, 110), and four producers at the outside corners of the four corner grid blocks, as shown in Figure 1-11. The model is coarsened from 60×220×85 to 6×22×85, with a coarsening factor of 10×10×1. This upscaling ratio is similar to those previously utilized in the literature (Nunna and King 2020, Wen et al. 2006). Steady state flow simulation is performed by fixing the producers and the injector with a bottomhole pressure constraint at 1000 psi and 4000 psi, respectively. As the well pressures are defined, the accuracy of the near-well upscaling techniques is measured by observing the total well liquid flow rates in comparison with the fine and coarse systems.

We compared the results of the flow-based upscaling methods and also include algebraic well index upscaling approaches that may be used when the well trajectory and the geological model are not simultaneously available, as is common in many projects.

These algorithms have been described in more detail previously (Liu et al. 2019), but now they are extended to include the new near well upscaling calculations of the current study. They include algorithms that are available in commercial flow simulators and geologic models, and also our research algorithms. We briefly describe the combinations of transmissibility and well index upscaling used for comparison purposes.

1. AHCSS (T) + PVWI (WI): Analytical half-cell steady state transmissibility upscaling with pore volume weighted well index upscaling. This combination is in use in a well-known commercial flow simulator.
2. AHCSS (T) + AWI (WI): Analytical half-cell steady state transmissibility upscaling with analytical well productivity upscaling. The analytic well productivity upscaling was developed for use in upscaling the cell permeability of the geologic model for flow simulation (King 2007, King et al. 1998).
3. DS (T) + AWI (WI): Diffuse Source transmissibility upscaling (DS) with analytical well productivity upscaling
4. DS (T) + SS (WI): Diffuse Source transmissibility upscaling (DS) with steady state flow based well index upscaling.
5. DS (T) + PSS(P) (WI): Diffuse Source transmissibility upscaling (DS) with diffuse source well index upscaling (PSSP).
6. DS (T) + SS (WI+T): Diffuse Source transmissibility upscaling (DS) with steady state flow based well index and face transmissibility upscaling.
7. DS (T) + SSM (WI+T): Diffuse Source transmissibility upscaling (DS) with SSM face transmissibility and well index upscaling.

8. DS (T) + SS (WI) + SSM (T): Diffuse Source transmissibility upscaling (DS) with steady state flow based well index upscaling and SSM face transmissibility.
9. DS (T) + PSS(P) (WI) + PSSPM (T): Diffuse Source transmissibility upscaling (DS) with pseudo steady state diffuse source well index upscaling and SSM face transmissibility.

To compare the different methods, we utilize a normalized L2 error norm, based on the sum of the difference of each well's rate compared to the fine scale reference calculation. The total well flow rate and the L2-Norm errors for different methods are presented in Figure 3-18. Results of the fine scale reference calculation are indicated as a vertical black line to help comparison with the other approaches.

From bottom to top, we first show the results of the AHCSS (T) + PVWI (WI), AHCSS (T) + AWI (WI), and DS (T) + AWI (WI) methods. Around these three methods, DS flow-based transmissibility upscaling shows the advantage between flow-based transmissibility upscaling and analytical transmissibility upscaling. Besides, these are both methods where the well trajectory and the geological model are not simultaneously available. These three methods have the advantage of being applicable to all project workflows and may be implemented quite easily. However, the flow-based upscaling approaches that utilize the well trajectories are more accurate, as shown on the following two cases show the results of the DS (T) + SS (WI) and DS (T) + PSSP (WI) methods.

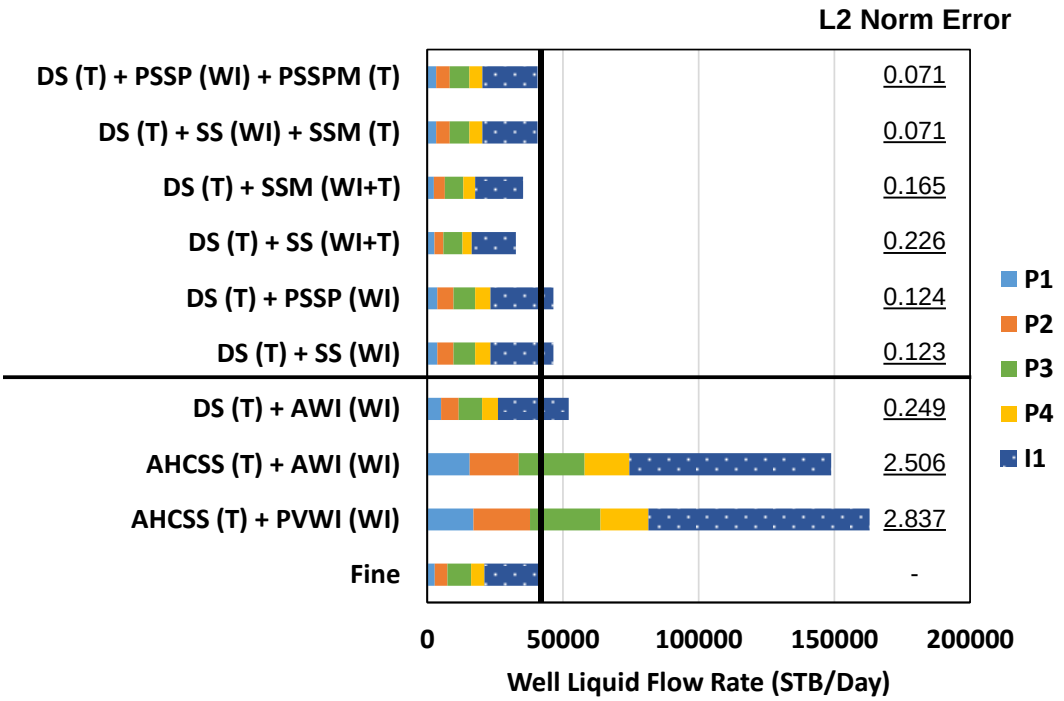

Figure 3-18 Well liquid flow rate with the L2-Norm error for each upscaling approach

The remaining four cases shown in Figure 3-18 all provide extremely good results except DS (T) + SS (WI+T) method because the SS face transmissibility correction does not provide a localized pressure solution. All of these cases include the face transmissibility corrections and two of them utilize explicit upscaling of the well index. As in the smaller models previously examined, the SS and PSSP well index upscaling approaches give essentially identical results. The inclusion of the face transmissibility upscaling provides additional improvement. Overall, the combination of DS (T) + SS (WI) + SSM (T) upscaling provides the most accurate upscaling approach for this SPE10 example.

3.7.2 Amellago Carbonate outcrop model

The Amellago model is coarsened to three coarse grid resolutions with a vertical coarsening ratio 6 (i.e., 1x1x6, 2x2x6, and 3x3x6). The numerical example is simulated under steady state flow conditions subject to bottomhole flowing pressure constraints. We, therefore, utilize the total well liquid flow rates in order to quantify the error between the fine and coarse systems with each upscaling technique. Before we move to the results of the simulation, we summarize the upscaling approaches studied. The list includes those of a previous study reported from Liu et al. (2019), as listed in Table 3-3, and augmented with the current near-well upscaling approaches. This list is not identical to the algorithms used for the SPE10 case.

Table 3-3 Summary of upscaling cases (After Liu et al. (2019))

		Transmissibility Upscaling					Transmissibility Upscaling With Near-Well Correction
		AHCSS	HCSS	K	SS	DS	DS + SSM
Well Index Upscaling	PVWI	1					
	AWI		3				
	K			4			
	SS				5		7
	PSSP	2				6	

The transmissibility upscaling used in this analysis includes:

1. AHCSS (T): Analytical half-cell steady state transmissibility upscaling, Eq. (1.11)
2. HCSS (T): Half-cell steady state transmissibility upscaling, Eq. (1.12) with the pressure drop between the center of the coarse cell
3. K (T): Flow based cell permeability upscaling, Eq. (1.12)

4. SS (T): Flow based steady state transmissibility upscaling, Eq. (1.13)
5. DS (T): Diffuse Source transmissibility upscaling, Eq. (1.14)

The well index upscaling used in this analysis includes:

1. PVWI (WI): Pore volume weighted well index upscaling, Eq. (1.18) with the pore volume weighted properties
2. AWI (WI): Analytical well productivity index, Eq. (1.28)
3. K (WI): Analytic Peaceman well index based on the flow based cell permeability upscaling, Eq. (1.18)
4. SS (WI): Steady state flow based well index upscaling, Figure 3-2 (a)
5. PSS(P) (WI): PSS(P) well index upscaling, Figure 3-2 (c)

The near well index upscaling with the face transmissibility correction (SSM) utilized Eq. (3.3) to calculate the half cell transmissibility and combined with the DS transmissibility upscaling.

A summary of the well flow rates for different coarsening resolutions and upscaling methods are presented in Figure 3-19. Table 3-4 displays the L2-Norm error for these upscaling methods at each resolution, and the average of the L2-Norm error summarizes the total mismatch with the fine scale system for each method.

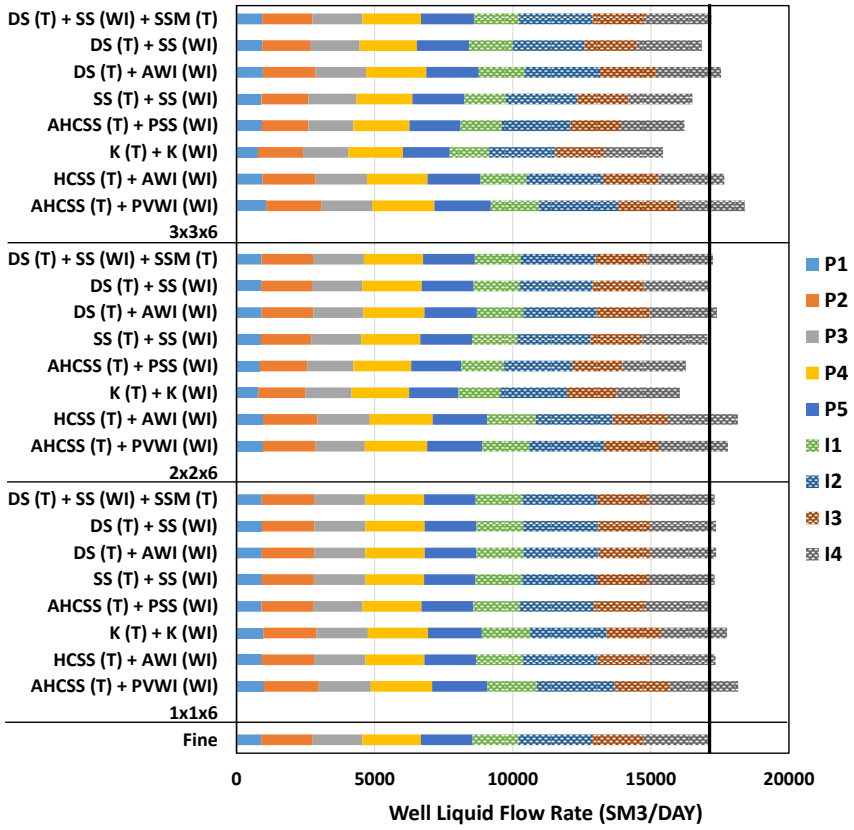

Figure 3-19 Well liquid flow rates for different coarsening ratios and upscaling approaches

Table 3-4 L2-Norm error of the well liquid flow rates for each upscaling approach and coarsening ratio

T WI Face T	AHCSS PVWI ---	HCSS AWI ---	K K ---	AHCSS PSSP ---	SS SS ---	DS PSSP ---	DS SS SSM
1x1x6	0.062	0.017	0.039	0.003	0.016	0.019	0.015
2x2x6	0.047	0.062	0.066	0.052	0.010	0.011	0.011
3x3x6	0.081	0.038	0.098	0.061	0.045	0.028	0.016
Average	0.063	0.039	0.068	0.039	0.024	0.019	0.014

As the coarsening ratio increased, upscaling based on algebraic calculations of the transmissibility or the well index, i.e., AHCSS, PVWI, and AWI, consistently

yielded poorer results compared to the flow-based calculations. Of the flow-based calculation, the cell pair intercell transmissibility upscaling performs consistently better than single cell permeability upscaling (i.e., K). Both DS and SS transmissibility upscaling work equally well, even though DS has slightly lower computed error than SS. Other studies, however, have shown that steady state-based upscaling can result in strong crossflows and negative transmissibilities, which are both problematic for two-point flux calculations, as described in Liu et al. (2019).

Generally, the methods that have the least accurate well index upscaling show the poorest performance, e.g., the pore volume weighted average (PVWI) and the cell permeability well index calculation (K). The PVWI calculation is a purely heuristic method that uses a pore volume weighted average of the fine scale permeability and cell dimensions together with Peaceman's well index relationship. By replacing the pore volume weighted average approach with the flow based well index upscaling, as denoted by AHCSS (T) + PSSP (WI), the improvement can be observed for 1x1x6 coarsening in particular where exact results are known. The cell permeability well index calculation also utilizes Peaceman's well index. However, although the permeability is flow based, the flow pattern uses linear flow core-flood boundary conditions, which does not capture the radial flow and pressure gradients near a well perforation.

Comparing the calculations summarized in Figure 3-19 and Table 3-4 allows us to draw additional conclusions. Of the transmissibility calculations, DS performs consistently well. This is especially apparent as the size of the upscaling region is increased and the impact of local heterogeneity becomes more important. Of the well

index calculations, those based on radial flow (SS and PSSP) perform well compared to the analytic or linear flow-based calculations.

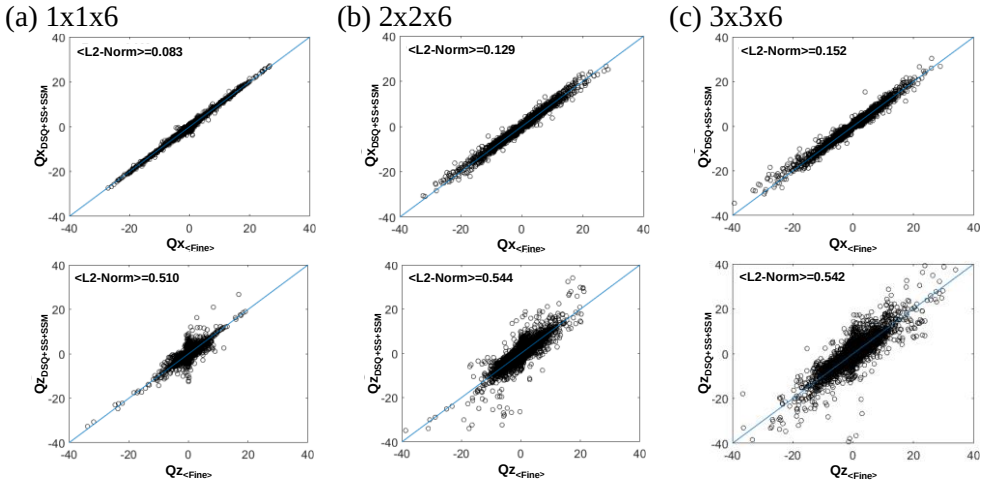

Figure 3-20 DS+SS+SSM upscaling comparison of coarse and summed fine scale face fluxes in the x direction (first row) and z direction (second row) at 1 month for (a) 1x1x6, (b) 2x2x6, and (c) 3x3x6 coarsening ratios. The L2-Norm error is provided to summarize the total error.

To understand the additional improvement provided by the correction to the well cell face transmissibility we have examined the flux within the reservoir model in detail. Figure 3-20 shows the results with the additional correction for the well cell face transmissibility. This removes the systematic errors seen in Figure 3-5 and reduces the L2-Norm error. The vertical flow correlation is only marginally improved, as expected since the well is fully completed in the vertical direction.

3.7.3 Former Soviet Union shale reservoir model

In this numerical experiment, we applied the novel distance-based upgridding statistical upgridding algorithms (VxS method) to design the vertical coarsen scheme.

The upgridding algorithm has been reported in the paper by Syed et al. (2020). We considered the statistical upgridding algorithms (i.e., velocity, slowness, and combining velocity and slowness (VS)), distance-based upgridding method, and uniform upgridding for reference purposes. We considered three coarsen ratios for the areal coarsening (i.e., 1x1, 3x3, and 5x5). We utilized the most accurate upscaling method that we have validated in the previous two numerical experiments (i.e., DS (T) + SS (WI) + SSM (T) method) for the upscaling algorithm. Figure 3-21 shows the well flow rate for each well and sums up the total flow rate with the L2 Norm Error listed.

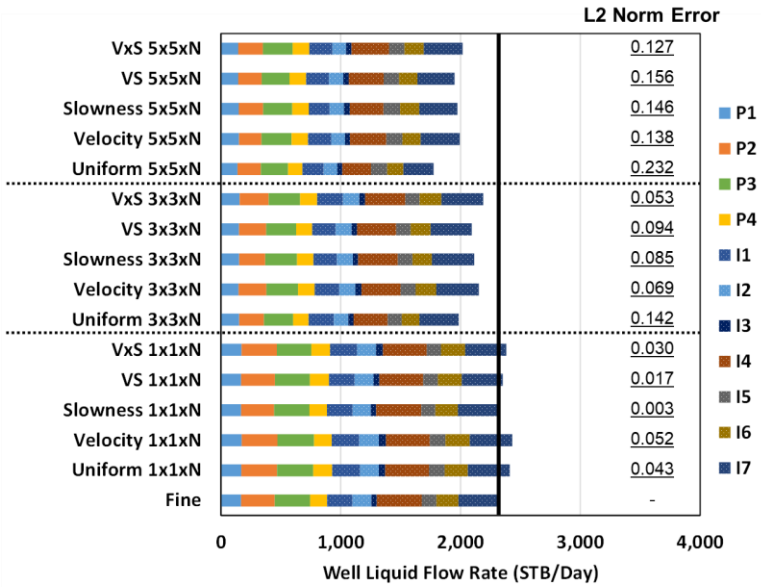

Figure 3-21 SFU model well flow rates for the upscaled simulation models

The black vertical line represents the fine scale result as a reference for upscaling results. First, the uniform upgridding comparing with the other upgridding results showing the benefits of utilizing the sophisticated upgridding design. Although we observe the slowness statistical upgridding has a better result in 1x1 areal coarsen

schemes, in the higher areal coarsen ratio (i.e. 3x3 and 5x5), the accuracy of the slowness statistical upgridding decreased. The distance-based upgridding, on the other hand, has the minor L2 Norm error when the areal coarsen ratio increases.

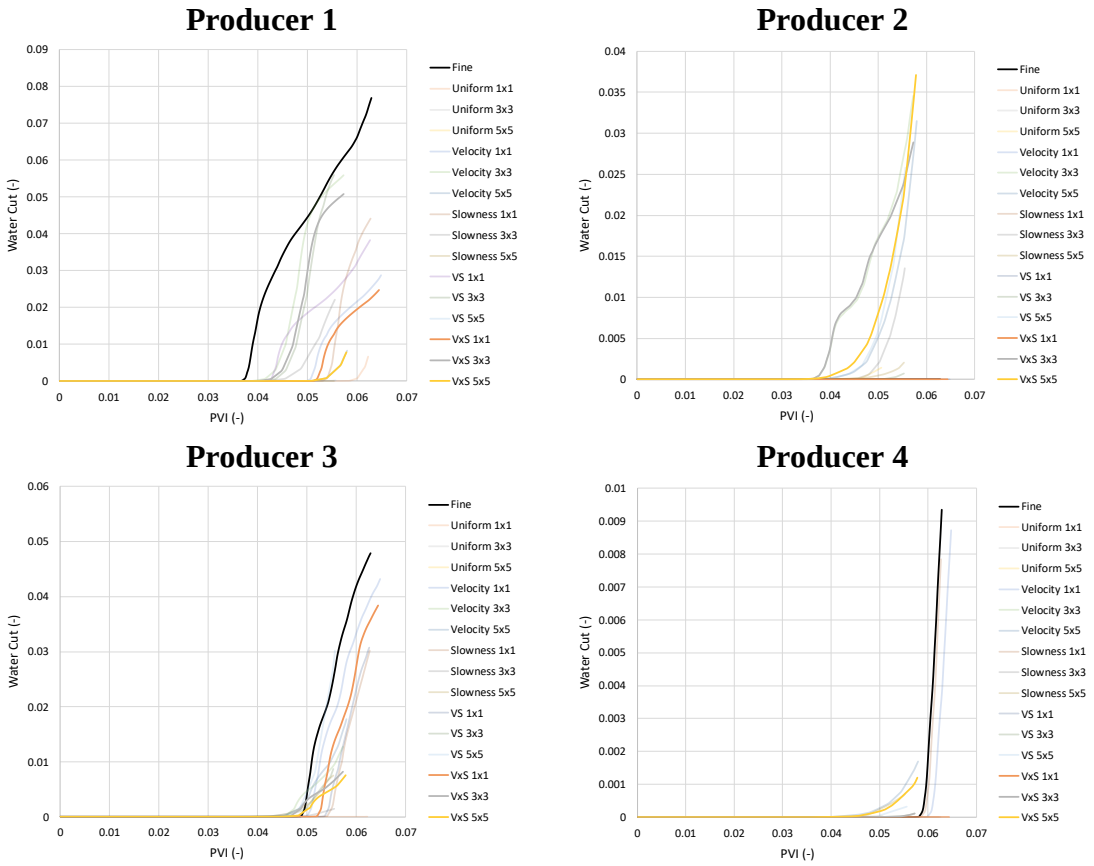

Figure 3-22 Water cut versus dimensionless time in pore volumes (PVI) for each producer (all schemes)

Table 3-5 PVI L2 Norm error for the upgridding scheme

PVI Error					
	Uniform	Velocity	Slowness	VS	VxS
1x1xN	0.0330	0.0040	0.0055	0.0175	0.0194
3x3xN	0.0368	0.0262	0.0304	0.0167	0.0263
5x5xN	0.0492	0.0170	0.0382	0.0362	0.0154
Average	0.0397	0.0157	0.0247	0.0234	0.0204

The water cuts profile versus pore volume injection for the four producers are shown in Figure 3-22. The fine scale reference result is plotted as a black line and the three VxS calculations are highlighted as bold lines. All other simulation calculations have been shaded. Table 3-5 shows that the VxS with DS upscaling consistently performs well compared to the other methods.

As a sensitivity on the upscaling methodology, we have considered three different flow calculations. The first is the DS (T) + SS (WI) + SSM (T) upscaling calculation, as shown in Figure 3-8. The second is a modification to the vertical transmissibility to use a PSS calculation. This method reduces the vertical transmissibility compared to DS upscaling whenever low permeability is present. Finally, we also consider the use of the industry standard upscaling (i.e. ECLIPSE COARSEN) with no use of the current upscaling methodology.

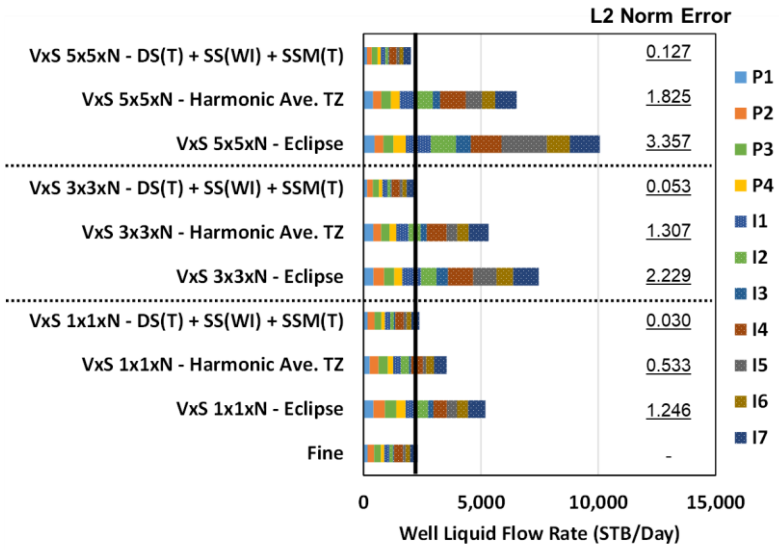

Figure 3-23 FSU well flow rate for upscaling sensitivities

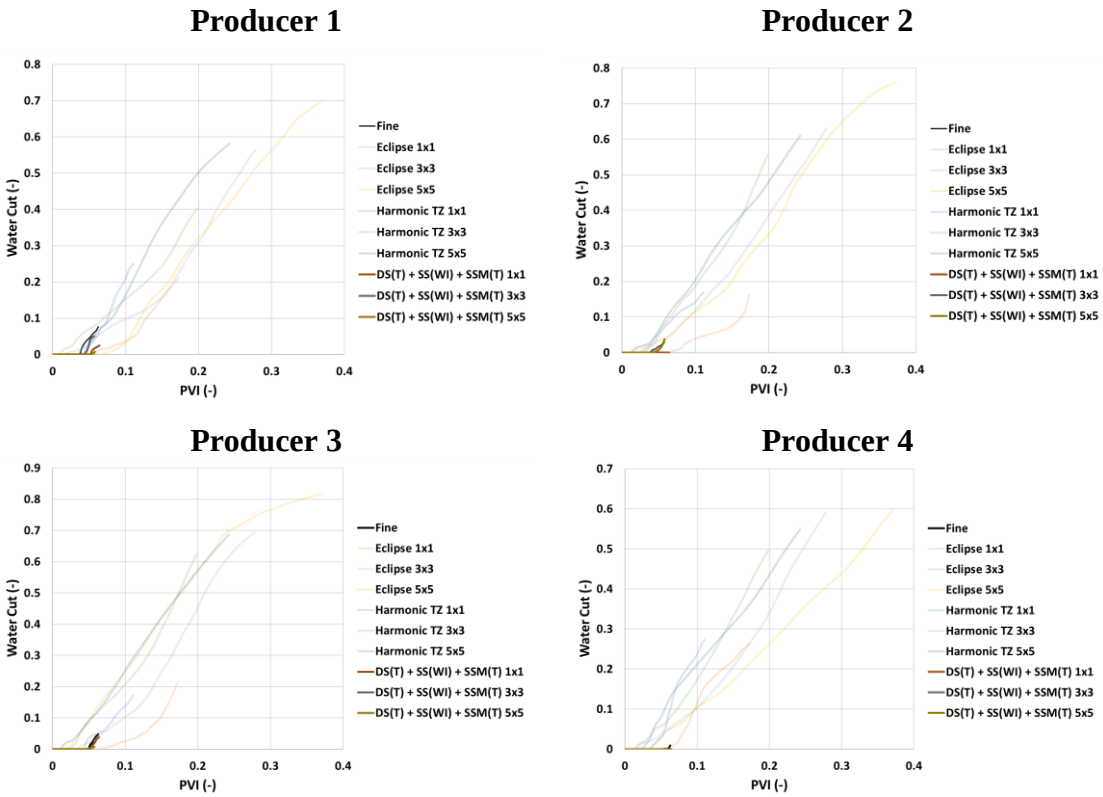

Figure 3-24 FSU water cut versus dimensionless time in pore volumes (PVI) for upscaling sensitivities

Table 3-6 PVI L2 Norm error for the upscaling method

	PVI Error		
	Eclipse	Harmonic TZ	DS(T) + SS(WI) + SSM(T)
1x1xN	0.0260	0.0137	0.0194
3x3xN	0.0319	0.0329	0.0263
5x5xN	0.0272	0.0226	0.0154
Average	0.0284	0.0231	0.0204

The well flow rate comparisons are shown in Figure 3-23 and water cut comparisons are shown in Figure 3-24. In each case the distanced-based upgridding algorithm was applied. These results are even more striking than the previous comparisons, showing the importance of choosing the better upscaling algorithm to best represent flow, especially in the vertical direction. The PVI L2 Norm error for each upscaling algorithm are listed in Table 3-6 which validated again that DS (T) + SS (WI) + SSM (T) upscaling calculation has smallest averaging error as what we observed in the Figure 3-24.

3.7 Discussion

Although much of the upscaling literature has focused on the upscaling of permeability and/or the intercell transmissibility, an important subset has considered near well. Our results reinforce and are consistent with many of their conclusions on the importance and benefits of near well upscaling. However, to best take advantage of these techniques requires a change in the geologic modeling to flow simulation workflow, which is already underway. If we only provide upscaled models to the flow simulator then none of these techniques are directly applicable as the well trajectory and the

geologic model are not simultaneously available. Most commercial flow simulators provide the capability of coarsening a model at run time, in which suitably averaged or summed pore volume, permeability and intercell transmissibility are calculated. Inclusion of a more accurate well index upscaling is certainly conceivable. This also provides the practicing engineer with more options as it allows resolution and simulation cost to be selected on the immediate requirements, from screening calculations with an ensemble of coarse (and uncertain) models to full field simulation and the evaluation of field development options to detailed mechanistic calculations at high resolution, perhaps in local sector models.

Although our conclusions are consistent with earlier studies, the specific methods we have developed have one important advantage. All of our recent developments have utilized the concept of superposition to provide completely local upscaling calculations. We have also recognized that flow simulation is a sequence of transient calculations, which may or may not reach PSS locally during a simulation time step. For the intercell transmissibility this has led to the development of diffuse source upscaling, which approaches the PSS limit but only on a well-connected sub-volume. For flow with wells, we instead have a point source, not a diffuse source, and the long-time limit of flow is locally steady state, not PSS. The resulting flow calibration is uniquely provided by the SSM boundary conditions, in which arbitrary flow into a well cell may be represented as a superposition of SSM calculations. Expressed as a half-cell transmissibility, this result may be combined with the previously calculated half-cell transmissibility that was

implicit in the DS intercell transmissibility, showing that only well cell and well cell face properties need to be modified for well perforations.

This analysis places more emphasis on flow from perforation to cell face than it does for flow from perforation to well cell, i.e., the well index. The SSM pressure drop is separated into two: perforation to cell and cell to face. So long as the modelled perforation to cell pressure drop does not exceed the SSM pressure drop then we can consistently define a well index (perforation to cell flow) and a half-cell face transmissibility (cell to cell face flow). SS upscaling provides such a consistent well index reference calculation as it is equivalent to a superposition of SSM calculations. As a summary, we obtain the combination of upscaling calculations shown in Figure 3-8.

3.8 Chapter Summary and Conclusions

The novel near well upscaling workflow has been developed and improved understanding of the near well flow behavior. We have introduced a completely local and completely general well cell upscaling technique based on the concept of superposition. The key element of our approach is the use of a complete set of local flux basis functions that ensure that the local calculations can be used to represent an arbitrary global flow field. Implementation of the solution requires a calculation for the well index and a modification to the half cell face transmissibility, but only in the perforated well cells. No other changes are needed in the near well region or in the remainder of the model. The results may be readily combined with the previously

developed diffuse source intercell transmissibility upscaling to obtain the intercell transmissibility from the well cell to adjacent cells.

The methods have been tested by comparison of the well rates for single-phase near steady state flow for five cases generated from two reservoir sector models (SPE10 and the Amellago carbonate outcrop) and results compared to previous research and commercially available upscaling techniques. All the examples (including both vertical and horizontal wells) showed improvement in their upscaling results by the combination of the near well upscaling for the well index (SS), half cell transmissibility (SSM), and intercell transmissibility (DS).

The current calculation for the well index may be considered a generalization of Peaceman's well index, but now extended to represent near well reservoir heterogeneity and with an arbitrary placement of a well perforation within a simulation well cell. However, Peaceman's analysis does not include the equivalent of the SSM cell face transmissibility, and this is important to correctly couple the well cell to the adjacent reservoir model. As with Peaceman, we have shown that the SS and PSS isobar well cell upscaling calculations give essentially identical results. We have also shown that the flow based calculations are consistently more accurate than performing a static upscaling calculation and the use of Peaceman's well index on a coarse grid.

We demonstrate that Peaceman's early time of validity for the Well Index in a homogeneous model is equal to the PSS time at the Peaceman radius in the perforated cells. Utilizing the PSS time allows us to extend Peaceman's time of validity to multiple perforations, heterogeneous models and upscaled models. We demonstrate the accuracy

for SPE 10 in both vertical and areal upscaling. The PSS time predicts the minimum time of validity for the finite difference transient solution, as demonstrated for both constant pressure and constant rate solutions with multiple perforation wells

CHAPTER IV

FINITE DIFFERENCE FLOW DIAGNOSTICS METHOD[‡]

This chapter starts with generalizing the compressible flow diagnostic and depletion Lorenz plot for the unconventional reservoir. Next, the results of a simple waterflooding model, a primary depletion model, and a hydraulically fractured well in the natural fractured reservoir model are presented to demonstrate the compressible flow diagnostic approach. The depletion Lorenz coefficient is applied for the primary depletion and unconventional reservoir models. We then presented a multiple transversely fractured well modeled in a commercial reservoir simulator. We will use this model as a benchmark against the diagnostic combined with compressible flow diagnostic (CTOF) and FMM methods (DTOF). Finally, the differences between the propagation of pressure and fluid particle fronts are used to address when occurs the fracture or well interference, how much of the pore volume is produced, and what strategies could be used to increase the drainage volume and thus maximize recovery factors from unconventional reservoirs.

[‡] Part of this section is reproduced with the permission from Nunna, K., Liu, C.H., and King, M.J. 2019. Application of Diffuse Source Functions for Improved Flow Upscaling. Computational Geosciences. DOI: 10.1007/s10596-019-09868-x.

[‡] Part of this section is reproduced with the permission from Nandlal, Kiran, Li, Chen, Liu, Ching-Hsien, Chavali, Venkata Bala Krishnateja, King, Michael J., and Ruud Weijermars. "Understanding Field Performance of Hydraulically Fractured Wells: Comparison of Pressure Front versus Tracer Front Propagation Using the Fast Marching Method (FMM) and Complex Analysis Method (CAM)." Paper presented at the SPE/AAPG/SEG Unconventional Resources Technology Conference, Virtual, July 2020. DOI: 10.15530/urtec-2020-2474.

4.1 Generalized Compressible Flow Diagnostic

The finite difference compressible flow diagnostic extended the control volume derivation by Shahvali et al. (2012) to compressible Nunna et al. (2019). One of the valuable tools in flow diagnostic is the drainage volume partition. The drainage volume partitions can be identified using the stationary tracer equation.

$$\vec{u} \cdot \nabla c_i = 0 \tag{4.1}$$

Here c_i is the concentration of the tracer from index *i*, and *i* is either a well, a perforation, or a source point. For instance, the tracer can start from an injector or any cell with the fluid expansions to a producer (Figure 4-1).

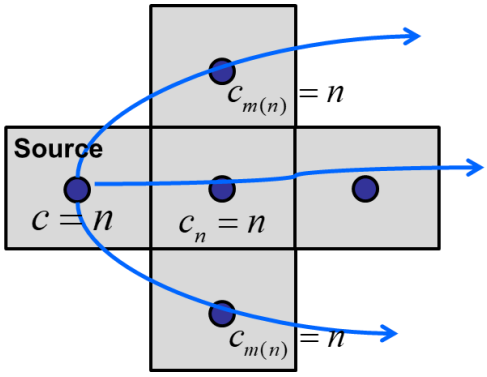

Figure 4-1 Schematic shows the concentration value start from a well cell

The finite difference equation is based on a single face with maximum flux to assign the concentration value for the cell. We tag the source of the maximum flux value and assign the partition based on it.

$$c_n - c_{m(n)} = 0 \tag{4.2}$$

The drainage volume partition distinguished the flow region for each well or source. The convective time of flight was then computed based on each flow region with the specific well or source.

The convective time of flight (CTOF denoted as τ^c) represents the propagation of fluid particle was solved by the time-of-flight equation.

$$\vec{u} \cdot \nabla \tau^c = \phi \tag{4.3}$$

Here $\vec{u}$ is the interstitial velocity, τ^c is the CTOF required for a neutral particle (tracer) to arrive at a particular location, and ϕ is the porosity. Noted that the CTOF represents the tracer front propagation, which is different with the diffusive time of flight (DTOF denoted as τ) representing the impulse of pressure propagation. Eq. (4.3) can be written in a more general conservation form applicable for either incompressible or compressible flow using the chain rule as follows.

$$\nabla \cdot \left(\tau^c \vec{u} \right) - \tau^c \left(\nabla \cdot \vec{u} \right) = \phi \tag{4.4}$$

For the compressible flow, the divergence of the velocity term ($\nabla \cdot \vec{u}$) is non-zero. The advantage here is that we do not need an injector to calculate the drainage volume partitions. This could be beneficial in the early life of the field undergoing primary depletion and not restricted for the waterflood model because the field rarely reaches the ratio of volume replacement equals to one, not to mention for the gas reservoir or unconventional reservoir. We extended the control volume derivation of Shahvali et al. (2012) to compressible flow by integrating Eq. (4.4) over a cell volume Ω_n, we have

$$\int_{\Omega_n} d^3x \left[\nabla \cdot \left(\tau^c \vec{u} \right) - \tau^c \left(\nabla \cdot \vec{u} \right) \right] = \int_{\Omega_n} d^3x \phi \tag{4.5}$$

Using divergence theorem for the integral in Eq. (4.5), we have Eq. (4.6) where $\hat{n}$ is the unit normal vector pointing outwardly over Ω_n.

$$\oint_{\partial\Omega_n} d^2x\left[\hat{n}\cdot\left(\tau^c\vec{u}\right)\right]-\tau_n^c\oint_{\partial\Omega_n} d^2x\left[\hat{n}\cdot\vec{u}\right]=V_{p,n} \tag{4.6}$$

Here τ_n is given by a cell property, and $V_{p,n}$ is the pore volume of Ω_n. Now, we consider the first term in the integral of Eq. (4.6), which can be written as time of flight weighted sum of face fluxes for a cell, Eq. (4.7).

$$\oint_{\partial\Omega_n} d^2x\left[\hat{n}\cdot\left(\tau^c\vec{u}\right)\right]=\sum_{m(n)} q_{nm}\tau^c_{nm,\,face}\approx\sum_{m(n)} q_{nm}\tau^c_{nm} \tag{4.7}$$

The CTOF is approximated from the upstream value, as Shahvali et al. (2012) discussed. Eq. (4.7) can be further simplified by separating the upstream (denoted by subscript *m*) and downstream (denoted by subscript n) faces of the cell based on the face fluxes, Eq. (4.8).

$$\oint_{\partial\Omega_n} d^2x\left[\hat{n}\cdot\left(\tau^c\vec{u}\right)\right]=\tau_n^c\sum_{m(n)}^{q_{nm}>0} q_{nm}+\sum_{m(n)}^{q_{nm}<0} q_{nm}\tau_m^c \tag{4.8}$$

Here τ_m is the time-of-flight of the cell upstream to the current cell face and τ_n is the time-of-flight of the current cell. Next, we rewrite the second term in the integral of Eq. (4.6) as cell time-of-flight times the sum of face fluxes for the cell. Again, we separate the upstream and downstream faces.

$$\tau_n\oint_{\partial\Omega_n} d^2x\left[\hat{n}\cdot\vec{u}\right]=\tau_n\sum_{m(n)} q_{nm}=\tau_n\left(\sum_{m(n)}^{q_{nm}>0} q_{nm}+\sum_{m(n)}^{q_{nm}<0} q_{nm}\right) \tag{4.9}$$

Substituting Eq. (4.8) and Eq. (4.9) in Eq. (4.6), we have the final time of flight equation for a cell after algebraic manipulation.

$$\tau_n\left(-\sum_{m(n)}^{q_{nm}<0} q_{nm}\right)+\sum_{m(n)}^{q_{nm}<0} q_{nm}\tau_m = V_{p,n} \tag{4.10}$$

Eq. (4.10) generates a sparse system for the compressible flow, which can be handled efficiently by any sparse matrix solver libraries. We can take advantage of the flux field generated from the transient or pseudo steady state flow to perform compressible flow diagnostics without assuming a steady state flow.

4.2 Depletion Lorenz Plot

As discussed in Chapter 1.5, the dynamic Lorenz plot is defined as the storage capacity (based on the pore volume) versus the flow capacity (based on the total CTOF, which is the summation of CTOF from producers and injectors) (Shahvali et al. 2012, Møyner et al. 2015a). However, for the unconventional reservoir or primary depletion reservoir, the CTOF from injectors does not exist. If we still calculated the dynamic Lorenz plot based on the CTOF from producers and the CTOF tracing from the reservoir boundary instead of CTOF from injectors would result in a distorted curve due to the infinite CTOF from producers (the blue curve shown in Figure 4-2).

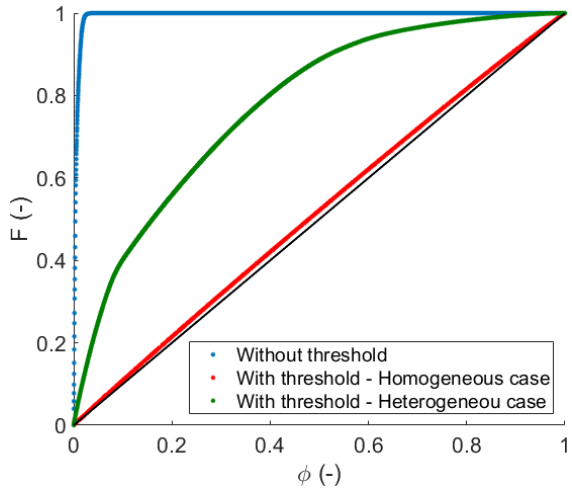

Figure 4-2 Dynamic Lorenz plot. The F on the y-axis is the flow capacity. The Φ on the x-axis is the storage capacity. The blue curve presents the distorted Lorenz curve without the threshold. The green and red curves present the depletion Lorenz curve with the threshold in heterogeneous and homogeneous flow regions, respectively. The black diagonal line represents the identical displacement.

Therefore, this study modified the dynamic Lorenz plot by defining a diagnostic region, which thresholds the volume within 50% of flux adding to the production in the whole drainage volume, to avoid the infinite time of flight issue. The flux adding to the producer reaches 100% at the wellbore and gradually decreases to zero at the boundary of the well drainage volume. Hence, the 50% flux represented the region, which has a substantially large pressure drop. The CTOF from injectors can then be replaced by the CTOF from sources flow into the diagnostic flow region. This approach first computes the volumetric rate, *f*, and pore volume, V_p, of cell k associated with the producer *i*.

$$f_k^i = \frac{c_k^i V_{p,k}}{\tau_k}, \quad V_{p,k}^i = c_k^i V_{p,k} \tag{4.11}$$

Here c_k^i is the producer *i* concentration and τ_k is the summation of time of flight from producer and sources. The volumetric rate and pore volume are then sorted in ascending order based on the total time of flight. Consequently, the flow capacity and storage capacity for a producer i are determined by the cumulative sum of the volumetric rate with normalization of the total sum.

$$F^m = \frac{\sum_{k=1}^{m} f_k^i}{\sum_{k=1}^{N} f_k^i}, \quad \Phi^m = \frac{\sum_{k=1}^{m} V_{p,k}^i}{\sum_{k=1}^{N} V_{p,k}^i} \tag{4.12}$$

Where for $m = \{1,...,n\}$. Here, index *n* is the total number of cells associated with producer *i*, and *N* is the total number of cells in the model. The resulting depletion Lorenz plot resolved the issue of infinite CTOF, as shown on the green and red curves in Figure 4-2 for the heterogeneous and homogeneous flow regions, respectively. Besides, the Lorenz coefficient was defined as twice the area under the Lorenz curve and above the diagonal line in the Lorenz plot (as shown on the area between the blue and black line in Figure 4-2).

$$L_c = 2\left(\int_0^1 F d\Phi - 0.5\right) \tag{4.13}$$

The quantity of Lorenz coefficient is between 0 as an identical displacement observing in a homogeneous reservoir and 1 representing the extremely heterogeneous reservoir.

4.3 Application of Compressible Flow Diagnostic

The following section will demonstrate what information we can get by utilizing the compressible flow diagnostics to three different reservoir models (waterflooding model, primary depletion model, and multi-hydraulic horizontal well model with natural fractures) based on a 2D-PEBI grid.

4.3.1 Analysis of Water Flooding Model

The first numerical example is a water flooding model built on the PEBI grid. The model has 1 injector at the center and 4 producers at the corner with the pressure constraint at 1000 psi and 4000 psi, respectively. The single-phase simulation with slightly rock and fluid compressibility has been performed for 50 years of production. The total compressibility was 5×10-6/psi and the oil viscosity was 1 cp at the initial reservoir pressure. Although it is not actually in the field production, this well schedule allows us to test the model in the SS condition. The permeability and pressure distribution are shown in Figure 4-3.

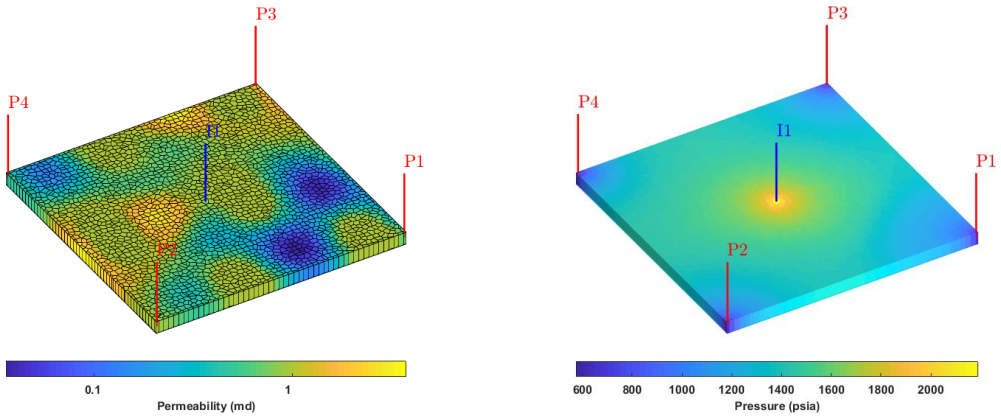

(a) Permeability distribution (b) Pressure distribution

Figure 4-3 Permeability and pressure distribution for water-flooding model

The permeability distribution is created based on the Gaussian random field. Figure 4-4 shows the well drainage partition map and well partition pie chart. The tracer concentration from producers could capture the drainage volume pattern for each well pair and summarized as the drainage partition, which quantified the production capacity for each producer and helped us to rank the well potential.

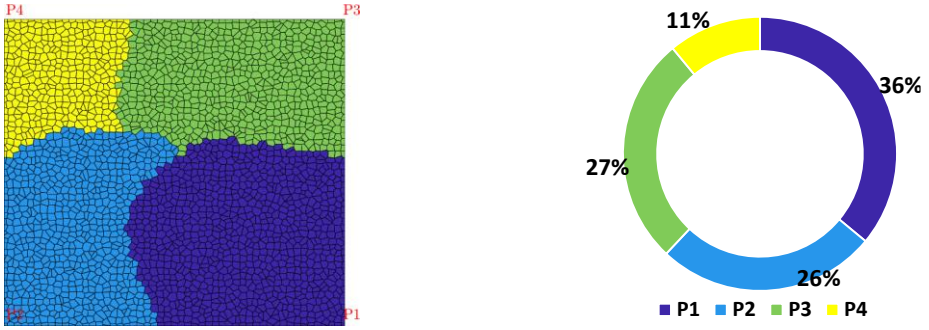

(a) Well drainage partition map (b) Well partition

Figure 4-4 Well drainage partition map and well partition pie chart for water-flooding model

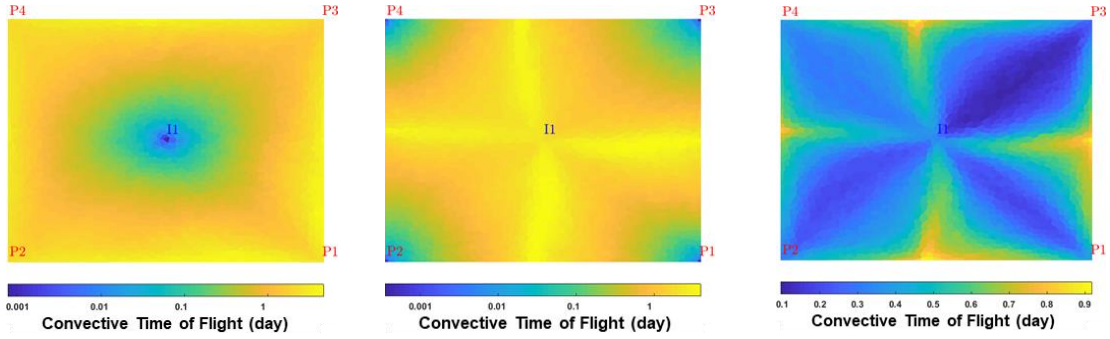

(a) (b) (c)

Figure 4-5 Convective time of flight from (a) producer, (b) injector, and (c) the totoal time of flight for the water-flodding model

The convective time of flight provides the tracer front from the injector or producer, as shown in Figure 4-5. The blue color denotes the easier accessible region for the. While the color turns yellow, it means those regions take more time to reach from wells. The sum of the injector and producer CTOF is the total CTOF, Figure 4-5 (c), which represents the sweeping channel between the injector and producer pair (blue color) and the stagnation area (yellow color). For the reservoir management, those stagnation areas are the candidate area of the future well development.

The dynamic Lorenz plot is another useful tool to analyze the heterogeneity of reservoir model. This plot is equivalent to the fractional flow curve on the saturation in the 1D Buckley-Leverett displacement theory. The ideal displacement is the diagonal line in this plot, which can be measured in the homogeneous model.

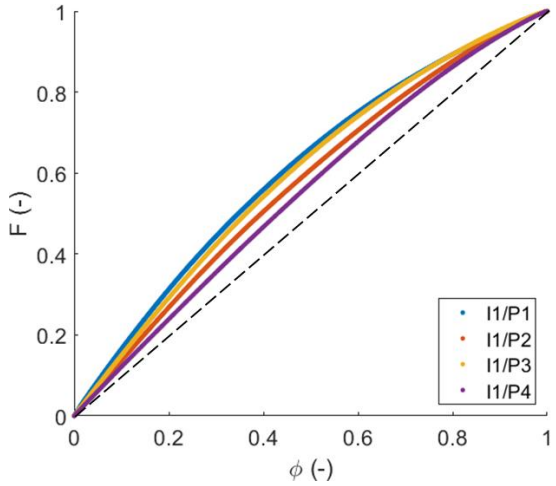

Figure 4-6 Dynamic Lorenz plot for water-flooding model

Table 4-1 Lorenz coefficient for each well pair in the water-flooding model

Well	Lorenz Coefficient
I1/P1	**0.215**
I2/P2	**0.148**
I3/P3	**0.195**
I4/P4	**0.103**

Figure 4-6 shows flow and storage capacity diagram for each well pair. Because the purple curve lies much closer to a linear curve corresponding to an ideal linear displacement, one can expect the higher recovery in the drainage region of I1/P4 pair. Table 4-1 shows the Lorenz coefficient for each well pair. The Lorenz coefficient is one of the most common measurement for the reservoir heterogeneity. The range of Lorenz coefficient is between 0 for a homogeneous displacement to 1 for an infinitely heterogeneous displacement.

4.3.2 Analysis of Primary Depletion Model

This model utilized the same permeability distribution as the water-flooding model has shown but shut in the injector at the model's center to simulate the primary depletion scenario. The initial pressure sets at 6000 psia to increase the reservoir energy. The single-phase simulation with slightly rock and fluid compressibility has been performed for 100 years of production. The total compressibility was 5×10^{-6}/psi and the oil viscosity was 1 cp at the initial reservoir pressure. In the primary depletion, no source comes from the well but the reservoir energy itself, which is the capacity of pore volume

in cells. This is suitable to test the compressible flow diagnostic, which built for the PSS condition. The permeability and pressure distribution are shown in Figure 4-7.

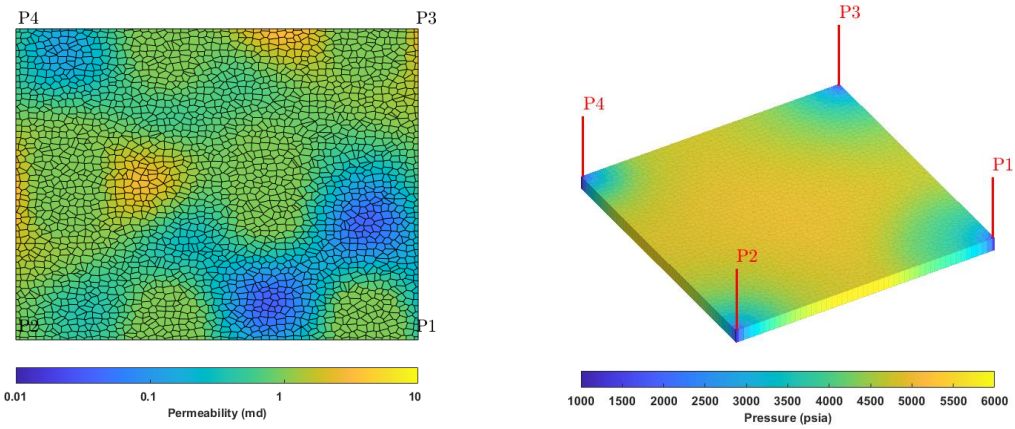

(a) (b)

Figure 4-7 (a) Permeability and (b) pressure distribution for primary depletion model

Figure 4-8 shows the well drainage partition map and well partition pie chart for primary depletion model at the time of 100 years production period. Without the injector the well drainage partition for each well pair is quite different from the water-flooding model shown in the Figure 4-4. We can now observe that the well drainage partition is strongly related to the permeability field.

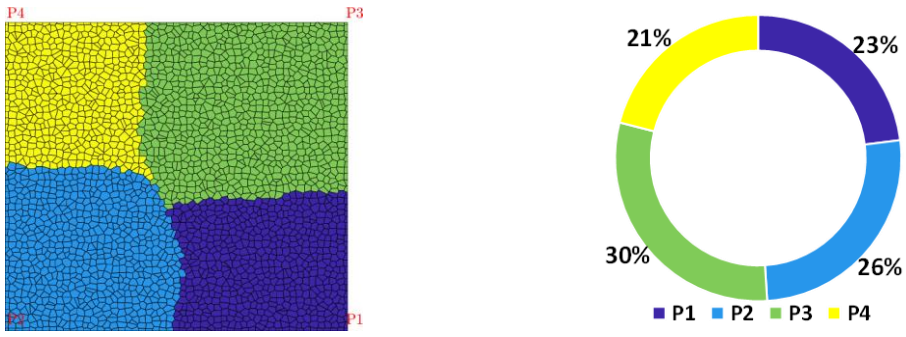

(a) (b)

Figure 4-8 Well drainage partition map and well partition pie chart for primary depletion model at the time of 100 years production period

The original flow diagnostic was built based on the SS condition, which assumes a stable flux field, but this is not the same for the compressible flow diagnostic. We expect the reservoir experienced the transient flow behavior followed by the boundary flow behavior. The flux field will then change with time by time resulting different drainage partition.

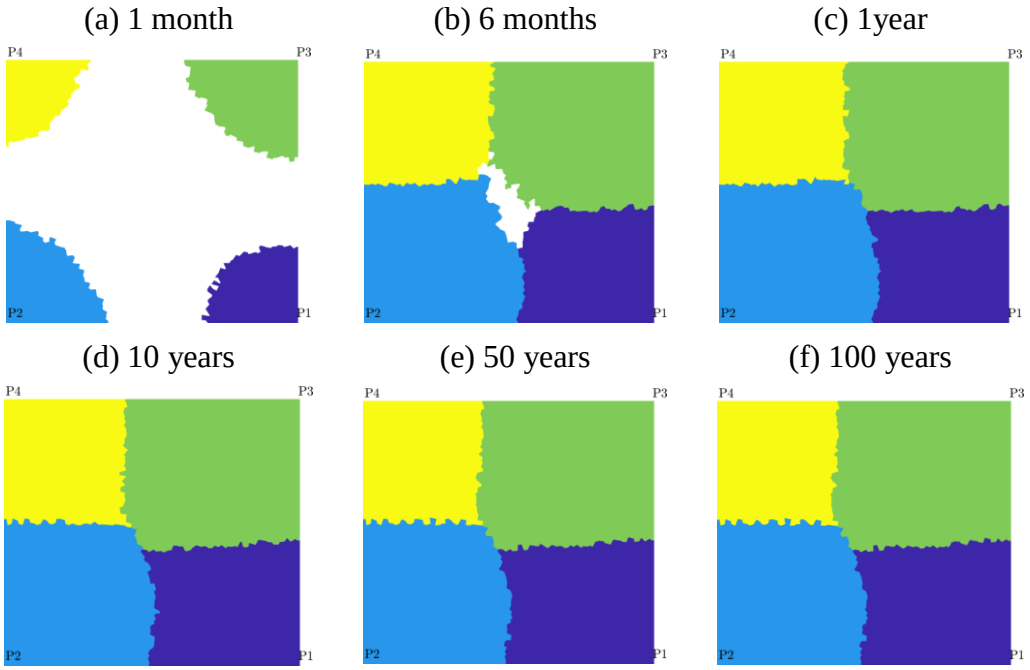

Figure 4-9 Drainage partition calculated based on the flux field at different time in the 100 years simulation time

Figure 4-9 shows how the drainage partition changes in the period of ten decades production and when the flux field begins to stabilize. The drainage partition quantified the production capacity for each producer and helped us to rank the well potential. The white area in the drainage partition is where the tracer has not reached. The drainage partition is stabilized after 10 years of production, and we can use the flux field at this

time to calculate the convective time-of-flight, as shown in Figure 4-9 (d). The drainage partition is stabilized after 10 years production and we can use the flux field at this time to calculate the convective time of flight, as shown in Figure 4-10. The value of the convective time of flight for the primary depletion model has enormously increased, and the stagnation area (yellow color) is identical with the drainage partition map. Noted that there is no time of flight from injector, which is why the dynamic Lorenz plot is unavailable to use here.

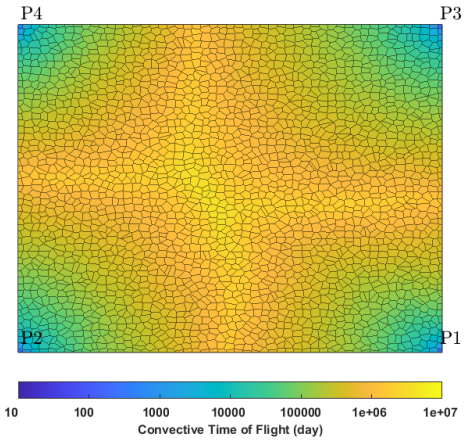

Figure 4-10 Convective time of flight from producer for primary depletion model

The pressure and pressure derivative map results during the 100 years of production period are shown in Figure 4-11 and Figure 4-12, respectively. The white contour indicates the threshold of 50% flux. The pressure maps present the life of reservoir from the transient flow to boundary dominate flow.

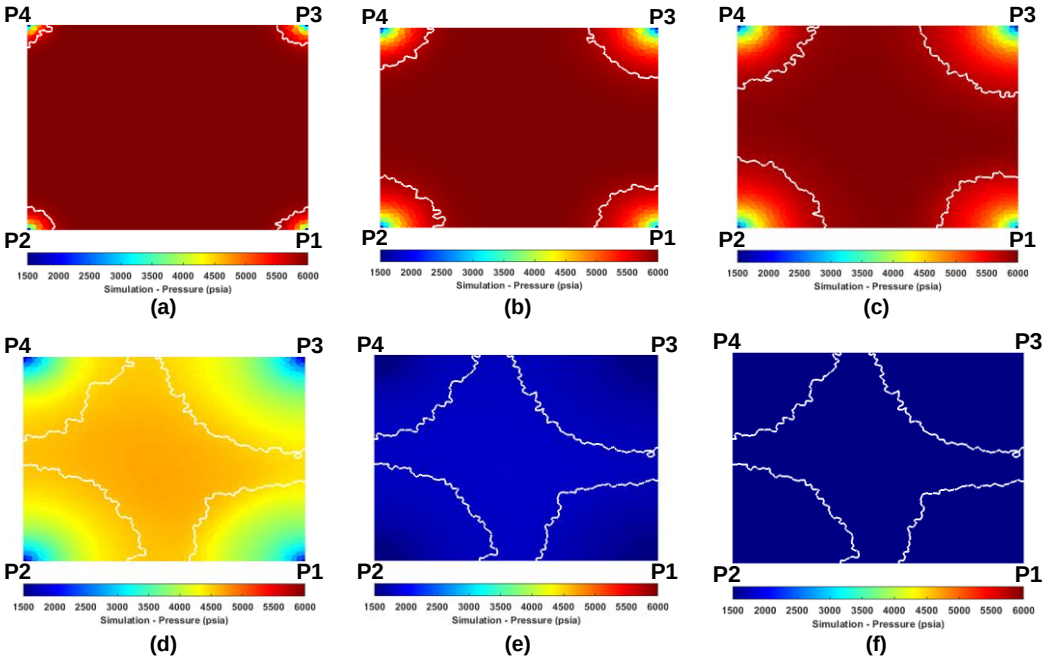

Figure 4-11 Pressure map during (a) 1 month; (b) 6 months; (c) 1 year; (d) 10 years; (e) 50 years; (f) 100 years. White contour presents the 50% flux region in the full drainage volume.

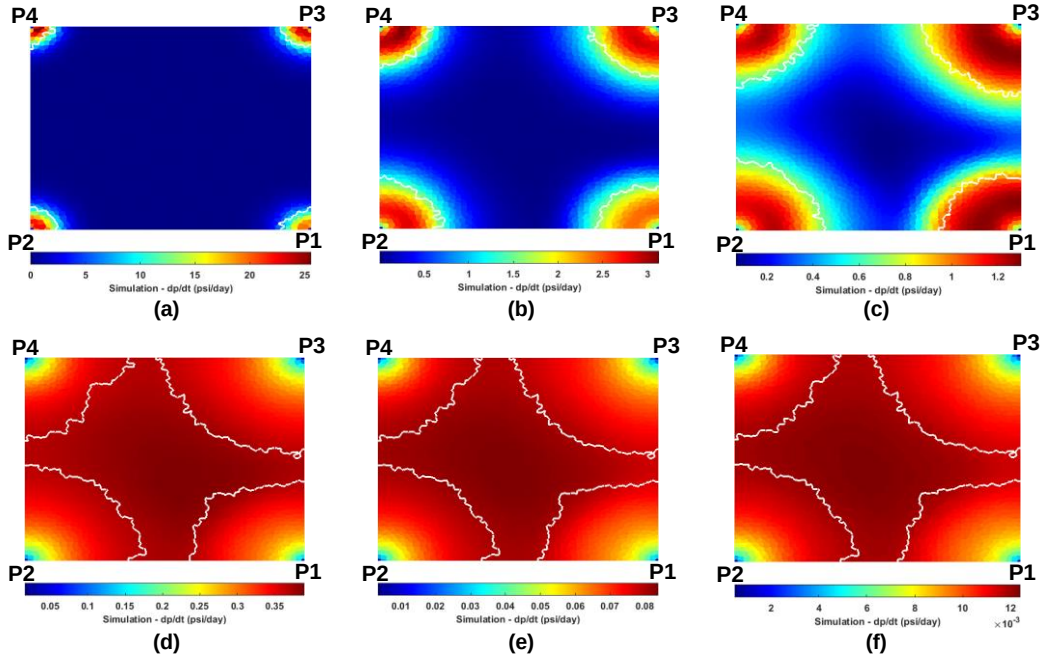

Figure 4-12 Pressure derivatives map at (a) 1 month; (b) 6 months; (c) 1 year; (d) 10 years; (e) 50 years; (f) 100 years. White contour presents the 50% flux region in the full drainage volume.

The pressure derivative maps highlight the pressure depletion region, which grows from the producers at early transient flow and covers the full reservoir after 10 years of production. The diagnostic region of 50% flux (white contour) represents the flow region with the substantially large pressure drop, as shown in Figure 4-12. This diagnostic region is then utilized to use as a threshold for the modified dynamic Lorenz plot.

The CTOF from producers within the diagnostic region of 50% flux in the 100 years production period is shown in Figure 4-13, which solved the issue of the infinity CTOF.

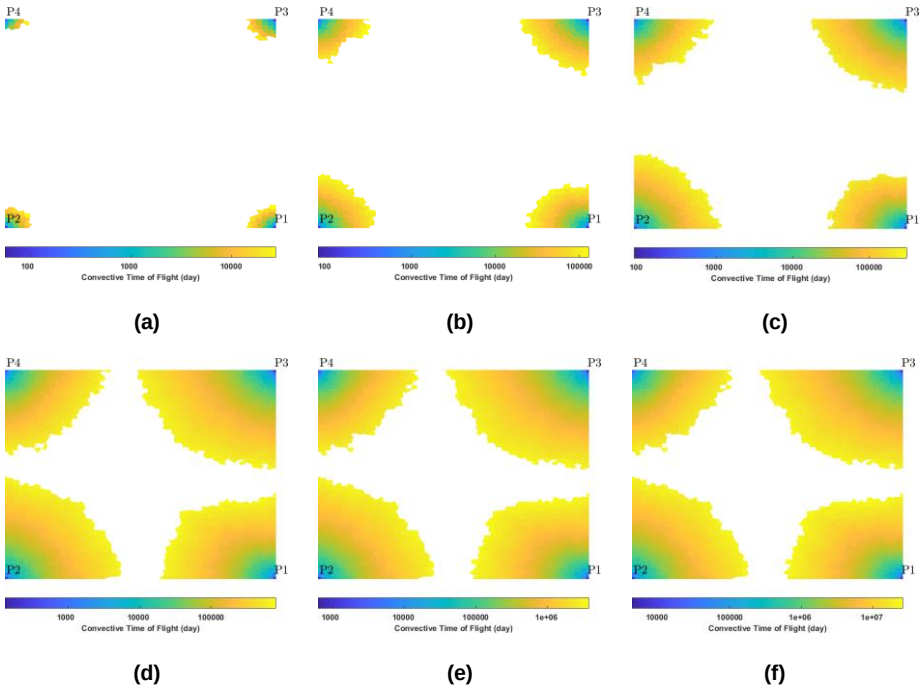

Figure 4-13 Convective time of flight map in the diagnostic region at (a) 1 month; (b) 6 months; (c) 1 year; (d) 10 years; (e) 50 years; (f) 100 years.

The CTOF tracing from sources at the boundary of diagnostic region is then computed by reversing the flux field and tracing the CTOF from the external source boundary to

the wellbore (as seen the water drive boundary in the field). The total CTOF now be defined as sums of the CTOF from the producer and the CTOF from the source boundary.

The resulting depletion Lorenz plot, for example, using 1 month production results, is shown in Figure 4-14. The depletion Lorenz plot with the threshold in diagnostic region of 50% flux, as shown in Figure 4-13, is not as skewed as the one without the threshold.

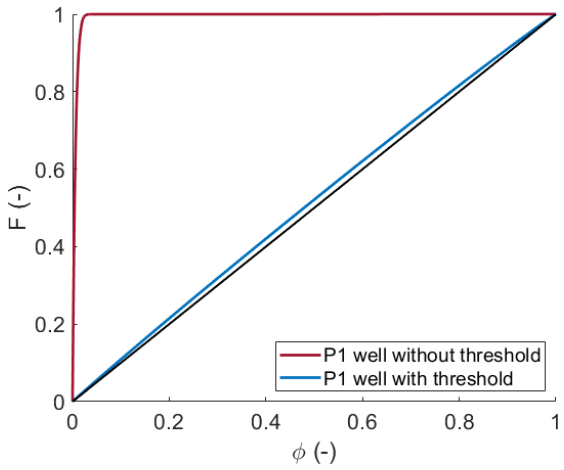

Figure 4-14 Depletion Lorenz plot at 1 month production. The red curve was calculated without the threshold. The blue curve was calculated with the threshold in diagnostic region.

These Lorenz curves also represent that even though the flux field is relatively homogeneous in this specific case, the results without utilizing the threshold to qualify the flow region will mislead the user to analyze the field.

4.3.3 Analysis of Multi-Hydraulic Fracture Well Model

In this section we built a synthetic model to simulate the multi-hydraulic fracture horizontal well connecting with the natural fracture on the 2D-PEBI grid. The permeability and the pressure drop distribution are shown in the Figure 4-15. The black line shows the location of the horizontal well (Figure 4-15 (a)). The hydraulic fractures perpendicular to the horizontal well and connect with the natural fractures are visually shown on the permeability map with million times larger permeability than the matrix has. The pressure drop distribution at 6 month shows the pressure propagation is aligned with the fractures (Figure 4-15 (b)).

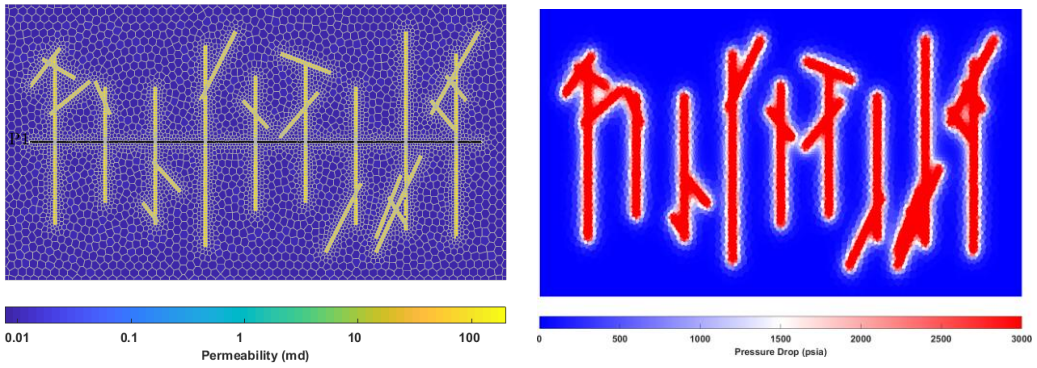

(a) (b)

Figure 4-15 Permeability and pressure distribution for MTFW 2D-PEBI Model

The porosity distribution for the matrix and fractures shows two Gaussian distribution models with the mean value around 0.5 for the matrix and mean value around 0.1 for the fractures, as shown in Figure 4-16 (a). The ratio of permeability to porosity distribution shows the matrix has a very tight and small K/ϕ ratio. On the other hand, the fractures have a logarithmic distribution with the left-skewed mean value, as shown in Figure 4-16 (b). The horizontal well has pressure constraint at 1000 psia for the

entire production period and the initial pressure of this reservoir is 6000 psia. The single phase simulation with slightly rock and fluid compressibility has been performed for 25 years of production.

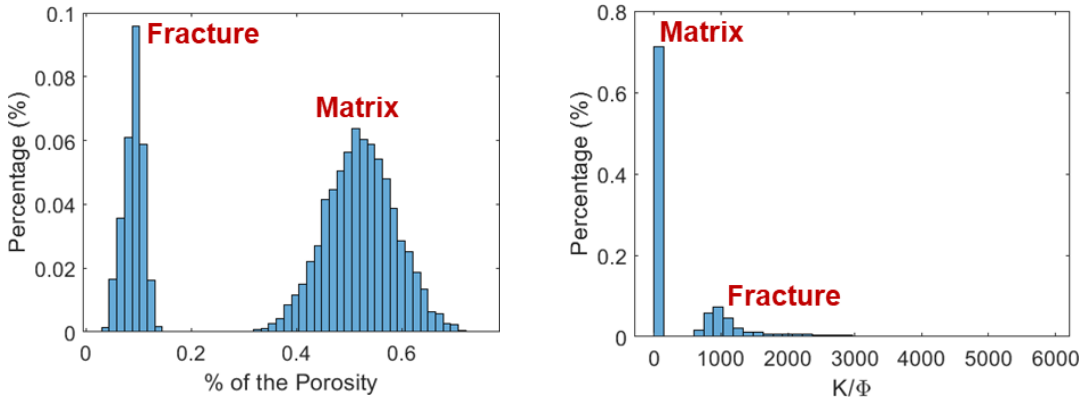

(a) Porosity distribution (b) Ratio of permeability to porosity

Figure 4-16 Porosity distribution and ratio of permeability to porosity

The horizontal well has pressure constraint at 1000 psia for the entire production period and the initial pressure of this reservoir is 6000 psia. The single phase simulation with slightly rock and fluid compressibility has been performed for 25 years of production.

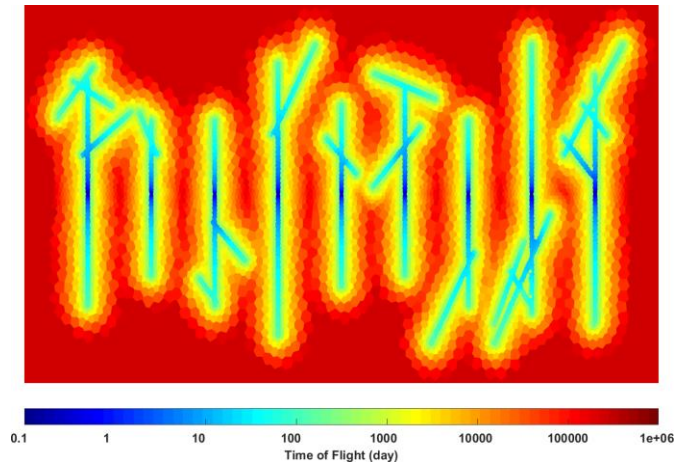

Figure 4-17 Convective time of flight from the perforation of horizontal well

Now let's look at the CTOF for this model using the 6 months result as an example, as shown in Figure 4-17. The blue color shows the easier accessible area and the red color, on the other hand, shows the harder accessible area. One can observe that the convective time of flight are tracing from the perforation cell on the horizontal well and propagating align with the hydraulic fractures to the nature fractures. After all the fractures are covered, the convective time of flight starts to move outward to the matrix.

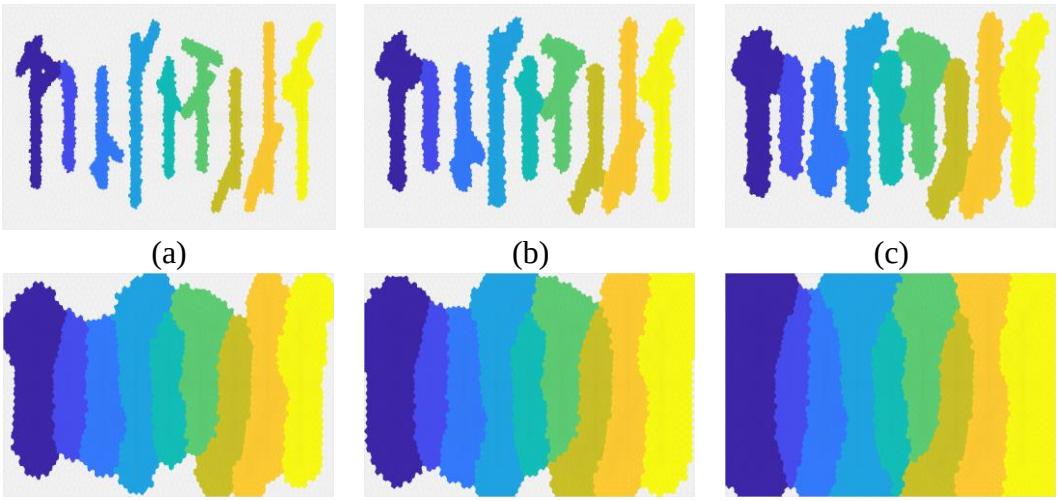

Figure 4-18 Drainage partition for each fracture in the 25 years production period

Figure 4-18 shows the drainage partition for each hydraulic fracture at different time points during the 25 years of production. The different color represents each different hydraulic fracture. At 1 month, the drainage partition covers the entire hydraulic fractures and nature fractures as observed in the convective time of flight. While time progress, one can observe that each drainage partition competes with each other. At the end of the simulation time, the middle of the fractures is squeezed and unable to grow out. On the other hand, the fractures on the sides are growing much

larger than the others. The drainage partition is a convenient tool to visualize the evolution of fractures and helpful for well and fracture development.

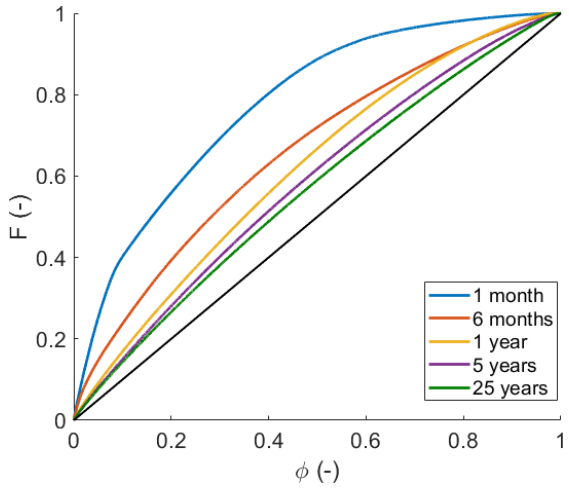

Figure 4-19 Depletion Lorenz plot in the period of 25 years production

The depletion Lorenz plot and corresponding Lorenz coefficient represent the encompassed heterogeneity in the diagnostic region at a given time. Figure 4-19 shows the depletion Lorenz plot in the period of 25 years of production. The depletion Lorenz curve is not independent of the time as the dynamic Lorenz curve in water flooding system. The Lorenz curves will gradually close to the diagonal line because the flux tends to stabilize if there is no new source contribute to the production. Thus, the Lorenz coefficient, which computed the twice area between the Lorenz curve and diagonal line at a given time, is not a uniform value and can be calculated as a function of time, as shown in Figure 4-20.

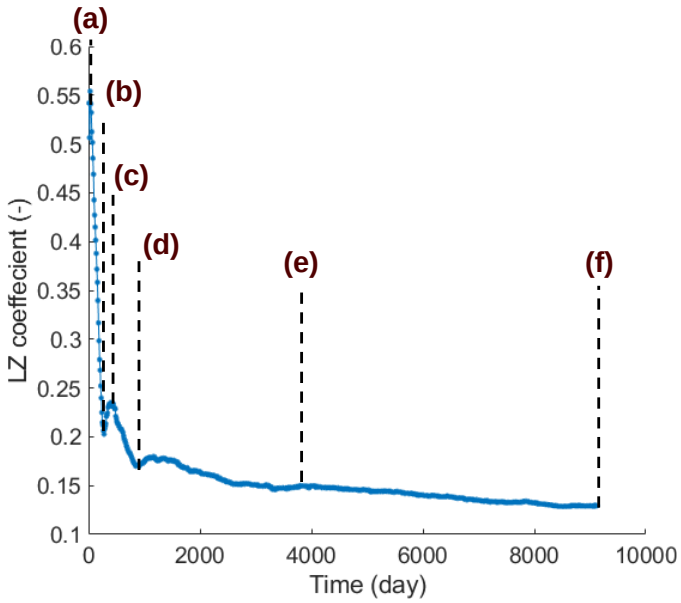

Figure 4-20 Depletion Lorenz coefficient plot. The indies present the time at (a) onset of matrix contribution; (b) strong matrix contribution; (d) onset of hydraulic fracture interference; (d) some nearby fractures combined; (e) strong hydraulic fracture interference; (f) fractures fully combined

Figure 4-20 presents the dynamic Lorenz coefficient in the 25 years production period, which characterizes the dynamic heterogeneity evolves with the time in the diagnostic region. The vertical dash line indicates the Lorenz coefficient at a specific time, and the corresponding CTOF is shown in Figure 4-21.

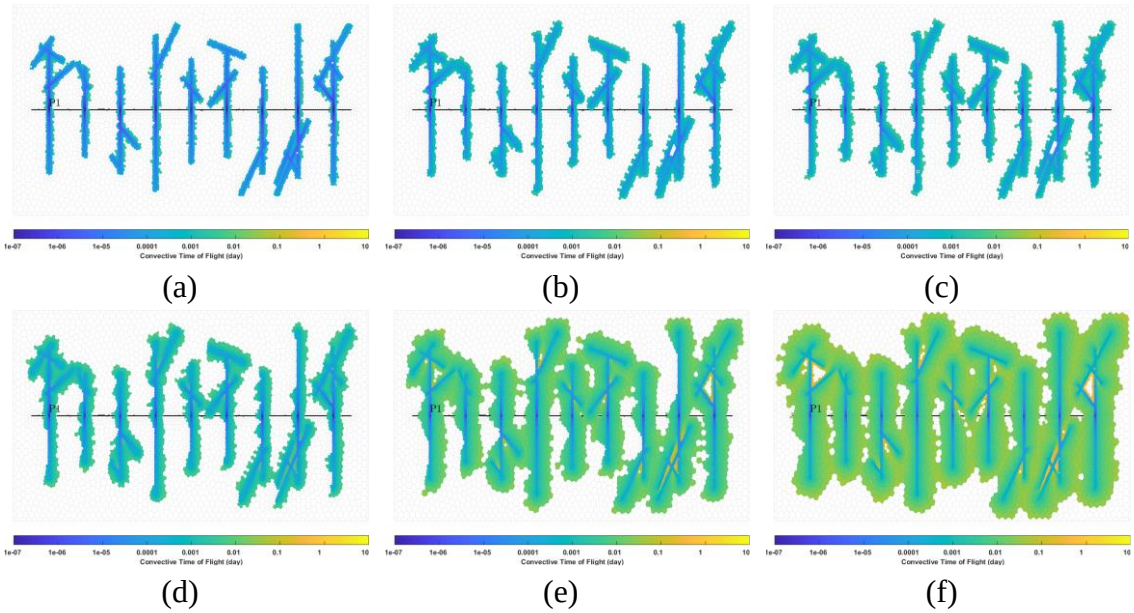

(a) (b) (c)

(d) (e) (f)

Figure 4-21 Convective time-of-flight map in the diagnostic region at (a) onset of matrix contribution; (b) strong matrix contribution; (c) onset of hydraulic fracture interference; (d) some nearby fractures combined; (e) strong hydraulic fracture interference; (f) fractures fully combined

The fluid particles will continue propagating outwardly from hydraulic fractures and natural fractures to the matrix. The first peak indicates in Figure 4-20 (a) is the onset of matrix contribution, which is the time that matrix starts adding to the production, as shown in Figure 4-21 (a). When more and more matrix contributes to the production in the diagnostic region, the Lorenz coefficient will decrease, as shown in Figure 4-20 (b) which indicates the time of the strong matrix contribution. The second peak in Figure 4-20 (c) indicates the onset of hydraulic fracture interference. The Lorenz coefficient is sensitive to the variation of flux field. However, when the flux field stabilized, the Lorenz coefficient will start to decrease again. With the time moving, the nearby hydraulic fractures or nature fractures will start to combine, which leads to a relatively small Lorenz coefficient indicating in Figure 4-20 (d). Consequently, when more and

more hydraulic fractures begin to interact with each other and merge together, the Lorenz coefficient well gradually decreases, as shown in Figure 4-20 (e) for the strong hydraulic fracture interference. At the late of the production period, the Lorenz coefficient will keep decrease, and we can observe the fractures fully combined, as shown in Figure 4-20 (f) and Figure 4-21 (f).

4.4 Analysis of Unconventional Reservoir Multi Transverse Hydraulically Fractured Well

This section the diagnostic by combining two distinct analytical/semi-analytical methods for determining pressure and fluid particle propagation in porous media. The multi-transverse fractured well is built and used as the reference model through our analysis. The CTOF represents the actual drainage volume and offers information on well partitioning and production capacity, which is crucial in reservoir management. The DTOF corresponds to the extent of the drainage volume. It leads to several definitions such as the depth of investigation, the limit of detectability, and the stabilized zone in the reservoir. Combining these two distinct concepts strengthens our ability to interact with the reservoir and extract more information than relying on one method.

4.4.1 Limit of Detectability and Stabilized Zone

The limit of detectability (LOD) describes how far a “detectable” pressure front propagates based upon a DTOF contour at a given time. The DTOF contour denoted the region or volume that was in transient flow at a given time. The definition of the LOD is

a consequence of the asymptotic pressure approximation of Eq. (1.15), which relates the strength of the rate of change of the pressure drop within the reservoir to the pressure drop at the wellbore, as governed by the exponential term, $e^{-\tau^2/4t}$. This term is known as the "Diffusion Kernel" and also describes the contribution of the reservoir pore volume to the transient drainage volume following Eq. (1.15). At a value of $\tau^2/4t = 4$, the exponential term is reduced to approximately 1.8% of its maximum value, and is used to define the limit of detectability.

$$\left(\tau^2/4t\right)_{LOD} = 4 \tag{4.14}$$

This is one of several measures of the extent of a pressure disturbance based on the concept of depth investigation (Kuchuk 2009). This limit of detectability corresponds to the time to the end of radial flow in bounded reservoirs (Lee 1982) and is equal to the end of linear flow indicated by Wattenbarger et al. (1998),as shown by Malone et al. (2019). Because of the exceptionally low reservoir permeability in an unconventional reservoir, transient flow dominates the drainage volume of most hydraulic fracture wells. The range of the limit of detectability highlights the region that contains any detectable transient flow at a particular time. Beyond the limit of detectability is the initial region, which has technically accessible reservoir capacity but does not experience considerable pressure disturbances.

Another important term is the depth of investigation (DOI), which both use the relationship between DTOF and real time. The DOI is defined for the infinite acting

linear flow, and can be used to measure the time that the significant fracture interference happens.

$$\left(\tau^2/4t\right)_{DOI} = 0.5 \tag{4.15}$$

In contrast, the stabilized zone (SZ) describes a smaller volume describing the extension of a PSS region from the wellbore. In the well test literature, the concepts of drainage volume and stabilization time are widely used. It is the time requiring for the entire reservoir to reach boundary dominated flow and to be able to contribute to production (Hossain et al. 2007). However, this concept may not be helpful in unconventional reservoirs as transient flow dominates the time on production due to the low reservoir permeability. Therefore, in this analysis, we instead define the stabilized zone, following Malone et al. (2019), as being determined by the transient drainage volume (TDV). For fixed rate draw-down, the transient drainage volume covers a PSS region close to the wellbore and a region of transient depletion beyond that. For variable rate drawdown, the drainage volume of the well may be determined using the rate normalized pressure drop and material balance time, as a specific example of superposition time for boundary dominated flow.

$$\frac{1}{V_d\left(t_e\right)} = \frac{c_t}{t_e}\frac{d\left(RNP\right)}{d\ln\left(t_e\right)} \tag{4.16}$$

Here $V_d\left(t_e\right)$ is the transient drainage volume and is a function of material balanced time. The TDV can use to analyze a well or individual fracture, and relate to the cumulative pore volume based on the DTOF, $V_p\left(\tau\right)$, at a specific time.

$$V_d\left(t_e\left(t\right)\right)=V_p\left(\tau\right) \tag{4.17}$$

The relationship of TDV and cumulative pore volume allows us to visualize the stabilized zone of the entire hydraulically fractured well by projecting the associated DTOF contour onto the reservoir model. Noted that the analysis of LOD and SZ can be directly calculated by the actual well data rather than utilizing inputs from a reservoir model. Nevertheless, in order to avoid unnecessary noise from the field data, such as flow back, workovers, well shut-ins due to any well operations, and so forth, we resort to using the synthetic reference well.

4.4.2 Analysis of Multiple Transversely Fractured Well Model (MTFW)

In this section we demonstrated the analysis of synthetic multiple transversely fractured well model (MTFW). This model was first reported by {Malone, 2019 #104@@author-year}. This synthetic well model has 10 transverse hydraulic fractures modeled by Eclipse, as shown in Figure 4-22.

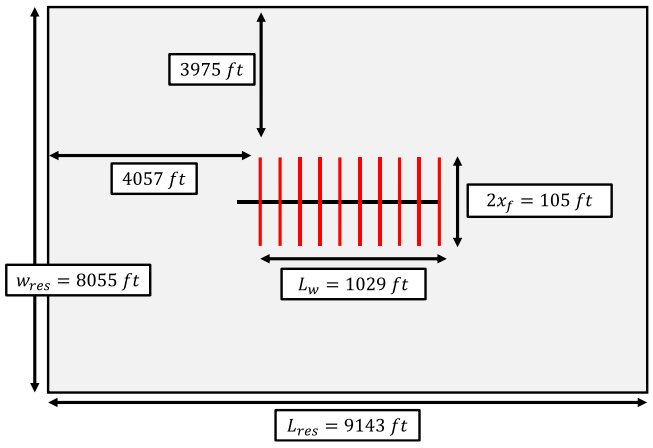

Figure 4-22 Geometry of synthetic well model; Wellbore indicated as black line; hydraulic fractures indicated as red lines

The other reservoir and fluid properties used in the Eclipse prototype simulation are provided from Table 4-2. The BHP was set as 5000 psi, causing the well to produce at a declining rate and slowing down the reservoir depletion rate to enable plausible production forecast time series over two decades.

Table 4-2 Reservoir parameters for MTFW model

Reservoir Properties	
Rock and Fluid Properties	
SRV Permeability, k_{SRV}	500 nD
Background Permeability, k	50 nD
Porosity, ϕ	6%
Oil viscosity, μ	1 cp
Oil compressibility, c_o	1E-5 psi^{-1}
Formation volume factor, B_o	1 rb/stb
Residual oil saturation, S_{or}	0
Pay height	30 ft
Rock Compressibility, c_R	1E-5 psi^{-1}
Model Fracture Properties	
Fracture half-length, x_f	52.5 ft
Fracture spacing	100 ft
Number of fractures	10
Fracture width, w_f	0.02 ft
Fracture permeability, k_f	5000 md

The pressure depletion maps generated by Eclipse is shown in Figure 4-23 for different times in the life of the prototype well. Although the well rate is low (25 stb/day as starting condition and gradually decreasing after switching to BHP constraint), the pressure transients propagate from the individual fractures into the reservoir space such that diffusive pressure fronts of adjacent fractures meet after about 1 year of production.

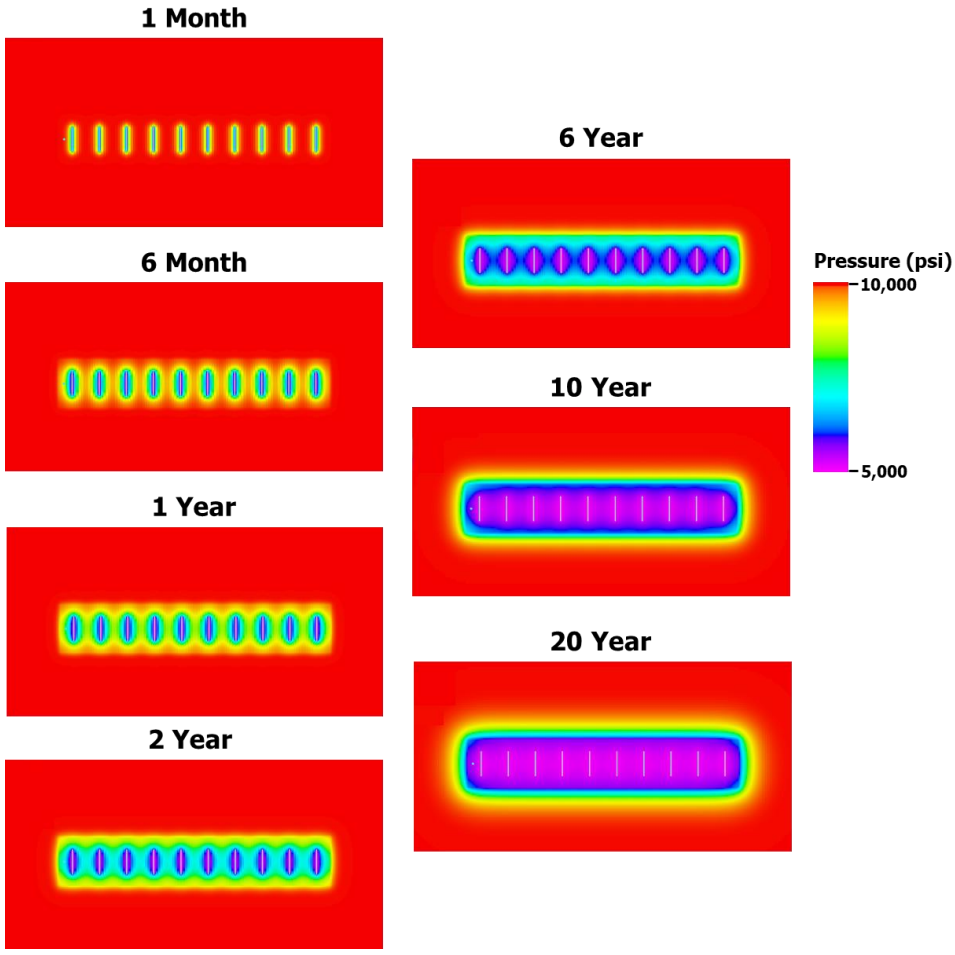

Figure 4-23 Pressure depletion map during 20 years production; The early depletion occurs near the hydraulic fractures at 1 month; After 1 year of production, fractures begin to interfere with each other; The pressure gradually propagates outward as a rectangular outline after 2 years of production

The whole reservoir region between the hydraulic cracks has reached the fixed BHP constraint after around 10 years of production. The pressure depletion in the region between the hydraulic fractures occurs relatively early in the well life and the transitions form one flow regime to the other have been described in various recent studies (King et al. 2016, Malone et al. 2019). Interestingly, after roughly a year, when the pressure transient interacts with the neighboring fractures, apparent boundary dominated flow

occurs. The well will be in secondary transient flow for most of the well life because the boundary of the reservoir space was set relatively far from the well and its fracture tips Because the pressure transient has not reached the reservoir's outer edge, actual boundary dominated flow will still not occur after 20 years of production. Furthermore, the phenomenon that the outline of the pressure transient propagates outward as a rectangular box after first year production, as shown in Figure 4-23, is mainly due to the assumptions made for this prototype well model. The rectangular stimulated reservoir volume (SRV) region was specified at the center of this model, where the fractures inside it have a small homogeneous matrix permeability (as shown in Figure 4-24 with 500 nD).

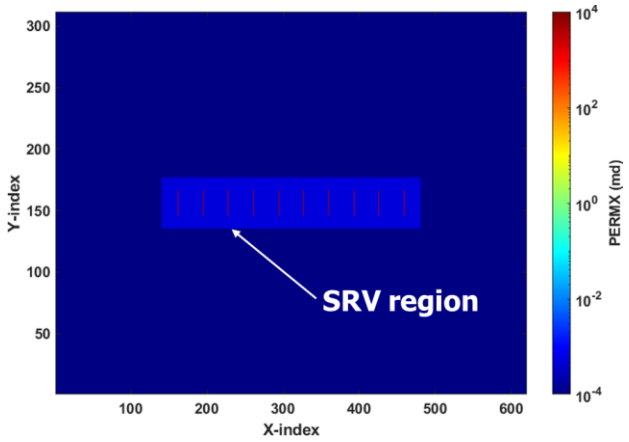

Figure 4-24 Permeability map for reservoir model

Outside of the region of SRV has a homogeneous background permeability (one order smaller than permeability in SRV with a value of 50 nD). As a consequence, the pressure transient tends to fill the rectangular region of SRV before extending outward in the same rectangular shape.

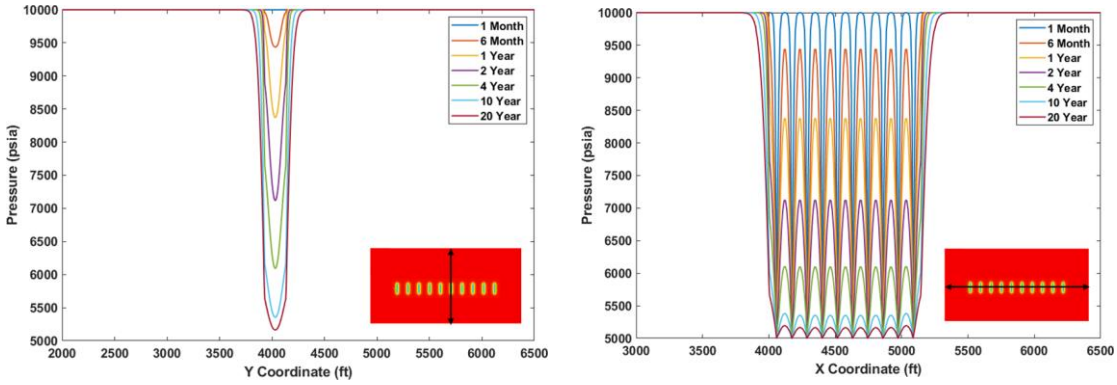

(a) (b)

Figure 4-25 Pressure depletion along (a) Y direction and (b) X direction in MTFW model

This graphical description of pressure depletion around modeled hydraulic fractures can also be displayed as pressure graphs along both the X and Y axes of the reservoir model, as shown in Figure 4-25.

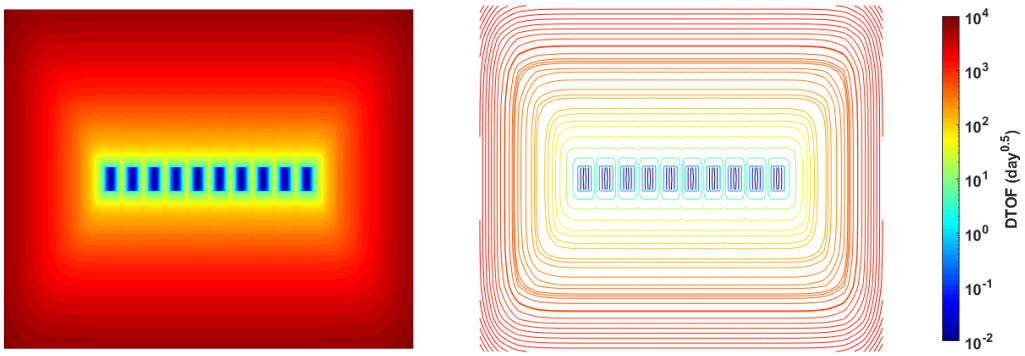

(a) (b)

Figure 4-26 Diffusive time of flight computed from the FMM. (a) shows the color map, and (b) shows the contour map.

We then looked at the results of FMM. The DTOF determining from FMM has minimal values in the hydraulic fractures and grows externally as the pressure front advances outside of the horizontal well (Figure 4-26). The DTOF represents the impulse of pressure front, which propagates from the hydraulic fractures to the entire reservoir.

We can also determine the cumulative pore volume as a function of the DTOF for the MTFW model using the DTOF computed from the FMM. One feature of the FMM solution is converting the 3D flow simulation to an equivalent 1D flow simulation with DTOF contour as the spatial coordinate. While the DTOF contour propagates outwardly from the horizontal well to the entire reservoir domain, we can add up the pore volume that it reaches to get a sense of how quickly the pressure front propagates outwards.

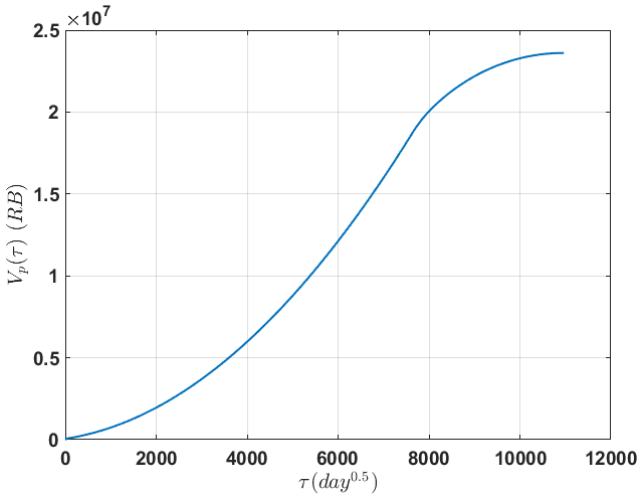

Figure 4-27 Cumulative pore volume as a function of the DTOF for the MTFW model

Figure 4-27 depicts how the pressure front propagates rapidly as the pore volume grows exponentially near the hydraulic fractures at the early time. As the pressure front advances toward the outer matrix with decreased permeability, the propagation speed gradually slows down until boundary effects are detected.

Now we used the compressible flow diagnostic results to analyze the MTFW model. The drainage partition of each fracture in the diagnostic region during 20 years of production is shown in Figure 4-28. This synthetic model has a uniform fracture space, which leads to a uniform drainage partition for each fracture. However, after 10 years of production, the fracture on the left and right sides has a relatively larger drainage partition because there is less fracture interference.

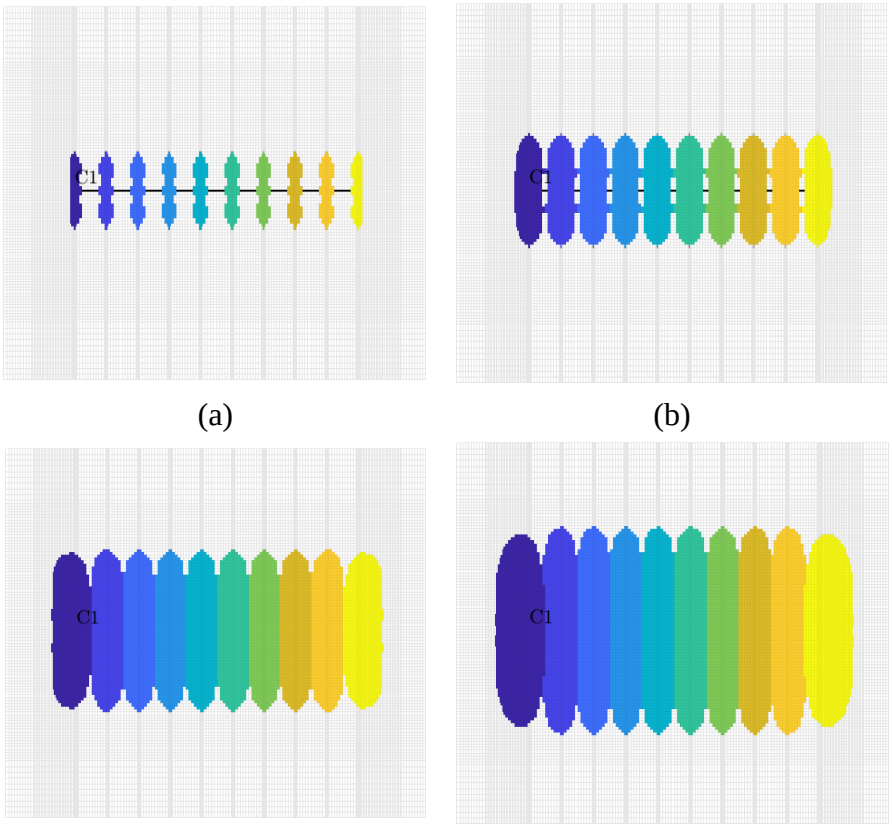

(a) (b)

(c) (d)

Figure 4-28 Drainage partition in the diagnostic region at (a) 1 month; (b) 1 year; (c) 10 years; (d) 20 years.

The Lorenz coefficient computed from the depletion Lorenz plot can be utilized to quantify the general heterogeneity encompassed in the drainage region. The value of

the Lorenz coefficient was calculated based on the region selected from the diagnostic region during the 5 years production, as shown in Figure 4-29. The CTOF and pressure derivative distribution at the specific time indicated in Lorenz coefficient plot are shown in Figure 4-30 and Figure 4-31, respectively.

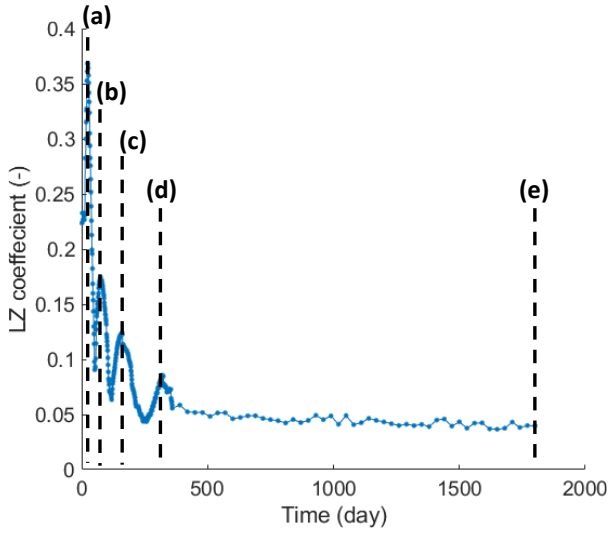

Figure 4-29 Lorenz coefficient plot. The indies present the time at (a) onset of matrix contribution; (b) onset of hydraulic fracture interference; (c) strong hydraulic fracture interference; (d) fractures fully combined; (e) flow begins to move out from SRV region.

The Lorenz coefficient versus time is noisy because the flux field is not monotonically growing or shrinking with the time in the diagnostic region. The Lorenz coefficient starts at a low quantity and initially decreases in a very short time because the drainage volume is drained only in the immediate vicinity of the fractures. Linear flow exists in this period, and it then quickly hit the first peak at the beginning of bilinear flow (Figure 4-29 (a)), where the fluid front advances out from each hydraulic fracture to the nearby matrix. The CTOF depicts the spatial path of the tracer front, as shown in

Figure 4-30 (a). The associated pressure derivative distribution also presents that the two sides of fracture have stronger pressure drop, as shown in Figure 4-31 (a).

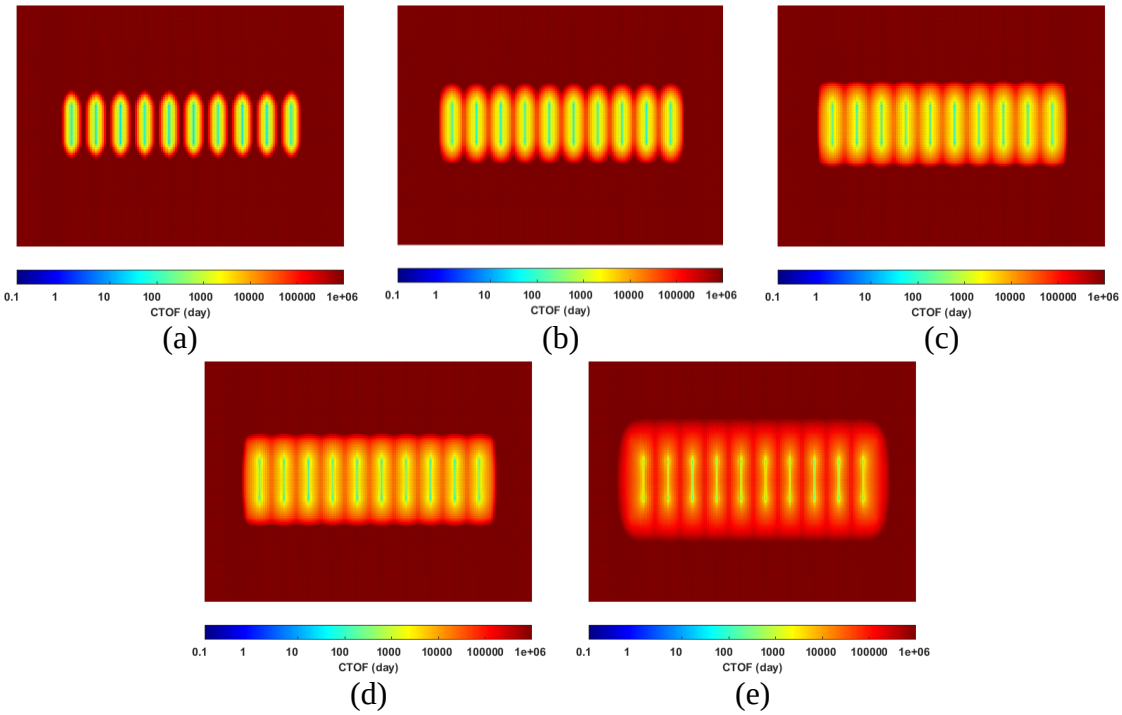

Figure 4-30 Convective time-of-flight map at (a) onset of matrix contribution; (b) onset of hydraulic fracture interference; (c) strong hydraulic fracture interference; (d) fractures fully combined; (e) flow begins to move out from SRV region.

When the fractures grow in the SRV region, the fracture will start to interference with each other. The onset of hydraulic fracture interference is indicated at the second peak in the Lorenz coefficient, as shown in (Figure 4-29 (b)). The CTOF shows the spatial area of each hydraulic fracture (Figure 4-30 (b)). The associated pressure derivative also indicates that the pressure drop is stronger along each fracture (Figure 4-31 (b)). The third peak of the Lorenz coefficient highlights the stronger fracture interference, as shown in Figure 4-29 (c). The pressure derivative distribution presents the hydraulic fractures begin to merge together (Figure 4-31 (c)). The last peak in the

Lorenz coefficient indicates the time that the hydraulic fractures fully combined (Figure 4-29 (d)). At this time, the region of significant pressure drop is still inside the SRV region, as shown in (Figure 4-31 (d)). The Lorenz coefficient is then gradually decreasing after fracture is fully combined. After 5 years of production, the fractures have formed a single collective drainage region and advanced out from the SRV region to the background matrix, as shown in Figure 4-29 (e) and visualized in Figure 4-30 (e).

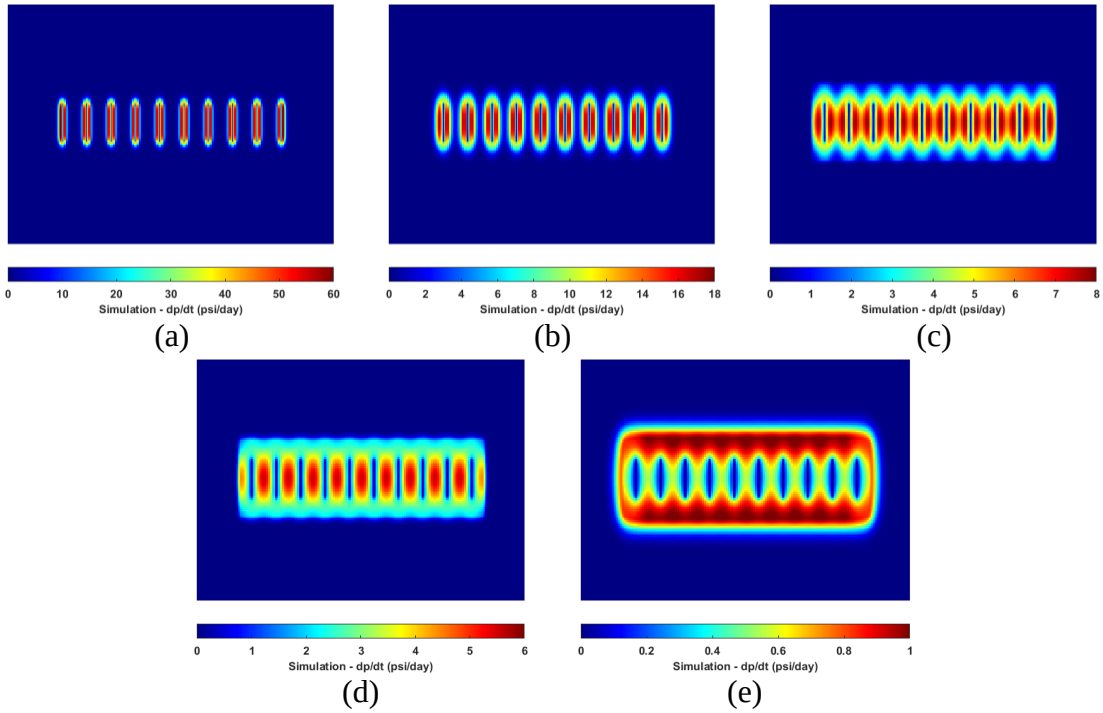

Figure 4-31 Pressure derivative map at (a) onset of matrix contribution; (b) onset of hydraulic fracture interference; (c) strong hydraulic fracture interference; (d) fractures fully combined; (e) flow begins to move out from SRV region.

Based on production allocation, the CTOF can relate the actual drained rock volume from individual hydraulic fractures. It can also estimate the tracer path deflections caused by nearby natural fractures (if present). Figure 4-32 depicts the pressure and pressure derivative map at production durations of 6 months and 20 years,

respectively. The region of actual drained rock volume, stabilized zone (SZ), and limit of detectability (LOD) are indicated in these figures for the fracture analysis.

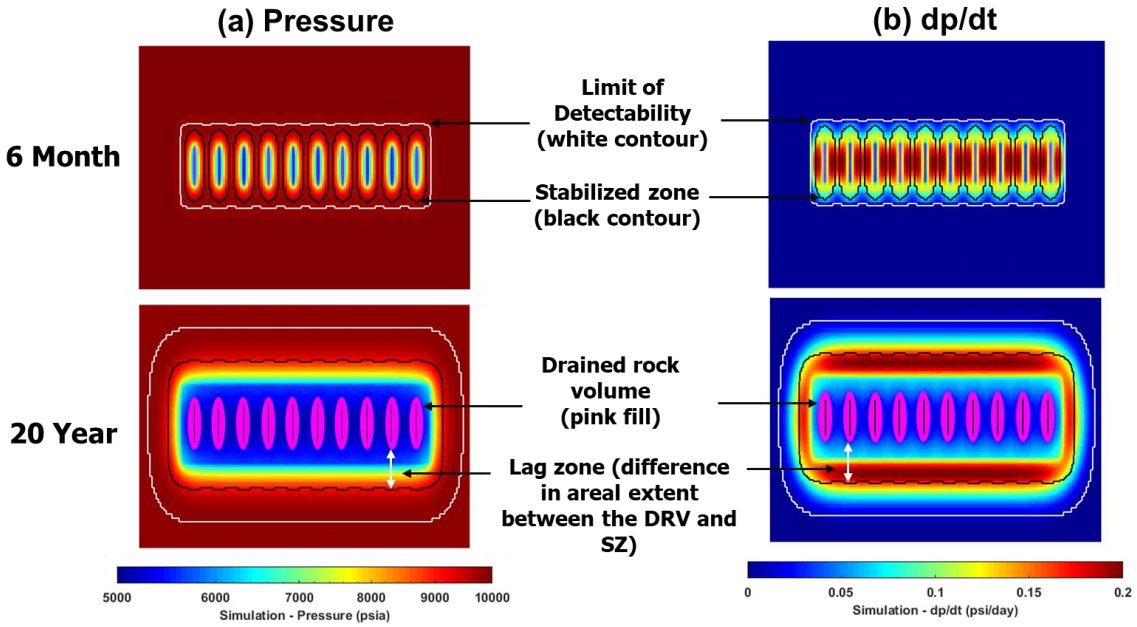

Figure 4-32 (a) pressure depletion (background color scale) after 6 months and 20 years production, and visual comparison of lag zone between DRV from convective time of flight (pink color fill); (b) dp/dt at 6 months production and at 20 years production; Stabilized zone shown in full black contour and Limit of Detectability given as white contour in both (a) and (b); The hydraulic fractures spacing of 100 ft with hydraulic fracture half-length of 52.5 ft are designed in this model

The area between the actual drained rock volume (pink-filled ellipses) and the pressure depletion from the Eclipse simulation is the lag zone. The stabilized zone presents the extension of PSS flow, which highlights the region of a significant pressure derivative. The area between actual drained rock volume and SZ (black contour line) shows the difference between the actual drained rock volume and transient drainage volume. The LOD contour (white contour line) indicates the area of the reservoir that starts to enter the transient flow regime, with the area beyond the LOD contour is the

reservoir volume still at the initial condition, as shown in Figure 4-32 (b). In addition, the discrepancy between actual drained rock volume and LOD (the white line) describes the difference between the area that can be observed from the CTOF (fluid front) and DTOF (pressure front). The pressure derivative map explains where the highest intensity of fluid expansion is happening in the reservoir and visually displays the drainage area at a given time, as shown in Figure 4-32 (b).

We have visualized the fracture interference in the spatial domain by using the SZ and LOD. The LOD can also utilize to determine the fracture interference in the real time domain. This approach is similar to the depth of investigation (DOI), which both use the relationship between DTOF and real time. The DOI is defined for the infinite acting linear flow, and can be used to measure the time that the significant fracture interference happens. Furthermore, the SZ indicates the transient drainage volume that is accessible from the well.

The management of reservoirs requires understanding the defined and calculated based on the transient drainage volume and the wellbore response.

$$UR = c_t \Delta V_p \Delta p_{wf} \tag{4.18}$$

Here, c_t is the total compressibility, ΔV_p is the reservoir pore volume, and Δp_{wf} is the well bottomhole pressure drop, flowing at a constrained pressure. This ultimate recovery potential for the improvement of production. The ultimate recovery (UR) is not a function of time, and indicates the technical limit of the volume recovered by pressure depletion. Figure 4-33 shows plots of the instantaneous recovery, $c_t \Delta V_p(\vec{x}, t)$, and the ratio of the instantaneous to the ultimate recovery at 6 months and 20 years of

production, respectively. A contour line has imposed on Figure 4-33 representing the LOD (white contour line) to highlight the region of transient drainage volume (i.e., the region of the reservoir that starts to enter the transient flow regime).

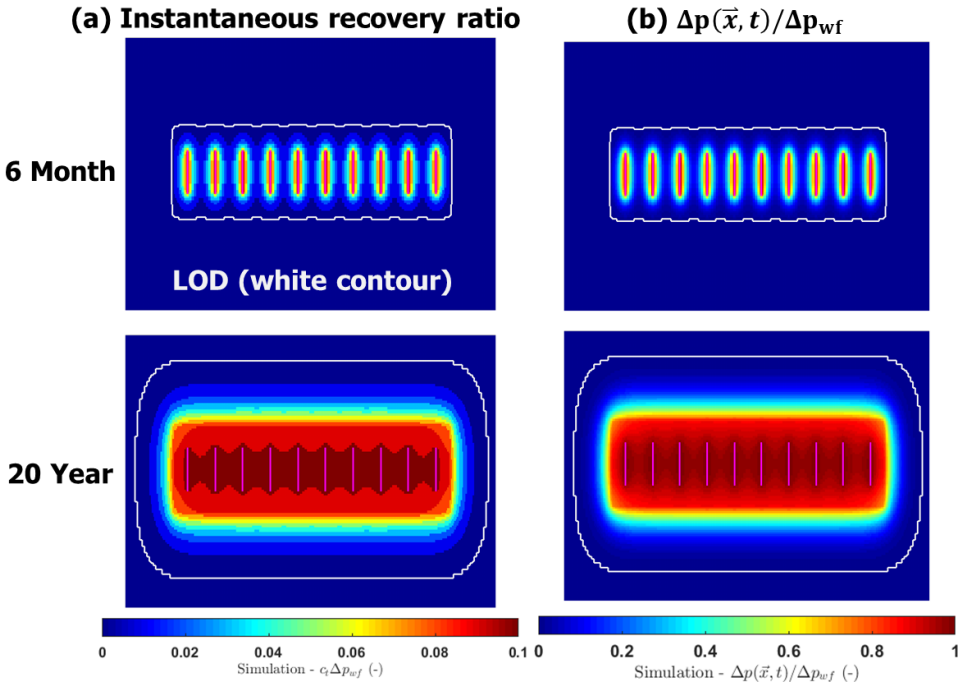

Figure 4-33 (a) Map of ultimate recovery ratio (Top: 6 months production, Bottom: 20 years production) and (b) The ratio of pressure drop to bottomhole pressure drop at 6 months and 20 years production respectively. The Limit of Detectability given as white contour.

We may make several observations based on these figures. First, the magnitude of the instantaneous recovery does not exceed 10% anywhere in the reservoir. This is a consequence of pure reservoir depletion, and can only be increased by dropping the bottomhole flowing pressure. Second, the ratio of instantaneous to ultimate recovery quickly reaches close to 100% near the hydraulic fractures, and extends over most of the SRV at later times. This shows that the multiple stages of hydraulic fracturing are

working as intended, and reach close to the technical limit of recovery. Finally, the last observation is that this depletion remains in a transient region, even at late times. The extent of the transient region, or more specifically the extent of the region that is not influenced by the well, is well described by the limit of detectability.

We have visualized the ratio of ultimate recovery in space. We may also examine the concept of the stabilized zone in more detail. In Figure 4-34, we determine the recovery from the stabilized zone following Eq. (4.18), in which we have a depleted pressure of Δp_{wf} within the stabilized zone, and a pressure drop of zero beyond that.

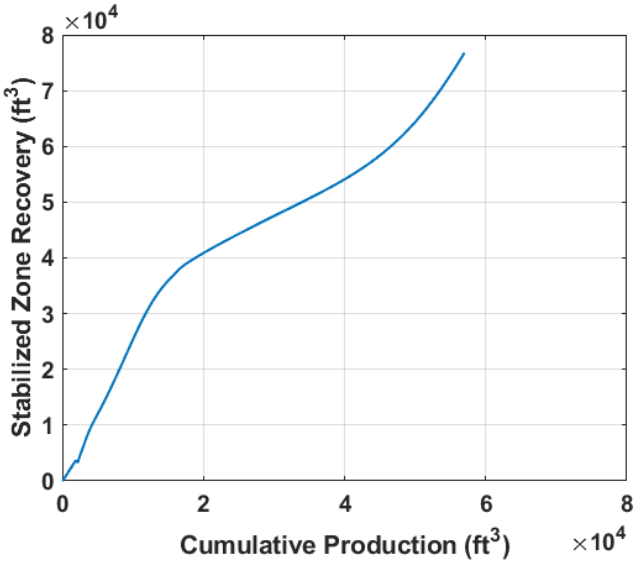

Figure 4-34 Stabilized zone recovery for the synthetic MTFW model

This recovery is compared to the actual cumulative recovery. In the absence of fracture interference, all of the pressure depletion would be due to outwardly moving pressure disturbances, and the relationship between drainage volume and reservoir pore volume would follow Eq. (1.15). We would then expect a straight line with a unit slope.

In fact, we do not find an exact correspondence indicating that the stabilized zone, i.e., a region of uniform PSS depletion is not consistent with the multi-fracture depletion seen in the flow simulation.

The onset of the fracture interference can be determined in the real time domain from the definition of LOD, as shown in Figure 4-35. Another useful relationship between DTOF coordinate and real time is the depth of investigation. Applying the depth of investigation for the infinite acting linear flow, $\tau^2/4t = 0.5$, we can observe when the strong fracture interference happens, as shown in Figure 4-35. Since the transient drainage volume, $V_d(t)$, indicates the pore volume of the reservoir that is accessible to the well and is independent operational changes, the production data can be incorporated into the analysis using the Instantaneous Recovery Ratio (Yang et al. 2016). The Instantaneous Recovery Ratio (IRR) can be expressed as Eq. (4.19).

$$IRR = \frac{N_p(t)}{V_d(t)} \tag{4.19}$$

The IRR is the ratio of the cumulative production from the well to the drainage volume accessible to the well at any time and is reported as a percentage representative of how efficiently or how quickly the accessible drainage volume is produced.

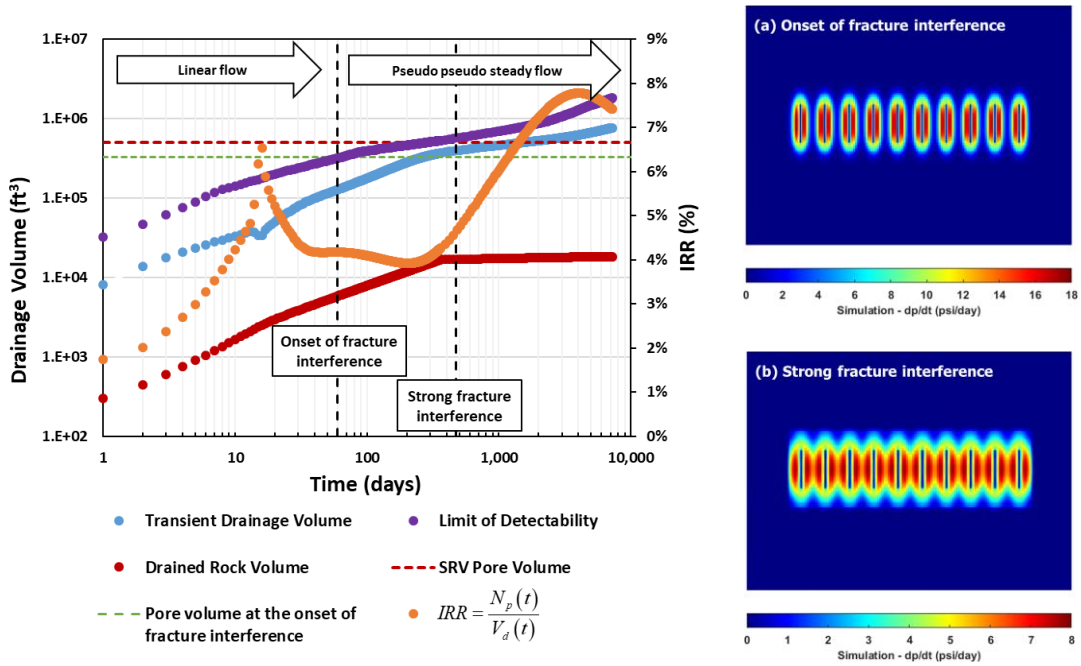

Figure 4-35 Diagnostic of Instantaneous Recovery Ratio. The horizontal lines show the pore volume at the onset of fracture interference (green line) and SRV pore volume (red line). The vertical lines indicate the onset of fracture interference and the strong fracture interference

Tracking the IRR and transient drainage volume, $V_d(t)$, together (Figure 4-35) shows high correlation with physical and operational changes in the reservoir. The IRR initially increases sharply because the drainage volume is drained only in the immediate vicinity of the fractures. Linear flow exists in this time period and we briefly hit a peak where the operational constraint is changed from fixed rate to fixed BHP. The IRR subsequently starts to decline owing to the reduction in the flow rate to honor the fixed BHP constraint. This reduction stabilizes to a flat spot that will end when each growing fracture drainage area begins to encounter interference from the adjacent fractures and form the stagnation lines between the fractures. The beginning of this fracture-fracture

interference is indicated by the first dashed vertical line in Figure 4-35. Since the model does not have a fixed rate drawdown maintained during the entire production period, the flow behavior after the onset of fracture interference is more precisely called the "Approximate Volumetric Flow." The IRR then tends to take a slight dip due to the strong fracture interference effect until all the fracture drainage areas are fully combined and form a single collective drainage volume as shown in the pressure gradient plots (Figure 4-35 (a)).

The pore volume for the onset of fracture interference (green horizontal line) also indicates the time when fracture drainage areas are completely combined. The linear depth of investigation, as detailed above, can be used to determine the time when strong fracture interference occurs. At this time, we can observe the strong pressure gradient forms between each fracture (Figure 4-35 (b)) and IRR begins to increase due to the growth of this collective drainage volume. The collective drainage volume will then grow into the reservoir at a slower pace, which will occur after the drainage volume grows beyond the SRV pore volume (red horizontal line). The growth of the IRR will end and begin to decrease when the background matrix is no longer capable of supporting an increase of drainage volume due to the low permeability. In realistic situations, this will not be the case since the region of SRV is not a clearly defined boundary in the field.

The actual drained rock volume (red dot) and the transient drainage volume (blue dot) have at least one order difference in value, which shows the potential to increase the production by the well or fracture allocation. The actual drained rock volume stops

growth after the strong fracture interference effect occurs because the SRV region is depleted, and producing the background matrix is inefficient. This phenomenon may not be seen as the actual field doesn't have a specific SRV region.

The difference between the transient drainage volume (blue dot) and LOD (purple dot) represents pressure propagation between the significant pressure depletion region and the impulse of pressure front. The transient drainage volume is always lower than the LOD. The time that the growth of the LOD slows down indicates the pressure propagating to the outside of the SRV region (red horizontal line). In the meantime, the transient drainage volume is still increasing. However, the slope of transient drainage volume decreases after reaching the pore volume at the onset of fracture interference (green horizontal line).

4.5 Discussion

The interaction between the two physically distinct fronts provides new insights into the development of undrained regions in unconventional reservoirs. The development of large lag zones between the drained rock volume (DRV, denoted by the tracer front) and the transient drainage volume (indicated by the stabilized zone) requires to be aware and mitigated because hydrocarbons in the lag zone remain largely undrained.

The pressure front often moves at least one order of magnitude quicker than the tracer front, resulting in the creation of these lag zones, particularly in ultra-low permeability shale reservoirs. The leading edge of this propagating pressure front can be

determined using the DTOF calculations and in our study is demarked by the limit of detectability with the stabilized zone showing stronger depletion. The limit of detectability is the extent at which the derivative of pressure with respect to time equals approximately 1.8% of its maximum value as given in Eq. (4.14). The stabilized zone is the extent within the reservoir that is between the full PSS region and initial conditions and is equivalent to the transient drainage volume.

The compressible flow diagnostic is developed for the reservoir in the primary depletion model or the unconventional reservoir without the need for an injector, as shown in Figure 4-30. The FMM is applicable to adjust the internal and external boundary effect, which presents a better characterization for the pressure propagation, as shown in Figure 4-26. The tracer front always arrives after the pressure front. As the pressure front moves outwards into the reservoir, fluid molecules begin moving towards the hydraulic fractures and are eventually produced at the wellhead. To determine where these fluid molecules are drained from in the reservoir, we use the process of flow reversal to create a tracer front that moves out into the reservoir from the hydraulic fractures. The tracer front and its propagation are calculated from the CTOF and is dependent on both the production rate and reservoir properties. This difference between the propagating pressure front and the actual DRV is termed the lag zone. The lag zone represents the reservoir region that is pressure depleted but where the fluid molecules have not yet reached the producing well. Spatial visualization of the DRV is given in Figure 4-32 and demonstrates that the reservoir space between the individual hydraulic fractures has not been drained even after 20 years production. This relation and

corresponding disparity between the propagating pressure front and tracer front (explained in simple terms in Table 4-3) is primarily responsible for the extremely low recovery factors typical in unconventional reservoirs.

Table 4-3 Descriptive terms for depleted reservoir regions

Limit of Detectability (LOD)	This is the area up to where the pressure pulse moving outwards from the hydraulic fracture is detectable
Stabilized Zone	The transient drainage volume, i.e. that volume of the reservoir that is in significant depletion due to the imposed pressure change
Drained Rock Volume (DRV)	The volume of the reservoir that has been drained of all movable fluid molecules which contributes to the production of the well/ hydraulic fractures (Weijermars et al. 2020)

The drainage process in the reservoir can be summarized as follows. Whereas the pressure front advance measured by the DTOF creates a pressure gradient that begins to move all fluid in this region, only a small portion of this moving fluid will reach the well during it productive life, with this portion given by the CTOF. The question then becomes how can operators mitigate the lag zone to improve productivity? A first step is the recognition of the lag zone as shown in this study via the use of pressure depletion plots with the corresponding calculated DRVs. Pinpointing exactly where in the reservoir is undrained, especially the undrained areas between the hydraulic fractures, can lead to more efficient placement of refractures that can access undrained reservoir sections. The creation and extent of the lag zone is determined mainly by reservoir parameters of fluid viscosity, reservoir permeability and porosity (Weijermars et al. 2020). One possible method to both reduce fluid viscosity while also increasing reservoir pressure is the use of enhanced oil recovery (EOR) methods such as carbon dioxide or

methane injection. Operators should seek to implement these learnings to boost productivity by increasing recovery factors in these unconventional reservoirs.

4.6 Chapter Summary

In this chapter, we generalized and validated the compressible finite difference flow diagnostics. The flow diagnostics were demonstrated for water flooding, primary depletion, and multi-transverse hydraulic fracture well models, representing the flexibility and convenience of this tool. The depletion Lorenz plot and coefficients are developed for the model without explicit injectors by selecting the diagnostic region that contributes strong flux to the well.

We have reported a detailed look at various complementary methodologies possible to approximate the changes in a subsurface reservoir due to production from man-made hydraulic fractures. Due to production two distinct propagating fronts have been identified, the transient pressure front (modeled using the diffusive time of flight) and the moving tracer front (modeled using the convective time of flight). Our synthetic model shows that the edge of the pressure front can be represented by either the Limit of Detectability (the minimum pressure pulse can be detected) or the Stabilized Zone (the significant depletion due to pressure imposed). The tracer front can be calculated by the drained rock volume (DRV) or pore volume (DPV) and represents the actual bulk rock or pore volume around the hydraulic fracture which contributes to the produced fluid.

CHAPTER V

CONCLUSION AND FUTURE RESEARCH DIRECTIONS

5.1 Summary and Conclusions

The improvement of the diffuse source upscaling has been developed demonstrated in SPE10 and Amellago carbonate outcrop reservoir model. The novel near well upscaling workflow has been developed and improved understanding of the near well flow behavior.

The developed local flow based PSS/DS Transmissibility and SS well index upscaling with the SSM face transmissibility correction has been applied to upscale the geologic model for flow simulation. The critical element of our approach is the use of superposition to ensure that the local calculation is consistent with arbitrary global flow fields. We demonstrated the new near well workflow to an industry general upscaling workflow and tested it on three reservoir sector models (SPE10, Amellago carbonate outcrop, and former Soviet Union shale model).

The finite difference compressible finite difference flow diagnostics was generalized and validated in water flooding, primary depletion, and multi-transverse hydraulic fracture well models in 2D-PEBI grid, representing the flexibility and convenience of this tool. The application of flow diagnostic for multi-scale modeling helps us rank the coarse model in both qualitative and quantitative ways. The compressible flow diagnostic can be furthered used in unconventional model and optimization well or fracture spacing.

We reported the usage of the compressible flow diagnostic and the FMM in the unconventional reservoir. Combining these two methods provides a detailed look of the growth of each fracture, fracture interference, and an indication of the flow after touching the SRV region. The spatial location of the tracer front is obtained by measuring the convective time of flight. The actual drained rock volume that contributed to the production can be indicated on the spatial domain using the convective time of flight. On the other hand, the pressure propagation is observing by the diffusive time of flight and can be identified as either the impulse of pressure front (represented as the limit of detectability) or the significant pressure depletion region (described as the stabilized zone).

5.2 Future Research Direction

The upscaling formulation was developed based on the analysis of the intrinsic reservoir properties (i.e., permeability distribution). Often, we assume the fluid properties do not strongly affect the flow behavior in our research. However, the near-well flow region, which has substantial pressure depletion, may alert the multi-phase flow impact. Hence, a more sophisticated study for multi-phase flow upscaling is required in future studies.

The application of compressible flow diagnostic is not limited in the single horizontal well diagnostic. The further studied of the parent/child well pattern or well pattern development are plausible and helpful for developed plan.

NOMENCLATURE

Property	Description	Unit of Measure	Conversion to SI
Latin			
c_t	Total compressibility	$1/psi$	$(1/6894.76)/Pa$
F	Flow capacity	$[1]$	
k	Permeability	mD	$9.869233\times10^{-16}m^2$
k_H	Horizontal permeability	mD	$9.869233\times10^{-16}m^2$
k_V	Vertical permeability	mD	$9.869233\times10^{-16}m^2$
p	Pressure	psi	$6.89476\times10^{3}Pa$
$p_{face,k}$	Pressure on face k	psi	$6.89476\times10^{3}Pa$
p_{wf}	Bottom hole pressure	psi	$6.89476\times10^{3}Pa$
p_i	Pressure in grid block i	psi	$6.89476\times10^{3}Pa$
q_w	Well flux	ft^3/day	$\left((0.3048)^3/24\right)m^3/hr$
q_f	Total face flux	ft^3/day	$\left((0.3048)^3/24\right)m^3/hr$
S	Source/Sink strength	ft^3	$(0.3048)^3\,m^3$
t	Time	hr	hr

t_{PSS}	Time to reach pseudo steady state	hr	hr
$\vec{u}$	Darcy velocity	ft/day	$(0.3048/24)\,m/hr$
$T_{i,k}$	Intercell transmissibility on face *k*	$mD\cdot ft$	$(9.869233)(0.3048)\times 10^{-16}\,m^3$
T^{DS}	Diffuse source transmissibility	$mD\cdot ft$	$(9.869233)(0.3048)\times 10^{-16}\,m^3$
T_{ℓ}	Intercell transmissibility in direction ℓ	$mD\cdot ft$	$(9.869233)(0.3048)\times 10^{-16}\,m^3$
T_f^{SS}	Steady state face transmissibility	$mD\cdot ft$	$(9.869233)(0.3048)\times 10^{-16}\,m^3$
T_f^{PSS}	Pseudo steady state face transmissibility	$mD\cdot ft$	$(9.869233)(0.3048)\times 10^{-16}\,m^3$
T_f^{SSM}	Steady state face transmissibility with mixed no flow and isobar pressure boundaries (one flowing face)	$mD\cdot ft$	$(9.869233)(0.3048)\times 10^{-16}\,m^3$
T_f^{PSSQM}	Face transmissibility based on the PSSQ well index and the SS mixed boundary conditions (one flowing face)	$mD\cdot ft$	$(9.869233)(0.3048)\times 10^{-16}\,m^3$
T_f^{PSSPM}	Face transmissibility based on the PSSP well index and the SS mixed boundary conditions (one flowing face)	$mD\cdot ft$	$(9.869233)(0.3048)\times 10^{-16}\,m^3$
V_p	Pore volume	ft^3	$(0.3048)^3\,m^3$
$V_{p,i}$	Pore volume of grid block i	ft^3	$(0.3048)^3\,m^3$
$V(t)$	Transient drainage volume	ft^3	$(0.3048)^3\,m^3$

WI	Well index	$mD \cdot ft$	$(9.869233)(0.3048)\times 10^{-16} m^3$
WI^{SS}	Steady state well index	$mD \cdot ft$	$(9.869233)(0.3048)\times 10^{-16} m^3$
WI^{PSSQ}	PSS well index with no flow boundary	$mD \cdot ft$	$(9.869233)(0.3048)\times 10^{-16} m^3$
WI^{PSSP}	PSS well index with isobar pressure boundary	$mD \cdot ft$	$(9.869233)(0.3048)\times 10^{-16} m^3$
z_k	Flux error measurement in fine scale	ft^3/day	$\left((0.3048)^3/24\right) m^3/hr$
$\tilde{z}_k$	Flux error measurement in coarse scale	ft^3/day	$\left((0.3048)^3/24\right) m^3/hr$

Greek

α	Hydraulic diffusivity	ft^2/hr	$(0.3048)^2\, m^2/hr$
Δp^{SS}	Pore volume averaged steady state pressure difference	psi	$6.89476\times 10^3 Pa$
Δp^{DS}	Diffuse source pressure drop	psi	$6.89476\times 10^3 Pa$
Δp^{PSSQ}	Pseudo steady state pressure drop with no flow boundary	psi	$6.89476\times 10^3 Pa$
Δp^{PSSP}	Pseudo steady state pressure drop with isobar pressure boundary	psi	$6.89476\times 10^3 Pa$
ϕ	Porosity	$[1]$	
Φ	Storage capacity	$[1]$	
μ	Fluid viscosity	cp	$10^{-3} Pa \cdot \sec$
τ	Diffusive time of flight	$\sqrt{hr}$	$\sqrt{hr}$

τ^c	Convective time of flight	*day*	*86400 sec*
τ_j	Diffusive time of flight of cell j	$\sqrt{hr}$	$\sqrt{hr}$
$\overline{\tau}$	Average diffusive time of flight	$\sqrt{hr}$	$\sqrt{hr}$

ABBREVIATIONS

AHCSS	Analytical half-cell steady state transmissibility upscaling
AWI	Analytical well productivity index
CTOF	Convective time of flight
DS	Diffuse source
DPV	Drained Pore Volume
DRV	Drained Rock Volume
DTOF	Diffusive time of flight
FMM	Fast Marching Method
HCSS	Half-cell steady state transmissibility upscaling
K	Cell based upscaling
LOD	Limit of Detecability
PSS	Pseudo steady state
PSSP	Pseudo steady state well index upscaling with the isobar pressure boundary
PSSPM	Mixed PSSP well index upscaling and SSM face transmissibility upscaling
PSSQ	Pseudo steady state well index upscaling with the no flow outer boundary

PSSQM	Mixed PSSQ well index upscaling and SSM face transmissibility upscaling
PVWI	Pore volume weighted well index upscaling
SS	Flow based steady state transmissibility upscaling
SSM	Flow based steady state face transmissibility upscaling with isobar pressure on one side of the boundary
SZ	Stabilized Zone

REFERENCES

Alpak, Faruk O., Pal, Mayur, and Lie, Knut-Andreas. 2012. A Multiscale Adaptive Local-Global Method for Modeling Flow in Stratigraphically Complex Reservoirs. *SPE Journal*. https://doi.org/10.2118/140403-PA.

Alpak, Faruk Omer. 2015. Quasiglobal Multiphase Upscaling of Reservoir Models with Nonlocal Stratigraphic Heterogeneities. *SPE Journal*. https://doi.org/10.2118/170245-PA.

Ates, Harun, Bahar, Asnul, Salem, Salem et al. 2005. Ranking and Upscaling of Geostatistical Reservoir Models Using Streamline Simulation: A Field Case Study. *SPE Reservoir Evaluation & Engineering - SPE RESERV EVAL ENG* **8**: 22-32.

Begg, S. H., Carter, R., and Dranfield, P. 1989. Assigning effective values to simulator gridblock parameters for heterogeneous reservoirs. *SPE Reservoir Engineering*. https://doi.org/10.2118/16754-PA.

Blunt, Martin, Liu, Kuiran, and Thiele, Marco. 1996. A Generalized Streamline Method to Predict Reservoir Flow. *Petroleum Geoscience* **2**: 259-269.

Bøe, Øistein. 1994. Analysis of an upscaling method based on conservation of dissipation. *Transport in Porous Media* **17** (1): 77-86. https://doi.org/10.1007/BF00624051.

Borregales, M., Møyner, O., Krogstad, S. et al. 2020. Data-Driven Models Based on Flow Diagnostics. **2020** (1): 1-11. https://www.earthdoc.org/content/papers/10.3997/2214-4609.202035122.

Boumi Mfoubat, H.R.N. and Zaky, E.I. 2020. Optimization of waterflooding performance by using finite volume-based flow diagnostics simulation. *Journal of Petroleum Exploration and Production Technology* **10** (3): 943-957. https://doi.org/10.1007/s13202-019-00803-5.

Bratvedt, F., Gimse, T., and Tegnander, C. 1996. Streamline computations for porous media flow including gravity. *Transport in Porous Media* **25** (1): 63-78. https://doi.org/10.1007/BF00141262.

Cardwell, W. T. and Parsons, R. L. 1945. Average Permeabilities of Heterogeneous Oil Sands. *Transactions of the American Institute of Mining and Metallurgical Engineers*. https://doi.org/10.2118/945034-G.

Chawathe, Adwait and Taggart, Ian. 2004. Insights Into Upscaling Using 3D Streamlines. *SPE Reservoir Evaluation & Engineering* **7** (04): 285-296. https://doi.org/10.2118/88846-PA.

Chen, Y., Durlofsky, L. J., Gerritsen, M. et al. 2003. A coupled local–global upscaling approach for simulating flow in highly heterogeneous formations. *Advances in Water Resources* **26** (10): 1041-1060. https://doi.org/10.1016/S0309-1708(03)00101-5.

Chen, Yuguang and Durlofsky, Louis J. 2006. Adaptive Local–Global Upscaling for General Flow Scenarios in Heterogeneous Formations. *Transport in Porous Media* **62** (2): 157-185. https://doi.org/10.1007/s11242-005-0619-7.

Cheng, Hao, Osako, Ichiro, Datta-Gupta, Akhil et al. 2006. A Rigorous Compressible Streamline Formulation for Two and Three-Phase Black-Oil Simulation. *SPE Journal* **11** (04): 407-417. https://doi.org/10.2118/96866-PA.

Christie, M. A. 1996. Upscaling for Reservoir Simulation. *Journal of Petroleum Technology*. SPE-37324-JPT. https://doi.org/10.2118/37324-JPT.

Christie, M.A. and Blunt, M.J. 2001. Tenth SPE Comparative Solution Project: A Comparison of Upscaling Techniques. Paper presented at the SPE Reservoir Simulation Symposium. SPE-66599-MS. https://doi.org/10.2118/66599-MS.

Christie, Michael Andrew, Wallstrom, T. C., Durlofsky, L. J. et al. 2000. *Effective medium boundary conditions in upscaling*, Los Alamos National Laboratory Technical Report LA-UR-00-2804 (Reprint).

Darman, N. H., Pickup, G. E., and Sorbie, K. S. 2002. A Comparison of Two-Phase Dynamic Upscaling Methods Based on Fluid Potentials. *Computational Geosciences* **6** (1): 5-27. https://doi.org/10.1023/A:1016572911992.

Datta-Gupta, A. and King, M. 2007. *Streamline Simulation: Theory and Practice*. Richardson, Texas: Textbook Series, Society of Petroleum Engineers.

Datta-Gupta, Akhil, Xie, Jiang, Gupta, Neha et al. 2011. Radius of Investigation and its Generalization to Unconventional Reservoirs. *Journal of Petroleum Technology* **63**: 52-55. SPE-0711-0052-JPT. https://doi.org/10.2118/0711-0052-JPT.

Desbarats, A. J. 1992. Spatial averaging of hydraulic conductivity in three-dimensional heterogeneous porous media. *Mathematical Geology* **24** (3): 249-267. https://doi.org/10.1007/BF00893749.

Deutsch, C. V. and Journel, A. G. 1998. *GSLIB. Geostatistical Software Library and User's Guide*, 2nd edition. Oxford: Oxford University Press.

Dijkstra, E. W. 1959. A note on two problems in connexion with graphs. *Numerische Mathematik* **1** (1): 269-271.

Ding, Didier. 2004. Near-Well Upscaling for Reservoir Simulations. *Rev Inst Fr Pét* **59**: 157-165. https://doi.org/10.2516/ogst:2004012.

Ding, Didier Yu. 2010. Modeling Formation Damage for Flow Simulations at Reservoir Scale. *SPE Journal* **15** (03): 737-750. https://doi.org/10.2118/121805-PA.

Ding, Yu. 1995. Scaling-up in the Vicinity of Wells in Heterogeneous Field. Paper presented at the SPE Reservoir Simulation Symposium, San Antonio, Texas, February 12–15. SPE-29137-MS. https://doi.org/10.2118/29137-MS.

Durlofsky, L. and Chung, E. 1990. Effective Permeability of Heterogeneous Reservoir Regions. Paper presented at the ECMOR II - 2nd European Conference on the Mathematics of Oil Recovery, Arles, France, 11-14 Sept. https://doi.org/10.3997/2214-4609.201411099.

Durlofsky, L. J. 2003. Upscaling of geocellular models for reservoir flow simulation: A review of recent progress. Paper presented at the International Forum on Reservoir Simulation, Bühl/Baden-Baden, Germany, June 23-27.

Durlofsky, L. J., Milliken, W. J., and Bernath, A. 2000. Scaleup in the Near-Well Region. *SPE Journal* **5** (01): 110-117. https://doi.org/10.2118/61855-PA.

Durlofsky, Louis J. 1991. Numerical calculation of equivalent grid block permeability tensors for heterogeneous porous media. *Water resources research* **27** (5): 699-708.

Efendiev, Yalchin R. and Durlofsky, Louis J. 2004. Accurate Subgrid Models for Two-Phase Flow in Heterogeneous Reservoirs. *SPE Journal*. https://doi.org/10.2118/88363-PA.

Farmer, C. L. 2002. Upscaling: a review. *International Journal for Numerical Methods in Fluids* **40** (1-2): 63-78.

Fincham, A.E., Christensen, J.R., Barker, J.W. et al. 2004. Up-Gridding from Geological Model to Simulation Model: Review, Applications and Limitations. *Proc.*, SPE Annual Technical Conference and Exhibition. https://doi.org/10.2118/90921-MS.

Fu, Jianlin, Axness, Carl L., and Gomez-Hernandez, J. Jaime. 2011. Upscaling Transmissivity in the Near-Well Region for Numerical Simulation: A Comparison on Uncertainty Propagation. *Engineering Applications of Computational Fluid Mechanics* **5** (1): 49-66. https://doi.org/10.1080/19942060.2011.11015352.

Fujita, Yusuke, Datta-Gupta, Akhil, and King, Michael J. 2016. A Comprehensive Reservoir Simulator for Unconventional Reservoirs That Is Based on the Fast Marching Method and Diffusive Time of Flight. *SPE Journal*. https://doi.org/10.2118/173269-PA.

Garmeh, Gholamreza and Johns, Russell Taylor. 2009. Upscaling of Miscible Floods in Heterogeneous Reservoirs Considering Reservoir Mixing. *Proc.*, SPE Annual Technical Conference and Exhibition. https://doi.org/10.2118/124000-MS.

Geiger, S. 2016. Amellago Carbonate Reservoir Model, ExxonMobil (FC)2 Alliance. *International Centre for Carbonate Reservoirs, Heriot-Watt University (Reprint)*. http://carbonates.hw.ac.uk/.

Gomez-Hernandez, J. Jaime and Journel, Andre G. 1994. Stochastic Characterization of Gridblock Permeabilities. *SPE Formation Evaluation* **9** (02): 93-99. https://doi.org/10.2118/22187-PA.

Guerillot, D. R. and Verdiere, Sophie. 1995. Different Pressure Grids for Reservoir Simulation in Heterogeneous Reservoirs. Paper presented at the SPE Reservoir Simulation Symposium, San Antonio, Texas, February 12–15. SPE-29148-MS. https://doi.org/10.2118/29148-MS.

Guerillot, D., Rudkiewicz, J. L., Ravenne, C. et al. 1990. An Integrated Model for Computer Aided Reservoir Description : from Outcrop Study to Fluid Flow Simulations. *Rev Inst Fr Pét* **45** (1): 71-77. https://doi.org/10.2516/ogst:1990005.

Holden, L. and Nielsen, B. F. 2000. Global Upscaling of Permeability in Heterogeneous Reservoirs; The Output Least Squares (OLS) Method. *Transport in Porous Media* **40** (2): 115-143. https://doi.org/10.1023/A:1006657515753.

Holden, Lars and Lia, Oddvar. 1992. A tensor estimator for the homogenization of absolute permeability. *Transport in Porous Media* **8** (1): 37-46. https://doi.org/10.1007/BF00616891.

Hossain, M.E., Tamim, M., and Rahman, N.M.A. 2007. Effects of Criterion Values on Estimation of the Radius of Drainage and Stabilization Time. *Journal of Canadian Petroleum Technology* **46** (03). https://doi.org/10.2118/07-03-01.

Hou, Thomas Y. and Efendiev, Yalchin R. 2009. Multiscale Finite Element Methods: Theory and Applications.

Hou, Thomas Y. and Wu, Xiao-Hui. 1997. A Multiscale Finite Element Method for Elliptic Problems in Composite Materials and Porous Media. *Journal of Computational Physics* **134** (1): 169-189. https://doi.org/10.1006/jcph.1997.5682.

Idrobo, Eduardo A., Choudhary, Manoj K., and Datta-Gupta, A. 2000. Swept Volume Calculations and Ranking of Geostatistical Reservoir Models Using Streamline Simulation. *Proc.*, SPE/AAPG Western Regional Meeting. https://doi.org/10.2118/62557-MS.

Iino, Atsushi, Vyas, Aditya, Huang, Jixiang et al. 2017. Rapid Compositional Simulation and History Matching of Shale Oil Reservoirs Using the Fast Marching Method. Paper presented at the Unconventional Resources Technology Conference, Austin, Texas, 24-26 July. urtec-2017-2693139. https://doi.org/10.15530/urtec-2017-2693139.

Izgec, Omer, Sayarpour, Morteza, and Shook, G. 2011. Maximizing volumetric sweep efficiency in waterfloods with hydrocarbon F–Φ curves. *Journal of Petroleum Science and Engineering - J PET SCI ENGINEERING* **78**: 54-64.

Jayasinghe, Savithru, Darmofal, David L., Dow, Eric et al. 2019. A Discretization-Independent Distributed Well Model. *SPE Journal* **24** (06): 2946-2967. https://doi.org/10.2118/198898-PA.

Jessen, K. and Orr, F. M., Jr. 2002. Compositional Streamline Simulation. Paper presented at the SPE Annual Technical Conference and Exhibition. SPE-77379-MS. https://doi.org/10.2118/77379-MS.

Journel, A. G., Deutsch, C., and Desbarats, A. J. 1986. Power Averaging for Block Effective Permeability. Paper presented at the SPE California Regional Meeting, Oakland, California, April 2–4. SPE-15128-MS. https://doi.org/10.2118/15128-MS.

Kam, Dongjae and Datta-Gupta, Akhil. 2016. Streamline-Based Transport Tomography With Distributed Water Arrival Times. *SPE Reservoir Evaluation & Engineering* **19** (02): 265-277. https://doi.org/10.2118/169105-PA.

Karimi-Fard, Mohammad and Durlofsky, Louis. 2012. Accurate Resolution of Near-Well Effects in Upscaled Models Using Flow-Based Unstructured Local Grid Refinement. *SPE Journal* **17** (04): 1084-1095. https://doi.org/10.2118/141675-PA.

King, M. J., MacDonald, D. G., Todd, S. P. et al. 1998. Application of Novel Upscaling Approaches to the Magnus and Andrew Reservoirs. Paper presented at the European Petroleum Conference, The Hague, Netherlands, October 20–22. SPE-50643-MS. https://doi.org/10.2118/50643-MS.

King, M. J. and Mansfield, Mark. 1999. Flow Simulation of Geologic Models. *SPE Reservoir Evaluation & Engineering* **2** (04): 351-367. https://doi.org/10.2118/57469-PA.

King, Michael J. 2007. Upgridding and Upscaling: Current Trends and Future Directions. SPE Distinguished Lecture. https://doi.org/10.2118/112810-DL.

King, Michael J., Wang, Zhenzhen, and Datta-Gupta, Akhil. 2016. Asymptotic Solutions of the Diffusivity Equation and Their Applications. Paper presented at the SPE Europec featured at 78th EAGE Conference and Exhibition, Vienna, Austria, May 30–June 2. SPE-180149-MS. https://doi.org/10.2118/180149-MS.

King, P. R. 1989. The use of renormalization for calculating effective permeability. *Transport in Porous Media* **4** (1): 37-58. https://doi.org/10.1007/BF00134741.

Krogstad, S., Lie, K.A., Nilsen, H.M. et al. 2016. Flow Diagnostics for Optimal Polymer Injection Strategies. https://doi.org/10.3997/2214-4609.201601874.

Krogstad, S. and Nilsen, H. Møll. 2020. Efficient Adjoint-Based Well-Placement Optimization Using Flow Diagnostics Proxies. **2020** (1): 1-14. https://doi.org/10.3997/2214-4609.202035227.

Krogstad, Stein, Lie, Knut-Andreas, Nilsen, Halvor Møll et al. 2017. Efficient flow diagnostics proxies for polymer flooding. *Computational Geosciences* **21** (5): 1203-1218. https://doi.org/10.1007/s10596-017-9681-9.

Kuchuk, Fikri J. 2009. Radius of Investigation for Reserve Estimation From Pressure Transient Well Tests. Paper presented at the SPE Middle East Oil and Gas Show and Conference, March 15–18. SPE-120515-MS. https://doi.org/10.2118/120515-MS.

Kulkarni, Kari Nordaas, Datta-Gupta, Akhil, and Vasco, D. W. 2001. A Streamline Approach for Integrating Transient Pressure Data Into High-Resolution Reservoir Models. *SPE Journal*. https://doi.org/10.2118/74135-PA.

Lake, L. W. and Jensen, J. L. 1989. A Review of Heterogeneity Measures Used in Reservoir Characterization. SPE Unsolicited. https://doi.org/10.2118/20156-MS.

Lee, John. 1982. *Well Testing*. Richardson, Texas: Textbook Series, Society of Petroleum Engineers.

Li, Chen and King, Michael J. 2016. Integration of Pressure Transient Data Into Reservoir Models Using the Fast Marching Method. Paper presented at the SPE Europec featured at 78th EAGE Conference and Exhibition, Vienna, Austria, May 30–June 2. SPE-180148-MS. https://doi.org/10.2118/180148-MS.

Li, Hangyu, Chen, Yuguang, Rojas, Danny et al. 2014. Development and application of near-well multiphase upscaling for forecasting of heavy oil primary production. *Journal of Petroleum Science and Engineering* **113**: 81-96. https://doi.org/10.1016/j.petrol.2014.01.002.

Li, Hangyu and Durlofsky, Louis J. 2016. Upscaling for Compositional Reservoir Simulation. *SPE Journal* **21** (03): 873-887. https://doi.org/10.2118/173212-PA.

Lie, Knut-Andreas. 2019. *An Introduction to Reservoir Simulation Using MATLAB/GNU Octave: User Guide for the MATLAB Reservoir Simulation Toolbox (MRST).* Cambridge: Cambridge University Press.

Liu, C., Nunna, K., and King, M.J. 2020. Application of Diffuse Source Basis Functions for Improved Near Well Upscaling. **2020** (1): 1-31. https://doi.org/10.3997/2214-4609.202035156.

Liu, Ching-Hsien, Nunna, Krishna, Syed, Imroj et al. 2019. Evaluation of Upscaling Approaches for the Amellago Carbonate Outcrop Model. Paper presented at the SPE Europec featured at 81st EAGE Conference and Exhibition, London, England, UK, June 3–6. SPE-195560-MS. https://doi.org/10.2118/195560-MS.

Lunati, Ivan, Bernard, Dominique, Giudici, Mauro et al. 2001. A numerical comparison between two upscaling techniques: non-local inverse based scaling and simplified renormalization. *Advances in Water Resources* **24** (8): 913-929. https://doi.org/10.1016/S0309-1708(01)00008-2.

Malone, Andrew, King, Michael J., and Wang, Zhenzhen. 2019. Characterization of Multiple Transverse Fracture Wells Using the Asymptotic Approximation of the Diffusivity Equation. Paper presented at the SPE Europec featured at 81st EAGE Conference and Exhibition. D031S004R002. https://doi.org/10.2118/195505-MS.

Mascarenhas, O. and Durlofsky, L. J. 2000. Coarse scale simulation of horizontal wells in heterogeneous reservoirs. *Journal of Petroleum Science and Engineering* **25** (3): 135-147. https://www.sciencedirect.com/science/article/pii/S0920410500000097.

Matthews, C.S., Brons, F., and Hazebroek, P. 1954. A Method for Determination of Average Pressure in a Bounded Reservoir. *Transactions of the AIME* **201** (01): 182-191. https://doi.org/10.2118/296-G.

Møyner, Olav, Krogstad, Stein, and Lie, Knut-Andreas. 2015a. The Application of Flow Diagnostics for Reservoir Management. *SPE Journal* **20** (02): 306-323. https://doi.org/10.2118/171557-PA.

Møyner, Olav, Krogstad, Stein, and Lie, Knut-Andreas. 2015b. The Application of Flow Diagnostics for Reservoir Management. *SPE Journal*.

Muggeridge, A.H., Cuypers, M., Bacquet, C. et al. 2002. Scale-up of well performance for reservoir flow simulation. *Petroleum Geoscience* **8** (2): 133-139. https://doi.org/10.1144/petgeo.8.2.133.

Nakashima, Toshinori, Li, Hangyu, and Durlofsky, Louis J. 2012. Near-well upscaling for three-phase flows. *Computational Geosciences* **16** (1): 55-73. https://doi.org/10.1007/s10596-011-9252-4.

Nielsen, Bjørn Fredrik and Tveito, Aslak. 1998. An upscaling method for one-phase flow in heterogeneous reservoirs. A weighted output least squares (WOLS) approach. *Computational Geosciences* **2** (2): 93-123. https://doi.org/10.1023/A:1011541917701.

Nunna, Krishna and King, Michael J. 2017. Dynamic Downscaling and Upscaling in High Contrast Systems. Paper presented at the SPE Reservoir Simulation Conference, Montgomery, Texas, USA, February 20–22. SPE-182689-MS. https://doi.org/10.2118/182689-MS.

Nunna, Krishna and King, Michael J. 2020. Dynamic Diffuse-Source Upscaling in High-Contrast Systems. *SPE Journal* **25** (01): 347-368. https://doi.org/10.2118/182689-PA.

Nunna, Krishna, Liu, Ching-Hsien, and King, Michael J. 2019. Application of diffuse source functions for improved flow upscaling. *Computational Geosciences*. https://doi.org/10.1007/s10596-019-09868-x.

Nunna, Krishna, Zhou, Peng, and King, Michael J. 2015. Novel Diffuse Source Pressure Transient Upscaling. Paper presented at the SPE Reservoir Simulation Symposium, Houston, Texas, USA, February 23–25. SPE-173293-MS. https://doi.org/10.2118/173293-MS.

Olalotiti-Lawal, Feyi, Hetz, Gil, Salehi, Amir et al. 2020. Application of Flow Diagnostics to Rapid Production Data Integration in Complex Grids and Dual-Permeability Models. *SPE Journal* **25** (04): 2000-2020. https://doi.org/10.2118/195253-PA.

Olalotiti-Lawal, Feyi, Onishi, Tsubasa, Kim, Hyunmin et al. 2017. Post-Combustion CO2 EOR Development in a Mature Oil Field: Model Calibration Using a Hierarchical Approach. *Proc.,* SPE Annual Technical Conference and Exhibition. https://doi.org/10.2118/187116-MS.

Pasumarti, Ashwin, Sengupta, Soumyadipta, and Michael, J. King. 2015. A Novel Transient Simulation Based Methodology for the Calculation of Permeability in Pore Network Models. Paper presented at the Abu Dhabi International Petroleum Exhibition and Conference, Abu Dhabi, UAE, November 9–12. SPE. https://doi.org/10.2118/177884-MS.

Peaceman, D. W. 1978. Interpretation of Well-Block Pressures in Numerical Reservoir Simulation (includes associated paper 6988). *SPE Journal*. https://doi.org/10.2118/6893-PA.

Peaceman, D. W. 1983. Interpretation of Well-Block Pressures in Numerical Reservoir Simulation With Nonsquare Grid Blocks and Anisotropic Permeability. *SPE Journal*. https://doi.org/10.2118/10528-PA.

Peaceman, D. W. 1990. Interpretation of Wellblock Pressures in Numerical Reservoir Simulation: Part 3 -- Off-Center and Multiple Wells Within a Wellblock. *SPE Reservoir Engineering* **5** (02): 227-232. https://doi.org/10.2118/16976-PA.

Peaceman, Donald W. 1996. Calculation of Transmissibilities of Gridblocks Defined by Arbitrary Corner Point Geometry. SPE Unsolicited. SPE-37306-MS. https://doi.org/10.2118/37306-MS.

Pickup, G. E., Ringrose, P. S., Jensen, J. L. et al. 1994. Permeability tensors for sedimentary structures. *Mathematical Geology* **26** (2): 227-250. https://doi.org/10.1007/BF02082765.

Pollock, D. W. 1988. Semianalytical computation of path lines for finite-difference models. *Ground Water* **26** (6): 743-750. http://pubs.er.usgs.gov/publication/70013303.

Pomata, Matias, Valle, Jorge E., and Menendez, Angel N. 2007. Streamline-Based Simulator for Unstructured Grids. Paper presented at the Latin American & Caribbean Petroleum Engineering Conference. SPE-107391-MS. https://doi.org/10.2118/107391-MS.

Prevost, Mathieu, Edwards, Michael G., and Blunt, Martin J. 2002. Streamline Tracing on Curvilinear Structured and Unstructured Grids. *SPE Journal* **7** (02): 139-148. https://doi.org/10.2118/78663-PA.

Renard, Ph and de Marsily, G. 1997. Calculating equivalent permeability: a review. *Advances in Water Resources* **20** (5): 253-278. https://doi.org/10.1016/S0309-1708(96)00050-4.

Ringrose, Philip and Bentley, Mark. 2015. The Rock Model. In *Reservoir Model Design*. Dordrecht: Springer.

Schlumberger. 2017. *ECLIPSE® Version 2017.1 Reference Manual*. Abingdon, UK: Schlumberger.

Schmalz, J. and Rahme, H. 1950. The variation of waterflood performance with variation in permeability profile. *Prod Monthly* **15** (9): 9-12.

Sethian, J. A. 1996. A fast marching level set method for monotonically advancing fronts. *Proceedings of the National Academy of Sciences of the United States of America* **93** (4): 1591-1595. https://doi.org/10.1073/pnas.93.4.1591.

Sethian, J. A. . 1999. Fast marching methods. *SIAM Review* **41** (2): 199-235. https://doi.org/10.1137/S0036144598347059.

Shahvali, Mohammad, Mallison, Bradley, Wei, Kaihong et al. 2012. An Alternative to Streamlines for Flow Diagnostics on Structured and Unstructured Grids. *SPE Journal*. https://doi.org/10.2118/146446-PA.

Shekhar, R., Sahni, I., Benson, G. et al. 2014. Modelling and simulation of a Jurassic carbonate ramp outcrop, Amellago, High Atlas Mountains, Morocco. *Petroleum Geoscience* **20** (1): 109.

Shook, G. Michael and Mitchell, Kameron M. 2009. A Robust Measure of Heterogeneity for Ranking Earth Models: The F PHI Curve and Dynamic Lorenz Coefficient. Paper presented at the SPE Annual Technical Conference and Exhibition, New Orleans, Louisiana, October 4–7. SPE-124625-MS. https://doi.org/10.2118/124625-MS.

Soeriawinata, T., Kasap, E., and Kelkar, M. 1997. Permeability Upscaling for Near-Wellbore Heterogeneities. *SPE Formation Evaluation* **12** (04): 255-262. https://doi.org/10.2118/36518-PA.

Sosa, L. Gutierrez, Geiger, S., and Doster, F. 2020. Hydro-Mechanical Coupling for Flow Diagnostics: A Fast Screening Method to Assess Geomechanics on Flow Field Distributions. **2020** (1): 1-19. https://doi.org/10.3997/2214-4609.202035242.

Spooner, Victoria, Geiger, Sebastian, and Arnold, Dan. 2019. Flow diagnostics for naturally fractured reservoirs. *Petroleum Geoscience* **25** (4): 490. http://pg.lyellcollection.org/content/25/4/490.abstract.

Sun, Shuyu, Gai, Xiuli, and Wheeler, Mary F. 2005. Streamline Tracing on Unstructured Grids. Paper presented at the SPE Annual Technical Conference and Exhibition. SPE-96947-MS. https://doi.org/10.2118/96947-MS.

Syed, Imroj, Liu, Ching-Hsien, Kelkar, Mohan G. et al. 2020. Improved Distance Based Upgridding and Diffuse Source Upscaling for High Resolution Geologic Models. Paper presented at the SPE Annual Technical Conference and Exhibition, Virtual, October 26–29. SPE. https://doi.org/10.2118/201727-MS.

Tanaka, Shusei, Datta-Gupta, Akhil, and King, Michael. 2013. *A Novel Approach for Incorporation of Capillarity and Gravity Into Streamline Simulation Using Orthogonal Projection*, Vol. 2.

Tanaka, Shusei, Kam, Dongjae, Datta-Gupta, Akhil et al. 2015. Streamline-Based History Matching of Arrival Times and Bottomhole Pressure Data for Multicomponent Compositional Systems. Paper presented at the SPE Annual Technical Conference and Exhibition. D021S013R004. https://doi.org/10.2118/174750-MS.

Vasco, DW and Datta-Gupta, Akhil. 1999. Asymptotic solutions for solute transport: A formalism for tracer tomography. *Water Resources Research* **35** (1): 1-16.

Vasco, DW, Keers, Henk, and Karasaki, Kenzi. 2000. Estimation of reservoir properties using transient pressure data: An asymptotic approach. *Water Resources Research* **36** (12): 3447-3465.

Virieux, Jean, Flores-Luna, Carlos, and Gibert, Dominique. 1994. Asymptotic theory for diffusive electromagnetic imaging. *Geophysical Journal International* **119** (3): 857-868.

Wang, Zhenzhen, Li, Chen, and King, Michael. 2017. Validation and Extension of Asymptotic Solutions of Diffusivity Equation and Their Applications to Synthetic Cases. Paper presented at the SPE Reservoir Simulation Conference, Montgomery, Texas, USA, February 20–22. SPE-182716-MS. https://doi.org/10.2118/182716-MS.

Warren, J. E. and Price, H. S. 1961. Flow in Heterogeneous Porous Media. *Society of Petroleum Engineers Journal* **1** (03): 153-169. https://doi.org/10.2118/1579-G.

Watson, F., Krogstad, S., and Lie, K. 2020. Flow Diagnostics for Model Ensembles. **2020** (1): 1-19. https://doi.org/10.3997/2214-4609.202035133.

Wattenbarger, Robert A., El-Banbi, Ahmed H., Villegas, Mauricio E. et al. 1998. Production Analysis of Linear Flow Into Fractured Tight Gas Wells. Paper presented at the SPE Rocky Mountain Regional/Low-Permeability Reservoirs Symposium, Denver, Colorado, April 5–8. SPE-39931-MS. https://doi.org/10.2118/39931-MS.

Weijermars, Ruud, Tugan, Murat Fatih, and Khanal, Aadi. 2020. Production rates and EUR forecasts for interfering parent-parent wells and parent-child wells: Fast analytical solutions and validation with numerical reservoir simulators. *Journal of Petroleum Science and Engineering* **190**: 107032. https://doi.org/10.1016/j.petrol.2020.107032.

Wen, X. H., Durlofsky, L. J., and Edwards, M. G. 2003. Use of Border Regions for Improved Permeability Upscaling. *Mathematical Geology* **35** (5): 521-547. https://doi.org/10.1023/A:1026230617943.

Wen, X. H., Durlofsky, L. J., Lee, S. H. et al. 2000. Full Tensor Upscaling of Geologically Complex Reservoir Descriptions. Paper presented at the SPE Annual Technical Conference and Exhibition, Dallas, Texas, October 1–4. SPE. https://doi.org/10.2118/62928-MS.

Wen, Xian-Huan, Durlofsky, Louis J., and Chen, Yuguang. 2006. Efficient 3D Implementation of Local-Global Upscaling for Reservoir Simulation. *SPE Journal*. https://doi.org/10.2118/92965-PA.

White, C. D. and Horne, R. N. 1987. Computing Absolute Transmissibility in the Presence of Fine-Scale Heterogeneity. Paper presented at the SPE Symposium on Reservoir Simulation, San Antonio, Texas, February 1–4. SPE-16011-MS. https://doi.org/10.2118/16011-MS.

Wu, Xiao-Hui, Efendiev, Y, and Hou, Thomas Y. 2002. Analysis of upscaling absolute permeability. *Discrete and Continuous Dynamical Systems Series B* **2** (2): 185-204.

Xie, Jiang, Yang, Changdong, Gupta, Neha et al. 2015. Integration of Shale-Gas-Production Data and Microseismic for Fracture and Reservoir Properties With the Fast Marching Method. *SPE Journal* **20** (02): 347-359. https://doi.org/10.2118/161357-PA.

Yang, Changdong, Sharma, Vishal Kumar, Datta-Gupta, Akhil et al. 2015. A Novel Approach for Production Transient Analysis of Shale Gas/Oil Reservoirs. Paper presented at the Unconventional Resources Technology Conference, San Antonio, Texas, USA, July 20–22. URTEC. https://doi.org/10.15530/URTEC-2015-2176280.

Yang, Changdong, Xue, Xu, Huang, Jixiang et al. 2016. Rapid Refracturing Candidate Selection in Shale Reservoirs Using Drainage Volume and Instantaneous Recovery Ratio. Paper presented at the SPE/AAPG/SEG Unconventional Resources Technology Conference, San Antonio, Texas, USA, August 1–3. URTEC. https://doi.org/10.15530/URTEC-2016-2459368.

Yin, Jichao, Park, Hanyoung, Datta-Gupta, Akhil et al. 2010. A Hierarchical Streamline-Assisted History Matching Approach with Global and Local Parameter Updates. *Proc.*, SPE Western Regional Meeting. https://doi.org/10.2118/132642-MS.

Zhang, Yanbin, Bansal, Neha, Fujita, Yusuke et al. 2016. From Streamlines to Fast Marching: Rapid Simulation and Performance Assessment of Shale-Gas Reservoirs by Use of Diffusive Time of Flight as a Spatial Coordinate. *SPE Journal*. https://doi.org/10.2118/168997-PA.

Zhang, Yanbin, Yang, Changdong, King, Michael J. et al. 2013. Fast-Marching Methods for Complex Grids and Anisotropic Permeabilities: Application to Unconventional Reservoirs. Paper presented at the SPE Reservoir Simulation Symposium, The Woodlands, Texas, USA, February 18–20. SPE. https://doi.org/10.2118/163637-MS.

Zhou, Yijie and King, Michael J. 2011. Improved Upscaling for Flow Simulation of Tight Gas Reservoir Models. Paper presented at the SPE Annual Technical Conference and Exhibition, Denver, Colorado, USA, October 30–November 2. SPE-147355-MS. https://doi.org/10.2118/147355-MS.